A search for long-lived neutral particles decaying to oppositely charged lepton pairs in pp collisions at $\sqrt{s} = 13$ TeV with the ATLAS detector

DISSERTATION

Presented in Partial Fulfillment of the Requirements for the Degree Doctor of Philosophy in the Graduate School of The Ohio State University

By

Benjamin Cote, B.S., M.S.

Graduate Program in Physics

The Ohio State University

2023

Dissertation Committee:

Professor K.K. Gan, Advisor

Professor Antonio Boveia

Professor Linda Carpenter

Professor Comert Kural

CERN-THESIS-2023-269
20/11/2023

© Copyright by

Benjamin Cote

2023

Abstract

A search for long-lived neutral massive particles decaying to an oppositely charged $\mu\mu$, ee, or $e\mu$ lepton pair is presented using 140 fb^{-1} of Run II proton-proton collision data at $\sqrt{s} = 13$ TeV collected by the ATLAS detector at the LHC from 2015 to 2018. The lepton pairs must form a vertex within the inner tracking volume of the detector, displaced from the primary vertex, and have a dilepton mass greater than 12 GeV. These signal selections effectively suppress Standard Model backgrounds where the remaining background, from high-energy cosmic ray muons and randomly crossing charged particle tracks, are estimated using data-driven methods. The results are interpreted for a model where a generic Z' is the long-lived particle, pair-produced from a new heavy scalar (S) and decaying to lepton pairs or pairs of fermionic dark matter (χ). Generic detection efficiencies and upper limits on the cross section are also presented for resonances with a mass of 100-700 GeV and decay length ($c\tau$) of 100-1000 mm. Despite the pair-produced nature of the Z' in the specific model interpretation, the analysis searches for a single displaced vertex, allowing the results to be reinterpreted for other Beyond the Standard Model theories.

To my parents and brothers.

Acknowledgments

When I first chose physics as a major, I was just a young high school senior with a sense of curiosity and deep desire for a challenge. Over a decade later, I can say, without a doubt, that this has been the most challenging part of my journey. With trips across the world, a global pandemic, and many other trials, this program pushed me to my mental and emotional limits, but that curiosity and yearning for a challenge still remain.

Reaching this point was made possible in large part due to the guidance of my advisor, Prof. K.K. Gan. His support and advice have constantly pushed me to be a better and more insightful physicist. Almost seven years after meeting, I count myself lucky to have found an advisor with whom a share such a good working relationship and sense of humor with. I would also like to thank the rest of my committee, Prof. Boveia, Prof. Carpenter, and Prof. Kural, whose input has broadened my perspective on high energy physics research. Prof. Boveia, in particular, was an invaluable source of reassurance throughout my graduate program.

The research and results of this dissertation would also not have been complete without the collaboration of my colleagues Zachary Pollock and Dr. Rachel Rosten. Their hard work and support through this process have been essential to the success of the analysis.

During the lowest points of my time in this program, my friends from high school, undergraduate, and graduate school were always there to pick me up and remind me how far I've come. Dr. Danny Tuthill and Dr. Anthony Tropiano, in particular, were vital to my ability to make it through the COVID pandemic unscathed. It is truly remarkable that all three of us finished the program with doctoral degrees.

Finally, I want to thank my parents, brothers, and girlfriend. They have believed in me when I haven't believed in myself and their love and support has motivated me to not just be a better scientist, but a better person as well. Without their perspective and backing, I would not be the person I am today.

Vita

August 5, 1995	Born - Princeton, MN
2017	B.S. Physics and Mathematics, University of Notre Dame, Notre Dame, IN
2019	M.S. Physics, The Ohio State University, Columbus, OH
2017-2018	Graduate Fellow, The Ohio State University, Columbus, OH
2018-2019	Graduate Teaching Associate, The Ohio State University, Columbus, OH
2019-present	Graduate Research Associate, The Ohio State University, Columbus, OH

Fields of Study

Major Field: Physics

Studies in:

Beyond the Standard Model searches	K.K. Gan
Optoboard production	K.K. Gan

Table of Contents

List of Figures

Figure **Page**

List of Tables

Chapter 1
Introduction

The Standard Model (SM) of particle physics, which describes the known fundamental particles and their interactions, has been experimentally verified at colliders for the past several decades. Since the discovery of a particle consistent with the Higgs Boson in 2012, reported by the ATLAS [1] and Compact Muon Solenoid (CMS) [2] experiments at the Large Hadron Collider (LHC), the SM is considered relatively complete despite its inability to explain several phenomena in the universe. While it has successfully described a majority of the results in experiments, it remains unable to fully explain phenomena such as the hierarchy problem [3, 4], the existence of dark matter [5–7], and matter-antimatter symmetry [8, 9]. As a result, Beyond the Standard Model (BSM) theories have been developed in an attempt to extend the SM's reach to cover these phenomena. In particular, exotic theories with collider signatures can and have been probed at experiments such as those at the LHC with no evidence of any elegant theoretical solution to date. With experimental results further constraining accessible parameter space for these exotic theories, it becomes more essential to consider less conventional signatures.

In this thesis, 140 fb^{-1} of Run II dataset collected in pp collisions at $\sqrt{s} = 13$ TeV at the ATLAS experiment between 2015 and 2018 is used to search for displaced dilepton vertices formed by long-lived particle decays to oppositely charged leptons. The analysis is performed in the context of an exotic Z' extension to the SM where the Z' has a macroscopic decay length ($c\tau$) and decays to $\mu\mu$, ee, or $e\mu$ pairs. The long-lived Z' decays are required to be located in the Inner Detector (ID) volume and have dilepton reconstructed mass of at least 12 GeV to reject SM backgrounds. The details of the SM are discussed in Chapter 2 while both general BSM Z' extensions and the specific theory used as a benchmark here are detailed in Chapter 3. Chapter 4 provides an introductory discussion of the LHC and the ATLAS experiment used to collect the dataset of interest. Further Chapters include the analysis details, such as the many specialized reconstruction methods for signal objects, data-driven background estimations, and systematic uncertainties.

Chapter 2
The Standard Model

The SM [10] of particle physics is the foundational theory on which the understanding of the known elementary particles and their interactions is built. It has been remarkably successful for the better part of the 20th century at providing a single framework under which these particles verifiably behave and interact in experimental observation. The SM covers three of the four fundamental forces with the exception of gravity, which is described by Einstein's theory of general relatively [11] and whose strength is too weak by comparison to contribute meaningfully at high-energy physics experiments. The three other forces include quantum chromodynamics (QCD), the weak interaction, and quantum electrodynamics (QED), and are described by the $SU(3)_C \otimes SU(2)_L \otimes U(1)_Y$ symmetry group. The requirements of local gauge invariance give rise to this symmetry group and the resulting forces, along with gravity, describe the interactions between the fundamental SM particles. The electromagnetic and weak interactions are unified in the Glashow-Weinberg-Salam theory as the electroweak symmetry group. In the SM, this unified symmetry is broken by the Higgs mechanism, resulting in the Higgs boson and nonzero masses for elementary particles. With the discovery of the Higgs boson at the LHC in 2012 [1, 2], the experimental picture of the SM was completed, marking the end of long search since its prediction in 1964 [12]. Further details of the SM are provided in the following section.

2.1 Fundamental Particles

The elementary particles of the SM can be classified according to the spin of the particle into two groups. The first is the half-integer spin particles, called fermions, that are the building blocks of all visible matter in the universe. Fermions can be further classified into leptons and quarks with different interactions with the fundamental forces. Leptons, such as electrons and muons, and quarks, which combine to form baryons like the well-known protons and neutrons, each come in three generations organized by increasing mass with two leptons and two quarks in each generation. Each fermion has an associated anti-fermion with the same mass but opposite quantum numbers. The second group consists of integer spin particles called bosons, which, with the exception of the Higgs boson, are responsible for mediating the three fundamental interactions detailed in Section 2.2. The Higgs boson, on the other hand, is the result of spontaneous electroweak symmetry breaking (EWSB), as detailed in Section 2.3.

2.2 Fundamental Interactions

The mathematical foundation of the SM is quantum field theory (QFT), where, specifically, the SM is a non-abelian gauge-invariant QFT with the gauge group $SU(3)_C \otimes SU(2)_L \otimes U(1)_Y$ representing the strong ($SU(3)_C$) and electromagnetic and weak ($SU(2)_L \otimes U(1)_Y$) interactions. While the mathematical formalism of QFT and the SM are left for further reading, conceptually, each of the elementary particles is a quanta of one of the fields and the local gauge invariance of the SM Lagrangian density introduces the rules by which the fermionic spinor fields interact with each other via the bosonic vector fields. For each of the fundamental forces in the SM, fermions interact by the exchange of a gauge boson, which is considered the mediator of that interaction. Fermions must, therefore, have a charge in a given gauge field in order to exchange the appropriate boson and these charges define the elementary particles.

The first symmetry group, $SU(3)_C$, describes the strong interaction, where C denotes the charge for the gauge fields, color, which can have the value of red, blue, or green. Only quarks interact via the strong force, but, due to color confinement [13], quarks are only observed in color-neutral bound states in nature. These bound state configurations are known as hadrons and exist as either quark anti-quark pairs, called mesons, or three-quark systems, called baryons. Similar to positive and negative charges, anti-quarks have anti-color charges that make mesons color-neutral composite particles and allow baryons to consist of one of each color or one of each anti-color. There are eight different gluon fields generated by the $SU(3)_C$ group, where the quanta are massless gluons that carry their own color charges and are capable of self-interaction. While color confinement requires quarks and gluons exist in nature as hadrons, such as protons, they can interact as free particles when probed at high enough energies, a property known as asymptotic freedom [14, 15]. At the LHC, in particular, protons can reach high enough energies such that their constituent particles can interact and hadronize to form new hadrons.

The second symmetry group, $SU(2)_L \otimes U(1)_Y$, describes the unified electromagnetic and weak interactions, where the L and Y subscripts are more complicated than simply denoting the charge of their respective gauge fields. All six quarks and all six leptons participate in electroweak interactions, but do not necessarily interact via the electromagnetic and weak forces when considered separately. Fermions are the quanta of either left-handed or right-handed fields, where the left-handed fields are fermions and right-handed ones are antifermions. The charge of the weak interaction is the third component of the weak isospin, I_3. The weak interaction is a chiral theory, meaning left and right-handed fermions interact differently and the L in $SU(2)_L$ denotes that only the left-handed fermions transform as doublets while the right-handed fermions transform as singlets. In practice, this means that each doublet contains either a left-handed lepton and its corresponding neutrino or a pair of left-handed quarks and have $I_3 = \pm\frac{1}{2}$. Right-handed neutrinos are assumed to be assumed to massless in the SM and are not included [16], but all other right-handed fermions exist as singlets and have $I_3 = 0$. As a consequence, neutrinos are constrained to only interact via the weak interaction while the other fermions have electrical charge as well. Similarly, only right-handed antifermions interact via the weak interaction while left-handed antifermions have $I_3 = 0$. $U(1)_Y$ uses Y to denote the weak hypercharge and to distinguish the symmetry group from the well-known $U(1)_Q$ from QED. Electrical charge, Q, is given by the Gell-Mann-Nishijima relation:

$$Q = I_3 + \frac{Y}{2}. \tag{2.1}$$

In summary, the three massless, colorless lepton neutrinos interact exclusively via the weak force, the three colorless leptons interact via both the weak and electromagnetic forces, and the quarks interact via all three of the fundamental forces covered by the SM. Each of the fermions, their corresponding quantum numbers, and their masses are given in Table 2.1.

Table 2.1: A summary of the fundamental fermions and their quantum numbers and masses.

	Generation	I_3 (L, R)	Y (L, R)	Q	Mass (MeV)
Quarks:					
u	1	(+1/2, 0)	(+1/3, +4/3)	+2/3	2.3
d	1	(-1/2, 0)	(+1/3, -2/3)	-1/3	4.8
c	2	(+1/2, 0)	(+1/3, +4/3)	+2/3	1275
s	2	(-1/2, 0)	(+1/3, -2/3)	-1/3	95
t	3	(+1/2, 0)	(+1/3, +4/3)	+2/3	173070
b	3	(-1/2, 0)	(+1/3, -2/3)	-1/3	4180
Leptons:					
ν_e	1	(+1/2, N/A)	(-1, N/A)	0	0
e	1	(-1/2, 0)	(-1, -2)	-1	0.511
ν_μ	2	(+1/2, N/A)	(-1, N/A)	0	0
μ	2	(-1/2, 0)	(-1, -2)	-1	105.7
ν_τ	3	(+1/2, N/A)	(-1, N/A)	0	0
τ	3	(-1/2, 0)	(-1, -2)	-1	1777

The unified electroweak group, $SU(2)_L \otimes U(1)_Y$, generates the gauge fields W_μ^{a} (a $=$ $1, 2, 3$) and B_μ, which mediate the electroweak interaction. The gauge bosons observed in nature, however, are $W\pm$, Z, and photon, γ, which are the consequence of the mixing of the generated fields:

$$\begin{aligned} W_\mu^\pm &= (W_\mu^1 \mp iW_\mu^2)/\sqrt{2} \\ Z_\mu &= \cos\theta_W W_\mu^3 - \sin\theta_W B_\mu \\ A_\mu &= \sin\theta_W W_\mu^3 + \cos\theta_W B_\mu \end{aligned} \tag{2.2}$$

for mixing angle θ_W and A_μ is the gauge field corresponding to the photon. The gauge bosons, their symmetry groups, charges, and masses are summarized in Table 2.2. While only massless particles have been theoretically considered thus far, it is evident in Tables 2.1-2.2, that many of the physically observed particles in the SM do, indeed, have mass. The mechanism by which these particles attain their mass is detailed in the following section.

Table 2.2: A summary of the gauge bosons and their charges and masses.

Symmetry	Gauge boson	Q	Mass (GeV)
$SU(3)_C$	g	0	0
	γ	0	0
$SU(2)_L \otimes U(1)_Y$	Z	0	91.2
	$W^\pm$	±1	80.4

2.3 Electroweak Symmetry Breaking and the Higgs Boson

The introduction of mass terms to the SM Lagrangian density to account for experimental observation would break the local gauge invariance of the theory, necessitating some mechanism by which the massive SM particles can attain their masses while maintaining this invariance. This mechanism is known as the Higgs mechanism, where a new complex $SU(2)_L$ scalar field, called the Higgs field, is introduced, couples to the electroweak gauge fields and is capable of self interaction. The Higgs field has a nontrivial ground state, giving the Higgs potential a nonzero vacuum expectation value. While the Higgs field remains invariant to $U(1)_Q$ gauge transformations, allowing the photon to remain massless, this nonzero ground state breaks the symmetry of $SU(2)_L \otimes U(1)_Y$ gauge transformations, hence the term EWSB. The result of this EWSB is the prediction of a massive spin-0 scalar boson, the Higgs boson, that was discovered at the LHC in 2012 [1, 2], verifying the last missing piece of the SM. Due to the coupling to the electroweak gauge fields, the physical gauge bosons become the mass eigenstates given in Equation 2.2 where $\cos\theta_W = m_W/m_Z$ and the mass terms are introduced for the $W^{\pm}$ and Z-bosons. The SM fermions acquire their masses through Yukawa couplings to the Higgs field where, similarly, the fermions take the physical form of the mass eigenstates given in Table 2.1 .

2.4 Limitations

Despite the successes of the SM, there exist several phenomena in nature that remain both unpredicted and unexplained by the SM. These phenomena include the fourth fundamental force, gravity [17], the existence of dark matter [5, 6] and dark energy [18, 19], nonzero neutrino masses [20], and matter-antimatter symmetry [8, 9] with brief details provided here. The SM framework lacks any QFT describing gravity. Similarly, there are no SM particle candidates matching the properties of dark matter and dark energy. Not only have neutrinos been observed to have nonzero mass, physical neutrinos are also not the mass eigenstates; rather, they oscillate between the mass states and are observed as a composition of them. Matter and antimatter are assumed to have existed in equal quantities at the start of the universe and, yet, a vast majority of the visible universe consists of matter, an asymmetry the SM is unable to explain. In addition to the aforementioned phenomena, there are also physical observations that are only partially explained by the SM, implying the incomplete nature of the theory. These include the hierarchy problem [3, 4], where the scale of the observed Higgs boson mass, 125 GeV, appears unnatural due the theoretical fine-tuning necessary to achieve this scale, and the strong CP problem, where QCD does not require CP conservation in strong interactions, but no CP-violating strong interactions are observed in nature. As a result of these examples, many BSM theories have been developed to extend the SM's reach to cover these phenomena.

Chapter 3
Beyond the Standard Model Physics

In an attempt to rectify the shortcomings of the SM described in Section 2.4, BSM theories have been developed to explain certain phenomenology. In particular, many BSM theories predict the addition of a new $U(1)$ gauge symmetry group (denoted $U(1)'$) mediated by a new neutral gauge boson that is weakly coupled and closely resembles the SM Z boson. Naturally, this new gauge boson is referred to as Z' and, depending on the specific theory of the symmetry group, can reach masses of several TeV with decay lengths ($c\tau$) ranging from less than 1 to well over 1000 mm. With certain BSM theories accessible only at larger energy scales, the LHC provides a unique way to probe a wide range of parameter space for these theoretical Z'. Basic $U(1)'$ extensions and the limits on prompt Z' are discussed in Section 3.1 while more complex extensions and the limits on long-lived Z' are discussed in Section 3.2.

3.1 Basic $U(1)'$ Extensions

Hidden valley (HV) theories are a collection of mechanisms by which an additional $U(1)'$ gauge symmetry group is added to the SM [21, 22] with a new group of particles considered inaccessible, or "dark," physics that occur in this hidden sector. These theories provide good dark matter candidates and the mediating Z' boson couples to both the SM and HV, allowing it to be probed experimentally. While HV theories can provide specific models predicting Z' production and decays to SM particles, it is particularly useful to simplify these theories in a way such that searches for Z' become model-independent at experiments. Specifically, if a Higgs-like scalar, S, is added to the SM and spontaneously breaks the $U(1)'$ symmetry, giving the Z' its mass, the number of additional parameters introduced by the theory is then more limited. Most importantly, the couplings of the Z' to SM particles determine the decay length ($c\tau$) of the Z' and the scale of the $U(1)'$ symmetry breaking determines its mass.

The simplest $U(1)'$ extension is one that results in a Z' that has identical SM couplings to the standard Z boson [23]. The resulting "sequential" Z', or Z'_{SSM}, is prompt and is severely constrained by experiments [24, 25]. Thus, more complex $U(1)'$ extensions to the SM have been developed to allow for non-SM-like Z' couplings and to access a wider parameter space.

3.2 Exotic $U(1)'$ Extensions

Several popular theories predicting an exotic Z' have been hypothesized with different Z' couplings to the SM and with additional BSM motivations. In any case, these theories typically predict SM couplings for the Z' that result in prompt Z' decaying to conventional particle topology. One example is $U(1)_{B-L}$ extensions, where the new gauge transformations conserve $B - L$, for baryon number, B, and lepton number L, and the new Z' couples to quarks and leptons [26]. These extensions are included in Grand Unification Theory (GUT), which posits that the three fundamental forces covered by the SM unify as one force at very high energies and is considered an intermediate step toward a unified force including gravity at even higher energies. It also provides a mechanism for observed nonzero neutrino masses by adding massive, right-handed neutrinos. Other examples include theories motivated by the E_6 GUT, where the SM is extended by two $U(1)'$ symmetries [23]. Popular benchmark theories in this group include $U(1)_\chi$, $U(1)_\psi$, and $U(1)_\eta$, each of which are anomaly free, meaning that any loop diagrams which would break the gauge invariance of the theory are cancelled out [27]. While these theories each offer interesting scenarios for Z' production and are motivated by BSM physics, no evidence of any such prompt Z' has been found at experiments [24, 25]. Indeed, Figure 3.1 shows, as an example, that strong limits have been placed on prompt Z' decaying to leptons in different benchmark models up to 4-5 TeV. Due to the limits placed on prompt $Z' \to \ell^+\ell^-$ constraining these benchmark models quite strongly, it is imperative that models with less conventional signatures be considered to probe Z' with this decay mode.

3.3 $U(1)_{L_\ell - L_{\ell'}}$ Extensions and Long-Lived Z'

Until now, $U(1)'$ extensions where the Z' has couplings to both quarks and leptons have been considered. However, exlusive Z' decays to oppositely charged leptons provide a particularly clean detector signature, making them a desirable probe for Z' searches and is the focus of this thesis. Unfortunately, as evidenced in Figure 3.1, prompt $Z' \to \ell^+\ell^-$ is heavily constrained. Searching for the dilepton Z' decay mode, therefore, necessitates the exploration of more unconventional signatures. This thesis examines the long-lived regime, where the Z' has a macroscopic decay length and is far less constrained by limits placed by existing searches. Long-lived particles are not exotic in and of themselves, as

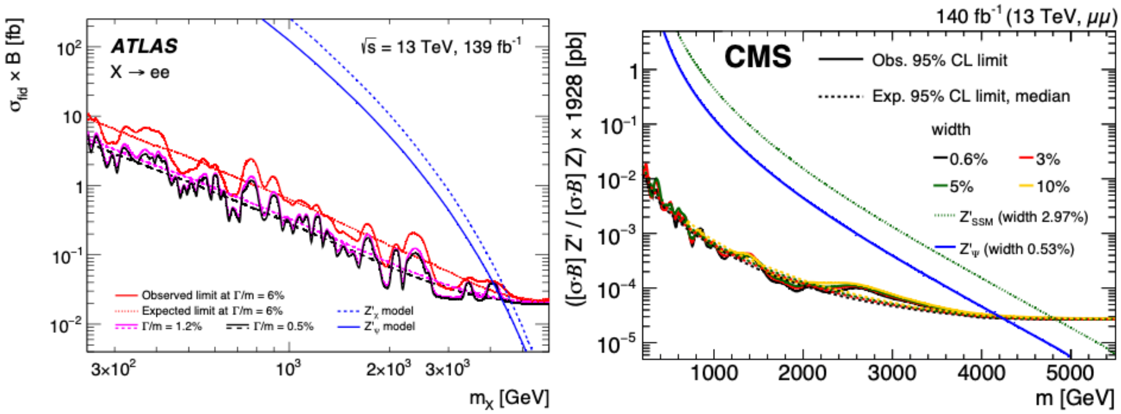

Figure 3.1: Upper limits on the cross section for prompt Z' production times branching fraction for $Z' \to e^+e^-$ (left, ATLAS [24]) and $Z' \to \mu^+\mu^-$ (right, CMS [25]) as a function of the Z' mass. Limits are presented for benchmark models $Z'_{\chi/\psi}$ and Z'_{SSM} [27].

they exist within the SM with examples such as b-hadrons and kaons. BSM models with small couplings, small mass splittings, or off-shell decays can produce similarly long-lived exotic particles, including the Z' considered here. Conveniently, the $U(1)_{L_\ell - L_{\ell'}}$ class of extensions to the SM provide a theoretical mechanism by which the Z' both couples to leptons (ℓ and ℓ') dominantly and can be long-lived, accessing a far less explored parameter space for the Z'. Furthermore, these extensions are anomaly free and are motivated by their consistency with the relic abundance of dark matter in freeze-out scenarios where, in particular, these models can dominantly decay to a dark matter fermion, χ [28]. For prompt decays, $L_\mu - L_e$ and $L_e - L_\tau$ coupling models are severely constrained by Large Electron-Positron Collider (LEP), but $L_\mu - L_\tau$ remains unconstrained and is detectable at the LHC as a decay to a $\mu\mu$ pair. The Z' can become long-lived for the appropriately small couplings/decay widths or large S masses, where S is the parent particle from Section 3.1. Thus, at particularly large Z' decay lengths, $L_\mu - L_e$ and $L_e - L_\tau$ models become less constrained, allowing for decays to ee pairs as well. As mentioned in Section 3.1, it is useful to remain model-independent while searching for Z'. Yet, having a production mechanism and leptonic decay mode theoretically motivated for the Z' provides a nice model for which results can be interpreted and compared to as a benchmark while still being able to set limits on other generic neutral high-mass resonances.

Chapter 4
The Large Hadron Collider and the ATLAS Experiment

With earlier collider experiments such as LEP and the Tevatron largely unsuccessful at finding evidence of BSM high-mass resonances, the LHC at the European Organization for Nuclear Research (CERN) was designed to access particle physics at even higher, unexplored energies [29]. The ATLAS (A Toroidal LHC Apparatus) detector is on of the four major experiments at the LHC and is a multipurpose detector designed to study EWSB and BSM physics [30]. Together, the LHC and the ATLAS detector form the experimental apparatus used to search for the high-mass resonances that are the target of the analysis presented in this thesis. Details of the LHC are discussed in Section 4.1 and the ATLAS detector and its subsystems are described in Section 4.2.

4.1 The Large Hadron Collider

Located near Geneva, Switzerland, the LHC is the world's largest and most energetic synchrotron accelerator and is located in a tunnel roughly 100 m underground, beneath the French-Swiss border. The LHC is the successor of the LEP experiment [31], occupying its old tunnels, and has circular beam pipes with a circumference of 27 km. The collider accelerates counterrotating beams of particles, bringing them to collision at four different Interaction Points (IPs). Starting in 2010, the LHC operated at $\sqrt{s} = 7$ TeV during early Run I and has a design energy of roughly $\sqrt{s} = 14$ TeV, corresponding to 7 TeV of energy per particle beam. The focus of this thesis is the data collected from proton-proton (pp) interactions collected at $\sqrt{s} = 13$ TeV during Run II (2015-2018).

The protons used in the LHC beams begin as Hydrogen gas [32], are stripped of their electrons, and enter the injection chain [33], where a series of several smaller accelerators bring the protons up to energies as high as 450 GeV before being injected into the LHC. This series of accelerators include a linear accelerator (LINAC2), the Proton Synchrotron Booster (PSB), the Proton Synchrotron (PS), and the Super Proton Synchrotron (SPS)

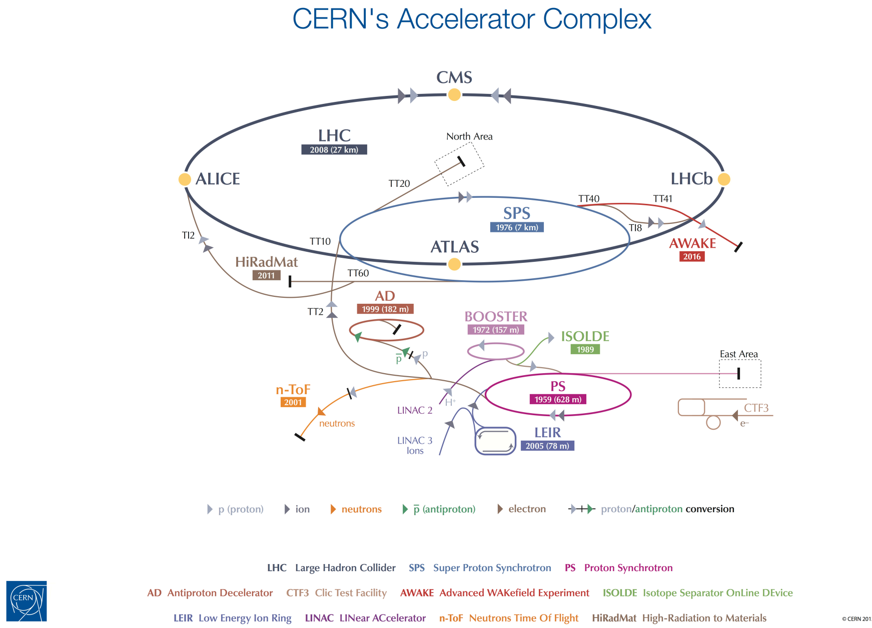

Figure 4.1: The CERN accelerator complex [34].

and sequentially increase the energy of the protons before injecting them into the LHC at one of two interaction regions, as shown in Figure 4.1.

The four main experiments are ATLAS [30], CMS [35], LHCb [36], and ALICE [37] and are located at four of the eight IPs along the LHC ring. The two largest collaborations are the ATLAS and CMS detectors, which are both general purpose experiments and work together to ensure reproducibility of results as was done in the 2012 Higgs boson discovery [1, 2]. Two of the other IPs are responsible for collimating the particle beams using the LHCs strong magnets to protect the accelerator from stray particles. The superconducting radio-frequency (RF) cavities are responsible for accelerating the proton beams to their final energy of 6.5 TeV and occupy their own IP [38].

The number of events per second observed at any of the detector experiments depends on the luminosity delivered by the LHC. Specifically,

$$\frac{dN}{dt} = \mathcal{L} \times \sigma, \tag{4.1}$$

for cross-section, σ, describing the probability of a particular physics process occurring and instantaneous luminosity, $\mathcal{L}$, describing the rate at which data is delivered by the LHC as determined by the properties of the beam and proton bunches. While the original design peak luminosity of the LHC was 1×10^{34} cm^{-2}s^{-1}, the instantaneous luminosity peaked at values over 2×10^{34} cm^{-2}s^{-1} in 2017 and 2018 due to improvements made to the proton

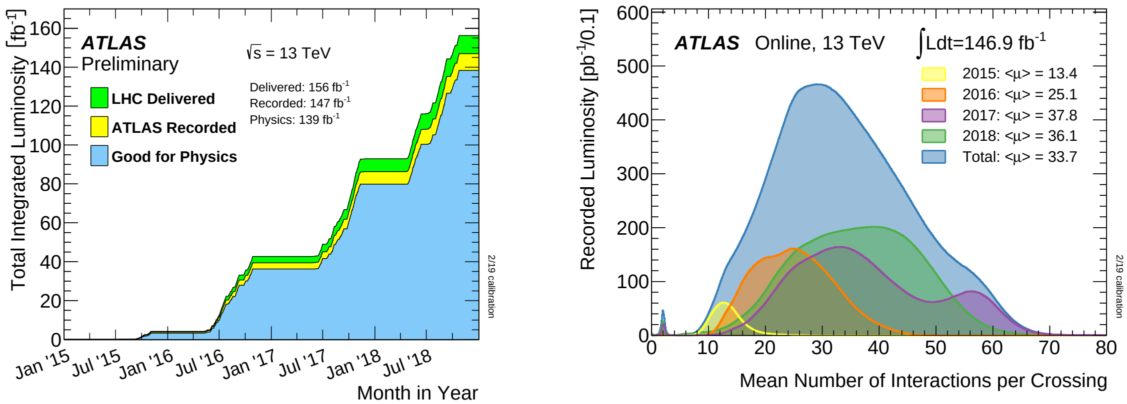

Figure 4.2: The integrated luminosity versus time (left) delivered to (green), recorded by (yellow), and deemed good for physics analyses by (blue) the ATLAS experiment and the luminosity-weighted distribution of the mean number of interactions per bunch-crossing (right) for the $\sqrt{s} = 13$ TeV Run II pp collision data [39].

beams [39]. Integrating Equation 4.1 over time yields:

$$N = \mathcal{L}_{int.} \times \sigma, \tag{4.2}$$

for integrated luminosity, $\mathcal{L}_{int.} = \int \mathcal{L}dt$, representing the total amount of data collected over the amount of time. Thus, the number of events observed at an experiment, N, can be predicted for its theoretical cross-section, σ. For full Run II data, the ATLAS experiment certified 140 fb^{-1} of the data delivered by the LHC passing quality criteria for use in physics analyses, as shown in Figure 4.2[1].

Due to the large number of protons in each bunch used to achieve the desired luminosity, there are multiple distinct pp collisions in each bunch crossing, an effect known as pileup. Unfortunately, a vast majority of these collisions result in soft, inelastic scattering events that produce low-energy particles. Heavy exotic particles in BSM are produced in the hard-scatter process. It is imperative, then, that any detector experiment be able to resolve the particles resulting from the hard-scatter process from those resulting from pileup in order to identify interesting physics. Pileup is quantified as the time averaged number of interactions per bunch crossing, $\langle\mu\rangle$, and the luminosity-weighted distribution of $\langle\mu\rangle$ for each year of ATLAS data taking in Run II is shown in Figure 4.2.

[1] Figure 4.2 shows a final luminosity of 139 fb^{-1} [40]; the final Run 2 measurement is 140 ± 1.2fb^{-1} [41].

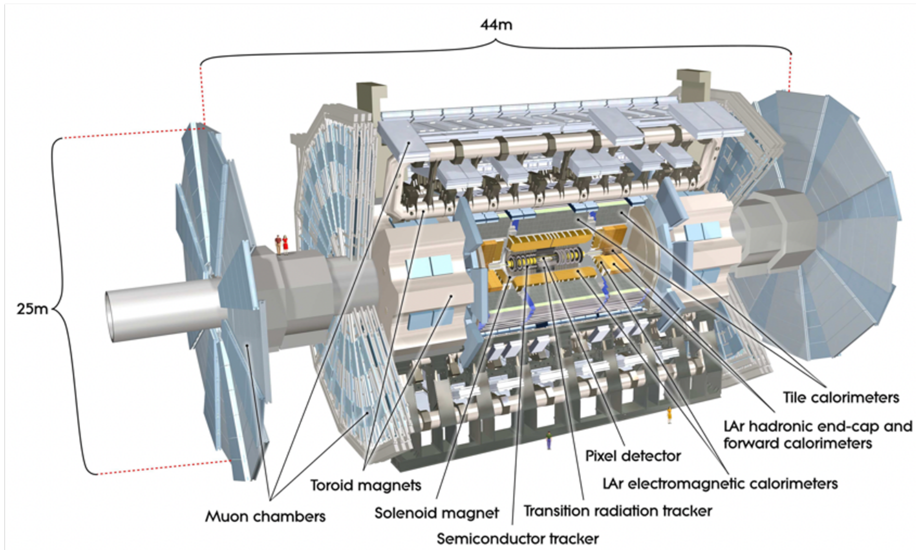

Figure 4.3: Cutaway of the ATLAS detector [30].

4.2 The ATLAS Experiment

The ATLAS detector is the largest particle detector ever constructed, measuring 46 m long, 25 m in diameter and weighing roughly 7000 tons [30]. It is one of the two multipurpose detectors at the LHC, the other being the CMS experiment, both of which participated in the discovery of the Higgs boson in 2012 and are engaged in many BSM searches. The ATLAS detector covers almost 4π of solid angle around the pp interaction point with its three layers of subdetectors: the ID, the electromagnetic and hadronic calorimeters, and the muon spectrometer (MS). These subsystems combine to provide excellent coverage of the wide array of interesting final states that can result from the pp collisions by identifying specific types of particles in a sequential way as they traverse the coaxial layers. The barrel region and two end-caps define the general geometry of the ATLAS detector, as shown in Figure 4.3. Details of each subsystem are discussed in the following sections. The coordinate system and the ATLAS magnet system are also detailed in Sections 4.2.1 and 4.2.5, respectively.

4.2.1 The Coordinate System

The origin of the ATLAS detector's right-handed coordinate system lies at the nominal IP along the beam line at the center of the detector with the beam direction defining the z-axis. The $x - y$ plane is perpendicular to the beam line and defines the transverse direction, where the positive x-axis points from the origin toward the center of the LHC ring and the positive y-axis points from the origin vertically upward toward the surface. The positive

z-axis points counterclockwise around the beam line and, with this coordinate system, the detector has forward-backward symmetric cylindrical geometry. The coordinates defining this cylindrical geometry are $R_{xy} = \sqrt{x^2 + y^2}$, ϕ, the azimuthal angle from the x-axis around the z-axis, and z. The spherical polar angle, θ, is the angle from the z-axis and is conveniently expressed as pseudo-rapidity, $\eta = -\ln(\tan\frac{\theta}{2})$, to take advantage of the cylindrical symmetry where $\theta = 0$ is along the positive z-axis and $\theta = \frac{\pi}{2}$ is in the transverse plane, but $\eta = 0$ is in the transverse plane and $\eta = \pm\infty$ is along the postive/negative z-axis. Pseudo-rapidity is also useful because it is Lorentz invariant under boosts for massless particles along the z-axis and approximates the rapidity, $y = \frac{1}{2}\ln(\frac{E+p_z}{E-p_z})$, in the massless or ultrarelativistic limit. For any two object system, their angular separation, or opening angle, are defined as $\Delta R = \sqrt{\Delta\eta^2 + \Delta\phi^2}$, which is also Lorentz invariant for massless particles. Finally, momentum and energy in the transverse direction, $p_T = p\sin\theta$ and $E_T = E\sin\theta$, are particularly useful quantities as the initial energy in the transverse plane is zero and, for a momentum and energy conserving collision system, the summed transverse quantities of all the particles after the collision must also sum to zero. Thus, it is standard for particles to be described by (p_T, η, ϕ).

4.2.2 The Inner Detector

The ID is the innermost subdetector, covering the region $|\eta| < 2.5$ and encompassing the beam pipe. Charged particles are tracked by the ID as their trajectories bend in the 2 T magnetic field produced by the central superconducting solenoid encasing the subdetector. The magnetic field is parallel to the beam line and the curvature of the bending trajectories determine the charged particles' momentum and electrical charge. The ID has three subsystems, the Pixel tracker, the semiconductor tracker (SCT), and the transition radiation tracker (TRT), with each containing the cylindrical barrel and two end-cap disks, as shown in Figure 4.4. These high granularity subdetectors work in conjunction to provide the high resolution momentum and vertex reconstruction necessary for long-lived particle searches as discussed in Sections 5.1.

Pixel Detector

The Pixel detector constitutes the innermost layers of the ATLAS tracking system and has the highest granularity and number of readout channels [42]. The Pixel detector consists of silicon semiconductor sensors, called pixels, and is segmented into four concentric barrel layers and three end-cap disks, covering the region $|\eta| < 2.5$. These pixels are responsible for registering any electrical currents generated by a charged particle traversing the modules as hits in space representing points along the particle's trajectory. The combined barrels and disks consist of over 80 million rectangular pixels of size 50 μm $\times$ 400 μm with spatial

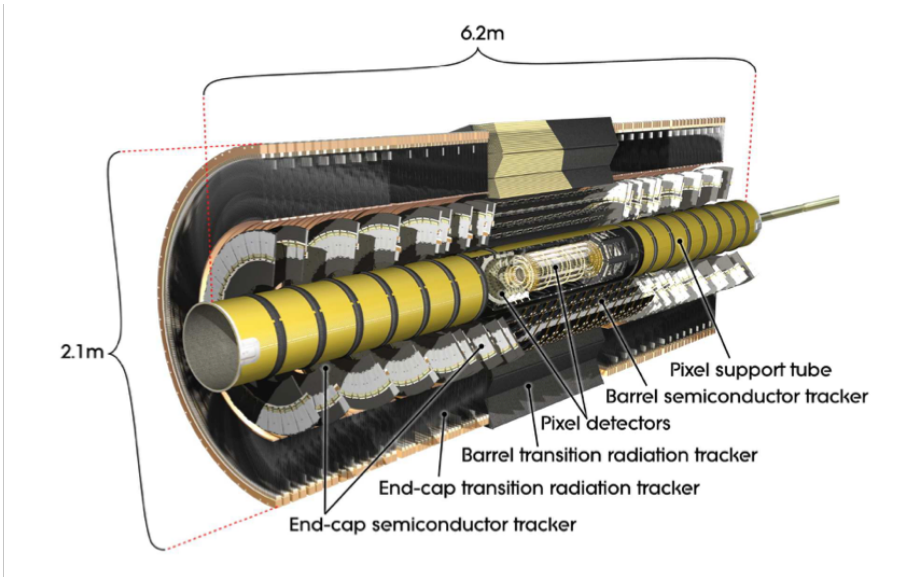

Figure 4.4: Cutaway of the ATLAS inner detector [30].

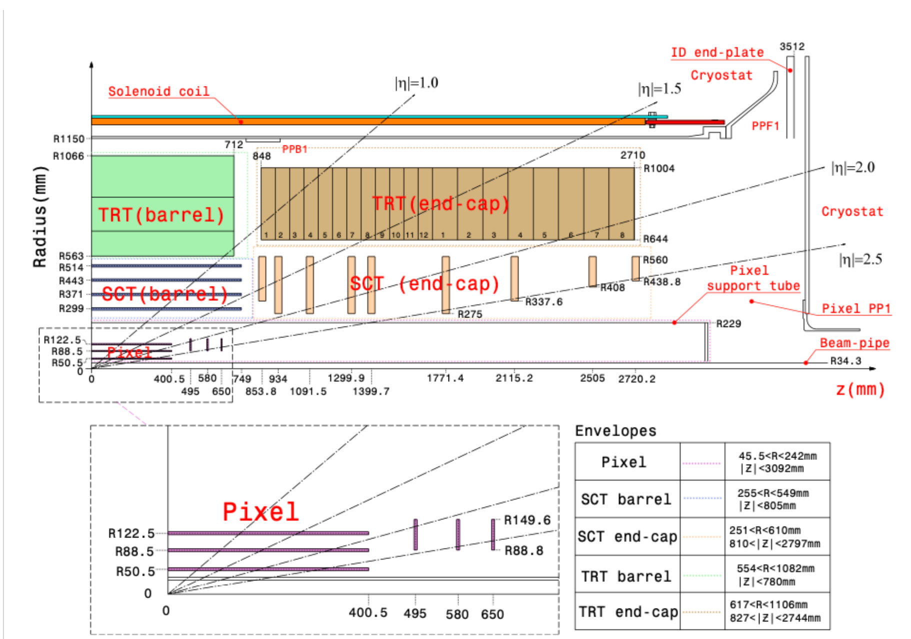

Figure 4.5: Quarter-section schematic of the ID in the R-z plane [30].

resolutions of 10 μm in the transverse plane and 115 μm in z. Prior to the start of Run II, the Insertable B-Layer (IBL) [43] was installed inside the innermost pixel layer (B-layer) to help recover resolution lost from radiation damage from Run I and prepare for the upcoming increase in pile-up. The IBL is comprised of an additional 12 million pixels of size 50 $\mu\text{m} \times 200$ μm with spatial resolutions of 8 μm in the transverse plane and 40 μm in z. Providing a fourth hit in the Pixel detector, the improvements from the IBL installation are imperative for secondary vertex reconstruction in long-lived particle searches. The Pixel detector with its subsystems and dimensions is shown in Figure 4.5.

Semiconductor Tracker

The SCT is a tracking subsystem also consisting of silicon sensors and surrounds the Pixel detector, covering the region $|\eta| < 2.5$. The SCT, unlike the Pixel detector, consists of over 6 million double-sided silicon strips of size 80 $\mu\text{m} \times 12$ cm in four barrels [44] and nine disks [45]. Each strip is tilted by 40 mrad to provide two-dimensional position measurement with a resolution of 17 μm in the transverse plane and 580 μm in z. This rotation is motivated by the positioning of the strips parallel/perpendicular to the beam axis, that would otherwise restrict spatial information to the transverse/z-ϕ plane in the barrel/end-cap region. The SCT provides eight additional hits for transverse momentum measurements and vertex reconstruction. The detector schematic is shown in Figure 4.5.

Transition Radiation Tracker

The TRT is the outermost subsystem of ID and covers the region $|\eta| < 2.0$. The TRT consists of straw tubes filled with a 70%/27%/3% mixture of Xe/CO_2/O_2 gas surrounding an anode central wire. Charged particles traversing the tubes ionize the gas, creating a cascade of electrons drifting toward the central wire that provide a measurement of the distance of closest approach of the particles with a resolution of roughly $\sim$130 μm [46]. There are 52,544 straw tubes parallel to the beam axis in the barrel region with a length of 144 cm, covering $|\eta| < 1.0$, and 122,800 straw tubes in the radial direction in the end-cap region with a length of 39 cm, covering $1.0 < |\eta| < 2.0$. The TRT provides another 36 hits on average in the transverse/z-ϕ plane in the barrel/end-cap region. This additional information helps to resolve tracks from charged particles that may not originate from the IP as in many long-lived analyses. The dimensions of the TRT are provided in Figure 4.5.

One additional feature of the TRT is its ability to identify types of charged particles, an ability unique with respect to the rest of the ID subsystems. Polypropylene fibers are used to fill the space between the straw tubes such that charged particles traversing the material emit photons via transition radiation that are absorbed by the gas mixture, amplifying the readout signal. This effect depends on the Lorentz factor and mass of the charged particles,

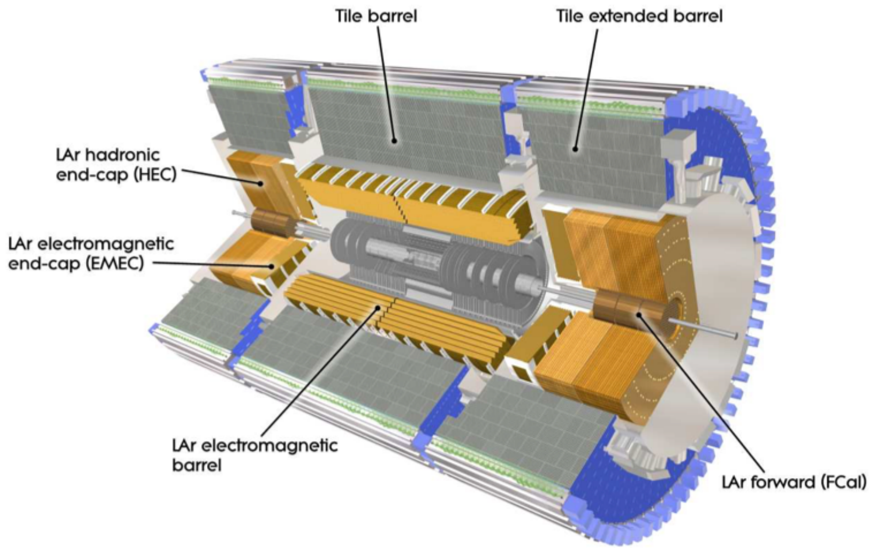

Figure 4.6: Cutaway of the ATLAS calorimeter system [30].

where, specifically, this effect is stronger for electrons, distinguishing them from charged hadrons, because of their relatively large Lorentz factor [47].

4.2.3 The Calorimeters

The calorimeters [48] are the next major ATLAS subsystem, located between the ID and MS, surrounding the central solenoid. The calorimeters are further divided into subsystems, the Liquid Argon (LAr) calorimeters [49] and the tile calorimeters [50], as shown in Figure 4.6. Generally, the calorimeters are responsible for measuring the energy deposits of both charged and neutral particles as they traverse the detector material covering $|\eta| < 4.9$. Both the LAr and tile calorimeters are sampling calorimeters with layers of alternating materials intended to interact with the incoming particles and measure the energy lost from the resulting particle showers. The passive, or absorbing, layers initiate electromagnetic or hadronic showers as a result of interactions with the dense material that forms the layer. The electromagnetic calorimeter (EMC) measures the energy of the induced electromagnetic showers while the hadronic calorimeter measures the energy of the induced hadronic showers. The only particles that typically pass through the calorimeters are muons and neutrinos while all others are stopped, depositing a portion of their energy in the subsystem. The high energy and position resolution measurements from the calorimeters are also used in the trigger system. Together, the two calorimeter subsystems aid long-lived particle searches by providing additional spatial and kinematic information for objects passing through the ID with potentially limited information (i.e. electrons from displaced decays).

Electromagnetic Calorimeter

The EMC is the first collection of calorimeters located outside the central solenoid magnet and is designed to completely stop a vast majority of photons and electrons while also measuring the magnitudes, shapes, and positions of their energy deposits. It is composed of the EM Barrel (EMB) calorimeter and EM End-Cap calorimeter (EMEC), which are both comprised of LAr calorimeters and cover the regions $|\eta| < 1.475$ and $1.375 < |\eta| < 3.2$, respectively. The EMB is divided into two identical half-barrels with a 4 mm gap at $z = 0$ and gives full ϕ coverage with sixteen modules each covering $\Delta\phi = 22.5°$, using accordion geometry without any gaps. Each of the end-caps is divided into two coaxial wheels with eight modules coviering $1.375 < |\eta| < 2.5$ and $2.5 < |\eta| < 3.2$. In the transition region of $1.375 < |\eta| < 1.52$, also known as the crack region, there is a significant amount of inactive material allowing for servicing of the ID that can lead to inefficiencies in reconstructing and identifying objects that pass through the region.

The absorber material for the LAr calorimeters is lead, due to its heavy nucleus, which induces electromagnetic interaction with the incident electrons and photons. The active material, the namesake of the LAr calorimeters, is liquid argon, which measures the electron and photon energy deposits. These liquid argon layers are also called sampling layers as the LAr calorimeters are only capable of measuring a small fraction of the total energy deposited in each layer as a portion is lost in the absorber material. Naturally, then, first layer of the barrel LAr calorimeters in the region $|\eta| < 1.8$ is called the presampler and is a thin layer of liquid argon designed to correct for energy lost by electrons and photons in the ID material without using an absorbing layer.

In each absorbing layer, electrons and photons interact with the heavy nuclei of the dense lead material, resulting in a bremsstrahlung and pair-production EM shower that is then amplified and measured in the sampling layer. In the precision region $|\eta| < 2.5$, each of the LAr modules is divided into three layers, where the first layer is segmented with fine spatial granularity to provide high resolution information for photons that, due to their neutral electrical charge, do not have ID tracks. This layer helps to distinguish single photons from multi-photon decays such as $\pi^0 \to \gamma\gamma$. The second layer is the longest, collecting a majority of the energy deposit. Finally, the third layer is the shortest, coarsest layer, collecting the tail of high energy EM showers and estimate the energy that leaks past the EMCs. The LAr modules have an energy resolution for the EMC of $\frac{10\%}{\sqrt{E/\text{GeV}}} \oplus 0.7\%$. The total thickness of the LAr modules in the precision region ranges from 22 X_0 to 33 X_0 for radiation length, X_0 (in units of g cm^{-2}), depending on $|\eta|$, while the modules in the end-caps range from 24 X_0 to 38 X_0 [51]. Covering this large number of radiation lengths effectively achieves the EMC's goal of stopping all electrons and photons traversing the material.

Hadronic Calorimeter

Due to their heavier masses, hadrons are far less likely to interact with the material of the EMC LAr modules, thus reaching the hadronic calorimeter. Similarly designed, the hadronic calorimeter is designed to stop the hadrons passing through the EMC while measuring their energy deposits as well as any missing transverse energy (E_T^{miss}). It is composed of the tile calorimeter (TileCal), the hadronic end-cap calorimeter (HEC) and the forward calorimeter (FCal).

The TileCal covers the range $|\eta| < 1.7$, divided into two components, the central barrel region $|\eta| < 1.0$ and the extended barrel region $0.8 < |\eta| < 1.7$. Each component consists of 64 wedge-shaped modules arranged in three radial layers, where each module uses alternating layers of steel as the absorber material and plastic scintillators as the active material. Similar to EM showers, hadronic showers are produced by hadrons interacting with the dense absorber material. The resulting particle showers, which are mostly pions, interact with the plastic tiles to produce scintillation light that is then passed to photomultiplier tubes through wavelength-shifting fibers that read out the cluster hit with an energy resolution $\frac{50\%}{\sqrt{E/\text{GeV}}} \oplus 3\%$.

The HEC and FCal cover $1.5 < |\eta| < 3.2$ and $3.1 < |\eta| < 4.9$, respectively, and are both comprised of LAr calorimeters [52]. The HEC is composed of four layers, two wheels per end-cap, with each layer consisting of 32 wedge-shaped LAr modules using copper as the absorber material instead of lead. The FCal is located between the beam pipe and the HEC wheels in three layers along the beam line with each layer using liquid argon as the active material, but the absorber materials depending on the targeted particle types. The first layer uses copper as the absorber material while the next two layers use tungsten to stop electromagnetically and strongly interacting particles, respectively. The hadronic calorimeter in the barrel and forward regions are 9.7λ and 10λ thick, respectively, for nuclear interaction length, λ, thus effectively stopping the strongly interacting particles passing through the material.

4.2.4 The Muon Spectrometer

The outermost subdetector of the ATLAS experiment is the MS, the system responsible for identifying muons and measuring their transverse momenta [53]. Due to their relatively heavy mass and electromagnetically interacting nature, muons can pass through the calorimeter systems without losing much of their energy[2], necessitating this MS system located outside the other subdetectors. The MS is divided into tracking components consisting of Monitored Drift Tube (MDT) chambers or Cathode Strip Chambers (CSCs) and triggering components consisting of Resistive Plate Chambers (RPCs) or Thin Gap Cham-

[2] The probability of bremsstrahlung $\propto 1/m^2$

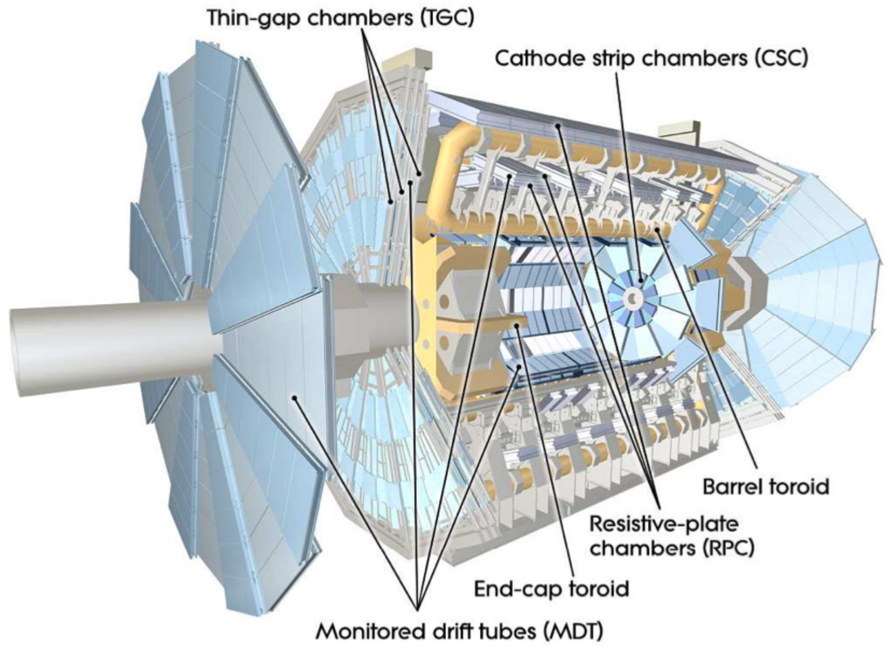

Figure 4.7: Cutaway of the ATLAS muon spectrometer [30].

bers (TGCs). The combined subsystems provide nearly full ϕ coverage with a small gap at $z = 0$ for ID access and service. Similar to the ID, the large toroid magnets of Section 4.2.5 surrounding the MS bend the trajectory of the muons, allowing for the measurement of the muons electrical charges and transverse momenta with resolution $\sigma_{p_T}/p_T = 10\%$.

The combined tracking systems cover the region $|\eta| < 2.7$ and the combined trigger systems cover the more restricted region $|\eta| < 2.4$. The magnetic field is provided by the barrel toroid in the region $|\eta| < 1.4$ and the end-cap toroids in the region $1.6 < |\eta| < 2.7$ with the transition region $1.4 < |\eta| < 1.6$ having a combined magnetic field from both toroidal systems. In addition to the information from the tracking systems, which measure the muons η and p_T, the triggering systems provide coarse momentum measurements, orthogonal spatial measurements in ϕ, and bunch crossing identification. The performance of the MS is crucial in long-lived particle searches with leptonic decay modes as the resulting muons often require both the tracking and trigger information from the MS to be reconstructed due to the limitations of the ID to independently reconstruct objects originating from points well beyond the IP. The combined MS subsystems are shown in Figure 4.7.

Monitored Drift Tube Chambers

The tracking subsystem of the MS is mainly provided by the MDT chambers with high-precision momentum measurements in the region $|\eta| < 2.7$, except in the innermost end-cap layer, where the coverage is limited to $|\eta| < 2.0$ [54]. The MDT chambers are arranged in three cylindrical barrel layers covering the region $|\eta| < 1.1$ and three parallel end-cap wheels covering the region $1.1 < |\eta| < 2.7$ with each comprised of chambers of drift tubes filled with a 93%/7% Ar/CO_2 gas mixture. Each drift tube is 3 cm in diameter and uses a tungsten-rhenium anode central wire and uses the same principles as the TRTs from Section 4.2.2 to measure the distance of closest approach of the incident muons with a precision of 80 μm. In the MDT chambers, however, the drift tubes are arranged perpendicular to the beam line in the barrel layers and tangential to the beam line in the end-cap wheels, providing measurements of the muon trajectory curvatures in the η-z plane with a spatial resolution of 35 μm. Each MDT chamber of six to eight drift tube layers is divided into two multilayers of three to four drift tube layers used to independently build partial muon tracks, called tracklets, during the muon reconstruction.

Cathode Strip Chambers

The second component of the MS tracking subsystem is the CSCs, extending the MDT coverage to $2.0 < |\eta| < 2.7$ in the innermost end-cap wheel [55]. In this region, the rate of muons far exceeds the maximal 150 Hz/cm^2 counting rates of the MDT chambers. As a result, the CSCs, with a much higher operational hit rate of up to 1 kHz/cm^2, are used to supplement the tracking information provided by the MDT chambers. Each of the CSCs is a multiwire proportional chamber with anode wires and cathode strip planes, filled with an 80%/20% Ar/CO_2 gas mixture. The multiwires are aligned radially while the cathode strips are aligned in alternating parallel and perpendicular directions with respect to the wires. This provides high-precision spatial measurements in η and ϕ with resolution 60 $\mu\text{m} \times 5$ μm. Each end-cap contains eight small and eight large chambers with four CSC planes in each chamber. The CSCs provide a large number of independent 2-dimensional spatial measurements in the region not covered by the MDT chambers.

Resistive Plate Chambers

The RPCs are the barrel component ($|\eta| < 1.05$) of the MS's triggering subsystem [56]. Similar to the MDT chambers in the barrel region, the RPCs are arranged in three concentric cylindrical layers with each chamber consisting of two parallel resistive plates separated by a 2 mm gap filled with a $C_2H_2F_4$-based gas mixture and surrounded by a readout strip on either side. Muons traversing the RPCs ionize the gas with the external readout strips recording any avalanches in the gaps as a spatial measurement in z on one side and ϕ on the other. In each layer the RPCs are configured in sixteen paired units around ϕ with each layer located either just inside or outside an MDT barrel layer. Thus, the RPCs provide six additional measurements for all three layers with spatial resolution of 10 mm and time resolution of 1.5 ns. The two innermost layers are used for the low-p_T muon triggers, requiring three of four hit coincidences, and the third is used for the high-p_T triggers, requiring one of two coincidences.

Thin Gap Chambers

The end-cap component of the triggering subsystem, covering the region $1.05 < |\eta| < 2.4$, is the TGCs, which additionally provide spatial measurements in ϕ to $|\eta| < 2.7$. Similar to the CSCs, the TGCs are multiwire proportional chambers filled with a 55%/45% CO_2/n-C_5H_{12} gas mixture, providing measurements in the radial, bending coordinate and ϕ with resolutions 7 mm and 2 mm, respectively. The TGCs are arranged in four layers of twelve sectors in each end-cap and coincident hits are used for the muon triggers, similar to the RPCs, with time resolution of 4 ns.

4.2.5 The ATLAS Magnet System

The ATLAS detector has two distinct superconducting magnet systems: the central solenoid and the toroidal system. Both systems use liquid helium to cool below 5 K to achieve superconductivity.

Central Solenoid Magnet

The central solenoid [57] is between the ID and calorimeters, providing a 2 T magnetic field that bends the trajectory of charged particles in the transverse plane inside the ID. As discussed in Section 4.2.2, this bending is critical for measurement of the charged particles' electrical charges and transverse momenta. At 2.4 m in diameter and 5.3 m in length, it is also imperative that the solenoid minimizes its radiative thickness as it lies before the calorimeter systems as detailed in Section 4.2.3.

Toroid Magnets

The toroidal system is further divided into one barrel and two end-cap magnets, all outside the MS. Providing a magnetic field of approximately 0.5 T in the barrel and 1.0 T in the end-caps, the toroids allow for muon momentum measurements. Measured at 25.3 m in length with an outer diameter of 20.1 m, the barrel toroid is composed of eight air-core coils with 120 turns of a Niobium-Titanium alloy. The end-cap is 5 m long, has an outer diameter of 10.7 m, and has eight air-core coils with 116 turns of the same alloy.

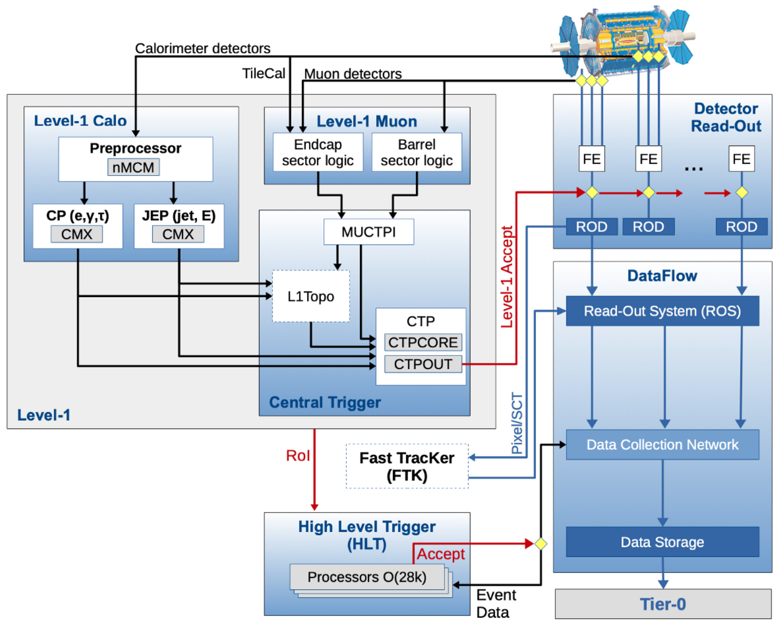

Figure 4.8: A schematic overview of the ATLAS trigger and data acquisition system in Run II including the planned Fast TracKer (FTK) that was cancelled [58].

4.2.6 The ATLAS Trigger System

The LHC collides proton bunches in the ATLAS detector every 25 ns, corresponding to a crossing frequency of 40 MHz. With the roughly 100 million combined readout channels, collecting all the information from these collisions would generate a computationally untenable amount of data at a rate of more than 60 TB/s. It is, therefore, imperative to implement a system which determines the data to save and store. The need for such a system only becomes more crucial when considering the pileup rates in Figure 4.2, where a large portion of the data comes from soft interactions containing minimally interesting physics. For the ATLAS experiment, this system is a combined hardware and software effort to select potentially new and noteworthy physics at a reduced rate of 1 kHz. Specifically, the ATLAS trigger system uses the hardware-based Level 1 (L1) trigger and software-based High Level Trigger (HLT) to select events and the Data Acquisition (DAQ) system to process the information from each of the detector elements to reconstruct the selected events that are stored in Data Storage (SFO). The workflow of the ATLAS trigger and DAQ system is shown in Figure 4.8.

Level 1 Trigger

The first and hardware-based trigger is the L1 trigger, which reduces the data rate to 100 kHz and consists of the L1 calorimeter (L1Calo) and L1 muon (L1Muon) trigger systems [59]. Within 2.5 μs after the bunch-crossing, the L1 trigger accepts events with high p_T leptons, photons, jets, and large total or missing transverse energy (E_T^{miss}) based on a list of selections called the Trigger Menu [60]. The Trigger Menu is a collaborative effort by different analyses to provide signal-motivated thresholds in energy that can be used to select interesting events. The L1 trigger is also responsible for defining areas in η and ϕ, called regions-of-interest (RoIs), where it determines potentially interesting features exist. In addition to the trigger-selected events, these RoIs are also passed to the HLT.

High Level Trigger

The software-based HLT operates on events selected by the L1 trigger by further filtering the data and performing a first pass reconstruction of physics objects. The HLT uses the full granularity information in the L1-identified RoIs combined with reconstructed ID tracks to loosely identify high-p_T physics objects based on associated energy signatures. The HLT system reduces the data rate to 1 kHz, a drastic improvement from saving all events to roughly 1 in every 40000 collisions, and sends the selected events to CERN's Tier-0 computing facility for storage and reconstruction following the methodology detailed in Chapter 5.

Chapter 5
Event Reconstruction

Following the trigger selection from Section 4.2.6, several reconstruction algorithms are performed on the raw data from the subdetectors to form physics objects that represent the particles traversing ATLAS and are used by analyses to search for interesting physics. Due to the significant displacement of long-lived particle (LLP) decays, several additional reconstruction algorithms have been developed to find physics objects that do not originate close to the IP. Details of the combined standard and extended reconstruction algorithms relevant to the analysis are discussed here. In particular, these include standard and large radius tracking, primary and secondary vertexing, and electron and muon reconstruction and identification. Further details on tau, jet, and E_T^{miss} reconstruction are not considered as they are not critical to the analysis. A summary of how different particles behave in the ATLAS detector is given in Figure 5.1

5.1 Track and Vertex Reconstruction in the Inner Detector

The first and most relevant step in event reconstruction is the formation of ID tracks using detector hits from the subsystems and vertexing of these tracks to determine their origin. As discussed in Section 4.2.2, any charged particles traversing the ID will leave raw signals registered as detector hits that can be used to reconstruct the particles' trajectories and transverse momenta. These trajectories are called tracks and, when the tracks are reconstructed using only information from the Pixel, SCT, and TRT detectors, are called ID tracks. While a standard track (ST) is reconstructed assuming the track's origin is one of the primary *pp* interactions, a second tracking algorithm reconstructs tracks with particularly large impact parameters [62]. Such a track is called a large radius track (LRT) and its trajectory does not necessarily point toward the IP as its source. Both STs and LRTs are reconstructed using pattern recognition algorithms as discussed in Sections 5.1.1-5.1.2. Similarly, the entire collection of ID tracks are passed to the vertexing stage to reconstruct the primary vertex (PV) of the hard-scattering process and a second algorithm reconstructs

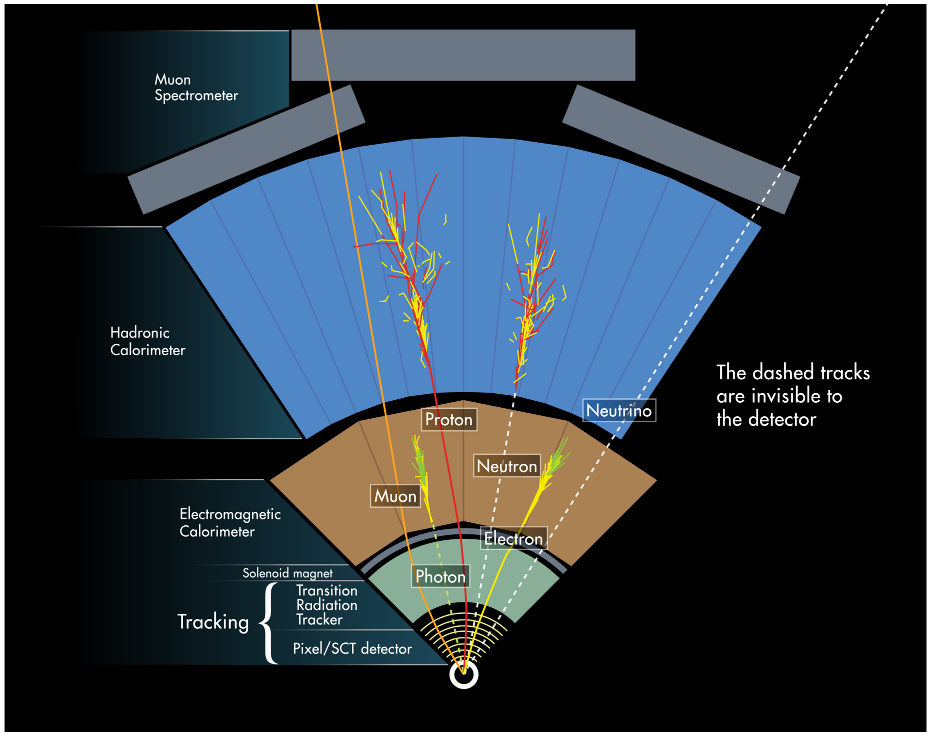

Figure 5.1: A cross-section diagram of how different particles interact with and are detected by ATLAS [61].

vertices significantly displaced from the PV [63]. Such a vertex is called a secondary vertex (SV), or displaced vertex (DV), and is the primary analysis object considered in this thesis. Details of the primary and secondary vertexing algorithms are discussed in Sections 5.1.3-5.1.4.

5.1.1 Standard Tracking

A majority of ID tracks are reconstructed using the standard ATLAS track reconstruction algorithm where two separate stages are employed to fully parameterise ST representations [64]. Each ID track is described by a set of five parameters using a perigee representation: d_0, z_0, ϕ, θ, and q/p, and each parameter is measured with respect to the PV. The first two parameters, d_0 and z_0, are the transverse and longitudinal impact parameters, respectively, and are the track's distance of closest approach to the PV in the appropriate plane. The other parameters are the azimuthal angle, ϕ, the polar angle, θ, and the ratio of the track's charge, q, to the magnitude of its momentum, p.

The standard tracking algorithm is separated into two reconstruction stages, namely, the inside-out and outside-in, or back-tracking, steps. The inside-out stage uses Pixel or SCT (silicon) hit clusters to form three-dimensional space points that are combined to form track

Table 5.1: Comparison of track requirements for standard and large radius tracking algorithms.

Reconstruction Phase	Requirement	Standard	Large Radius
Forward tracking	Min. p_T (MeV)	500	900
	Max. η	2.7	5.0
	Max. d_0 (mm)	10	300
	Max. z_0 (mm)	250	1500
Clustering	Min. unshared Si hits	6	5
	Max. shared Si modules	1	2
	Min. Si hits	7	7
	Seed extension	Combinatorial	Sequential
Back-tracking	Min. p_T (MeV)	1000	–
	Max. d_0 (mm)	100	–

seeds. Seeds are, then, filtered on quality criteria, including d_0 and z_0 requirements, and extrapolated into the outer silicon layers using an iterative algorithm to find compatible hits [65]. The track segments are passed through an ambiguity-solving algorithm that rejects fake tracks and ensures hit clusters are only associated to one track. The remaining tracks are, finally, extrapolated into the TRT, similarly searching for compatible hits. Extended tracks whose quality is improved with the new hits are kept and those whose quality decreases are reverted to their original silicon track.

The outside-in stage of standard tracking uses track segments in the TRT to extrapolate to compatible, unused hits in the silicon layers to form ID tracks that have partial coverage for displaced decays. For particles with moderately displaced decays, resulting charged particles may have insufficient silicon hits to be reconstructed by the inside-out algorithm, but still have small enough impact parameters to be reconstructed by the outside-in algorithm. A summary of the selections made by the inside-out (forward tracking), ambiguity-solving (clustering), and outside-in (back-tracking) algorithms is given in Table 5.1.

5.1.2 Large Radius Tracking

With its relatively strict impact parameter requirements, standard tracking performs remarkably well in reconstructing tracks that originated from the PV [66]. However, because these impact parameters are measured with respect to the PV, the standard tracking algorithms are not optimized for ID tracks that do not originate from the primary interaction. As a result, the large radius tracking algorithm was developed to extend the track reconstruction coverage to include highly-displaced tracks by using the same inside-out tracking strategy for unused hits and with loosened criteria [62] summarized in Table 5.1. Most notably, the requirements on d_0, z_0, and number hits allow for tracks originating from points

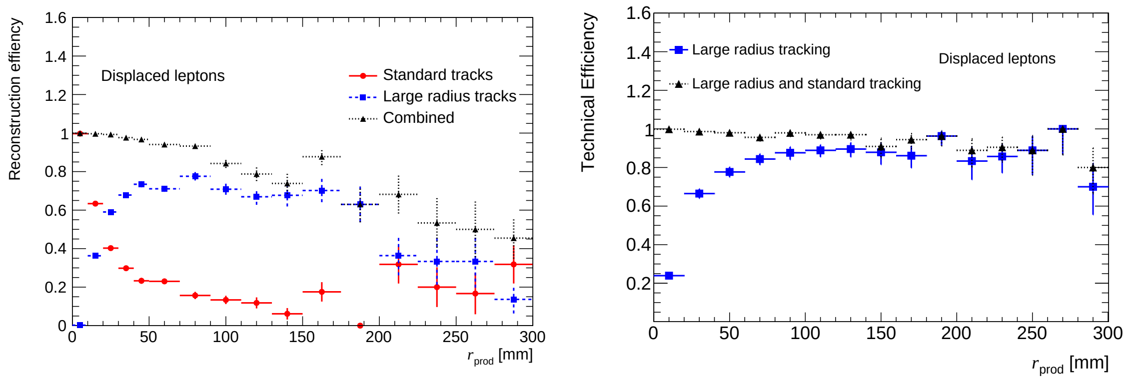

Figure 5.2: Track reconstruction (left) and technical reconstruction (right) efficiency for displaced leptons produced by long-lived particle decays as a function of r_{prod} [62].

in the ID far from the PV. The LRTs are combined with the STs to form one combined ID track collection that is passed to the secondary vertexing algorithm described in Section 5.1.4 and lepton reconstruction algorithms in Sections 5.2-5.3. Figure 5.2 shows that the LRT tracking algorithm significantly improves the overall tracking efficiency for $d_0 > 10$ mm and leads to a total efficiency of roughly 90%. The selections listed in Table 5.2 define the technical efficiency given in Figure 5.2 where the selections are applied to the truth particles to ensure that they are reasonably reconstructable and r_{prod} is the decay radius of the LLP parent particle. The large gain in sensitivity to displaced leptons from the LRT tracking algorithm is crucial for the analysis presented in this thesis.

Table 5.2: Fiducial selections for truth particles used to calculate technical tracking efficiency.

Fiducial Selections
$r_{prod} < 300$ mm
$\|\eta\| < 5$
$p_T > 1$ GeV
Number of silicon hits ≥ 7

5.1.3 Primary Vertexing

As described in Section 4.1, the hard scatter interactions are the most likely source of interesting physics in the ATLAS detector. The primary vertex reconstruction algorithm [67] is designed to use the reconstructed ID tracks to resolve the different pp interactions and identify the hard scatter process from the collision as the one with the highest sum of p_T, called the PV. Similar to the standard tracking algorithm, the primary vertexing algorithm is composed of two major steps, namely, the vertex finding and vertex fitting stages. The vertex finding algorithm uses a collection of filtered tracks to form the vertices where the selections used to filter tracks are summarized in Table 5.3 and are based on early Run II values that evolved over the course of data collection [68]. The selected tracks then undergo an iterative process of vertex fitting where two-track seed positions and compatible tracks are used to determine the best overall vertex position and rejected tracks are used as the new input for vertex finding until no selected tracks remain or no more vertices are found. The vertex with the highest summed p_T is then considered the PV and all other vertices with two or more tracks are considered pileup.

5.1.4 Secondary Vertexing

Analogous to the move from ST to LRT with the intent of targeting LLP scenarios, a secondary vertexing algorithm called `VrtSecInclusive` (VSI) was developed to reconstruct the decay vertices of such LLPs using the combined collection of STs and LRTs [63]. While SV and DV are interchangeable, DVs with oppositely charged lepton tracks are the main analysis object. The original inspiration for reconstructing DVs was to map ID material during Run 1 [69], but the VSI algorithm is designed to specifically target LLP decays. Similar to the primary vertexing algorithm, secondary vertexing begins by selecting all ID tracks (including LRTs) not used to form PVs with the selections in Table 5.3. Most notably, there is a minimum d_0 track displacement requirement as well as a 1 GeV minimum p_T requirement to reject photon conversions. Selected tracks are used to form two-track seed vertices where low quality seeds can be rejected as fakes based on constituent track hit patterns and the associated tracks are combined to form multi-track vertices that can potentially share tracks across multiple DVs. With the fake seeds rejected, the remaining DVs are refitted [70] and iteratively merged with poorly associated tracks removed to ensure that each associated track belongs to only a single DV. Finally, lower quality tracks are attached to the multi-track DVs with the criteria for both track association and track attachment given in Table 5.3. Generally none of the tracks are allowed to have hits at smaller radii than the DV position, but are required to have a hit in the nearest Pixel or SCT layer at larger radii unless it is in a disabled module.

Table 5.3: Comparison of track requirements for primary and secondary vertexing algorithms. Note that the preselection χ^2/n_{dof} cut is with respect to the beamline whereas, in the following cuts, it is with respect to the DV unless specified to be with respect to the track.

Reconstruction Phase	Requirement	Primary	Secondary
Track preselection	Min. p_T (MeV)	500	1000
	Max. d_0 (mm)	4	300
	Min. d_0 (mm)	–	2
	Max. z_0 (mm)	1000	1500
	Max. z_0 significance	5	10
	Max. track χ^2/n_{dof}	–	50
	Min. Pixel hits	1	0
	Min. SCT hits	4	2 (7 if $p_T < 20$ GeV, 6 if $p_T > 20$ GeV and 0 Pixel hits)
	Max. shared Si hits	–	2
	Min. TRT hits	–	1 (0 if Pixel hits ≥ 2, 20 if $p_T < 20$ GeV and $\|\eta\| < 1.7$)
2-track compatibility	Max. $d_{0,DV}$ (mm)	–	5
	Max. $z_{0,DV}$ (mm)	–	50
	Max. χ^2/n_{dof}	–	5
	Max. DV position (mm)	–	563
Track association	Max. track χ^2/n_{dof}	–	5
	Max. $\sigma(d_{0,DV})$	–	5
	Max. $\sigma(z_{0,DV})$	–	5
Track attachment	Min. p_T (MeV)	–	1000
	Max. track χ^2/n_{dof}	–	5
	Max. $\sigma(d_{0,DV})$	–	5
	Max. $\sigma(z_{0,DV})$	–	5

5.2 Electron Reconstruction and Identification

Electrons are reconstructed using a combination of EMC cluster and ID track information [71]. EMC seed clusters are formed by energy deposits with $E_T > 2.5$ GeV in a 0.075×0.125 window in $\eta \times \phi$ [72] and matched to ID tracks within $|\Delta\eta| < 0.05$ and $|\Delta\phi| < 0.1$ of the seed. A Gaussian-sum-filter (GSF) technique is then used to refit the matched ID tracks to account for energy lost by bremsstrahlung [73]. At this point, seed clusters with matched tracks are refit and reconstructed as electrons and those without are reconstructed as photons. Finally, nearby EMC clusters are grouped with the seed clusters to collect the energy deposits associated with the reconstructed EM object and the total energy is calibrated to account for energy lost upstream and for differences between Monte Carlo and data [74, 75].

Following reconstruction, further selections are made on electrons to discriminate against hadronic jet and material interaction backgrounds that can mimic electron signals [71]. This identification process can be imposed in a simple cut-based method or more complicated likelihood (LH) based method, each of which are utilized in the analysis as appropriate. The LH-based method uses probability density functions (PDFs) for both the signal and background to calculate the probability for an electron to pass the identification based on the discriminating variables. Identification working points with increasing threshold for the LH discriminant are *VeryLoose*, *Loose*, *Medium*, and *Tight*. Analogous working points also exist for the cut-based method. The d_0-related quality criteria imposed in the identification are a particular problem for the analysis due to the highly displaced nature of the signal electrons. While GSF tracking can lead to improved sensitivity to high-d_0 electrons, GSF tracks are not passed to primary or secondary vertexing and, unfortunately, the analysis cannot take advantage of the possible gain in efficiency. Rather, electrons are identified using an LH-based method where the standard *VeryLoose* identification working point has been modified. In order to gain sensitivity to large impact parameter electrons, cuts on d_0 and the number of Pixel hits are removed while keeping the Silicon hits requirement. Other cut-based and LH-based working points are also used for specific lepton filtering detailed in Section 6.3.2 and tag-and-probe studies detailed in Sections 7.3.3-7.3.4.

5.3 Muon Reconstruction and Identification

Muons are reconstructed by combining MS track and ID track information [76] where the composite muon resulting from the match is globally refit and matches between MS and ID tracks on opposite sides of the detector are not allowed. The ID tracks follow the same reconstruction procedure described in Section 5.1 and the MS tracks are reconstructed independent of this procedure. In the MS, track segments are formed using hits in the MDT layers with an additional coordinate provided by the RPCs and TGCs and a separate search for segments is performed using the CSCs in the region $|\eta| > 2.0$. A combinatorial search for track seeds is then performed using the segments starting in the central layers with the largest number of hits in the trigger chamber and extending to the inner and outer layers. Track candidates are formed by combining at least two segments except in the transition regions where only one high-quality segment is required. An overlap removal algorithm determines if track candidate trajectories diverge enough to share segments and, otherwise, only allows each segment to belong to one track and, finally, a track quality algorithm determines whether each hit in a track is kept based on its impact on a global χ^2 fit for the track. Similar to electrons, muons also have their momenta calibrated independently for the ID and MS tracks. The combined (CB) muons used in the analysis are reconstructed by extrapolating the track from one subdetector to the track in the other with a global refit performed and MS hits added or removed based on their impact on the fit.

Cut-based identification working points are also defined for muons as *Loose*, *Medium*, *Tight*, and *HighPt*, similar to electrons with an additional specific working point defined for muons with large transverse momenta. Requirements on the number of pixel hits are applied to muons with ID tracks by default for all working points, which can exclude highly displaced muons that would result from LLP decays. Thus, this requirement is removed, leaving only requirements on the number of SCT and TRT hits. While the central *Medium* working point is used to identify muons in tag-and-probe studies detailed in Sections 7.3.3-7.3.4, this modified configuration of the standard *Loose* working point is used to identify signal leptons in the analysis and improve sensitivity to highly displaced muons. Despite the relatively high transverse momenta of the muons from high mass LLPs, the `HighPt` muon identification working point greatly degrades signal efficiency and is, thus, not used.

Chapter 6
Data and Simulated Samples

In order to perform the analysis introduced in Chapter 1 and detailed in the following Chapter, both real and simulated samples of pp collision data at the ATLAS detector are used. The dedicated streams of Run II data that define the analysis dataset are described in Section 6.1 and the simulated signal and background Monte-Carlo (MC) samples are described in Section 6.2. Finally, the preselections performed on both data and MC samples to target dilepton DVs and refine the datasets are detailed in Sections 6.3.

6.1 Data

The analysis uses pp data collected at $\sqrt{s} = 13$ TeV in 2015-18 with an integrated luminosity of 140.1 fb^{-1}, measured using the LUCID-2 detector [40] to precision of 0.83% [41]. The luminosity and corresponding `GoodRunsList` (GRL) for each year are listed in Table 6.1. These GRLs exclude bad datasets (luminosity blocks) to ensure that the data from each year is unaffected by various detector and operations-related problems.

The main analysis datasets use a special processing, called `DRAW_RPVLL`, designed to target LLP reconstruction as detailed in Section 6.3. Traditional reconstruction (STs and PVs only) is run on datasets used in studies utilizing prompt leptons as well. After reconstruction, the datasets can be further filtered on the physics objects and activity in the events in a process known as derivation, with modifications for the analysis. The data derivations used are summarized in Table 6.2 with their associated study where the main analysis derivation, `DAOD_SUSY15`, focuses on LLP reconstruction and high-energy lepton activity and special derivations intended to select leptons for precision studies and scale factor derivation, `DAOD_EGAM1` and `DAOD_MUON1`, are also used. ATLAS metadata interface (AMI) tags are used to identify the configurations used to generate, simulate, reconstruct, and derive the different samples handled by the central processing groups. The derivation AMI tags (p-tags) used are `p5332/p4614/p4513`, as shown in Table 6.2.

Table 6.1: GRLs for 2015-2018 data at 13 TeV and the corresponding integrated luminosity.

Year	GRL	Int. Lumi [fb^{-1}]
2015	data15_13TeV.periodAllYear_DetStatus-v89-pro21-02_Unknown_PHYS_StandardGRL_All_Good_25ns.xml	3.2
2016	data16_13TeV.periodAllYear_DetStatus-v89-pro21-01_DQDefects-00-02-04_PHYS_StandardGRL_All_Good_25ns.xml	33.0
2017	data17_13TeV.periodAllYear_DetStatus-v99-pro22-01_Unknown_PHYS_StandardGRL_All_Good_25ns_Triggerno17e33prim.xml	44.3
2018	data18_13TeV.periodAllYear_DetStatus-v102-pro22-04_Unknown_PHYS_StandardGRL_All_Good_25ns_Triggerno17e33prim.xml	59.9

Table 6.2: Datasets used for analysis and their corresponding systematic error studies.

Year	Dataset	Study
2015	data15_13TeV.*.physics_Main.deriv.DAOD_SUSY15.*_p5332	Main analysis and LRT/VSI
2015	data15_13TeV.periodAllYear.physics_Main.PhysCont.DAOD_EGAM1.grp15_v02_p4614	Tag-and-probe
2015	data15_13TeV.*.physics_Main.deriv.DAOD_MUON1.*_p4513	Tag-and-probe
2016	data16_13TeV.*.physics_Main.deriv.DAOD_SUSY15.*_p5332	Main analysis and LRT/VSI
2016	data16_13TeV.periodAllYear.physics_Main.PhysCont.DAOD_EGAM1.grp16_v02_p4614	Tag-and-probe
2016	data16_13TeV.*.physics_Main.deriv.DAOD_MUON1.*_p4513	Tag-and-probe
2017	data17_13TeV.*.physics_Main.deriv.DAOD_SUSY15.*_p5332	Main analysis and LRT/VSI
2017	data17_13TeV.periodAllYear.physics_Main.PhysCont.DAOD_EGAM1.grp17_v02_p4614	Tag-and-probe
2017	data17_13TeV.*.physics_Main.deriv.DAOD_MUON1.*_p4513	Tag-and-probe
2018	data18_13TeV.*.physics_Main.deriv.DAOD_SUSY15.*_p5332	Main analysis and LRT/VSI
2018	data18_13TeV.periodAllYear.physics_Main.PhysCont.DAOD_EGAM1.grp18_v02_p4614	Tag-and-probe
2018	data18_13TeV.*.physics_Main.deriv.DAOD_MUON1.*_p4513	Tag-and-probe

6.2 Simulated Samples

Simulated MC samples are used to study efficiencies and search strategy in the analysis due to the available truth-level (generator-level) information. In particular, the signal Z' model can be studied in MC while remaining blind to the Run II data, where the analysis can be optimized in a model-independent way. Different selection criteria and background estimation techniques can also be validated using MC samples at the cost of systematic uncertainties associated with the imperfect simulation of the data.

6.2.1 Signal Samples

The analysis uses the signal Z' model detailed in Section 3.3 to define benchmark for the analysis selection and results. This model is used to inject LLP signals into the detector simulation and obtain model-independent results. The ATLAS detector performance is simulated [77] using GEANT4 [78] to produce simulated detector information that is reconstructed using the same algorithms performed on data. Signal samples are generated with AMI tag `e8092` and processed using full detector simulation with AMI tag `s3126`. Simulated minimum-bias events are included in the reconstruction to model pile-up in data and the combined events are reconstructed using AMI tags `r11915/r11916/r11891` for samples in periods mc16a/mc16d/mc16e. All signal samples undergo `DAOD_SUSY15` derivation with the `p4800` AMI tag.

The generic Z' toy model used in the previous early Run II analysis [79] has been updated to a more complex but better motivated model [28]. In the past, because the Z' was produced via $q\bar{q}$ interactions, it would also decay dominantly to quarks. With the new pair-produced model, both Z' in each event are forced to decay with a specific lifetime to the same $\ell\ell'$ for the sake of statistics, as illustrated in Figure 6.1. The Z' are generated and decayed by MADGRAPH5_aMC@NLO 2.6.7 [80] interfaced with PYTHIA 8.244 [81] with parton density function (PDF) set NNPDF2.3LO [82] and the min-bias tune `A14`. The scalar masses range from 500 to 1500 GeV, with the Z' masses varying by scalar mass and decay lengths ($c\tau$) ranging from 10 to 1000 mm. The generated samples with their dataset identifiers (DSIDs) are listed in Table 6.3.

Figure 6.2 presents the truth-level p_T and η distributions for the Z', electron children, and muon children for a representative set of Z' mc16d signal samples with a scalar mass of 1500 GeV, $e\mu$ decay mode, Z' decay length ($c\tau$) of 100 mm and mass of 250, 450, 600, and 700 GeV. As expected, the p_T of the Z' peaks at about half the scalar mass for low Z' mass and decreases as the Z' mass increases. For the η distribution, Z' has somewhat higher η as the mass increases, but the lepton children are relatively insensitive to the Z' mass. Most of the signal leptons are inside the detector acceptance in η and one notable feature is the large number of low-p_T electrons. Because the truth-child finding algorithm

Table 6.3: MC samples & DSIDs for Z' signal model. Each sample contains 10000 events.

m_S (GeV)	$m_{Z'}$ (GeV)	$c\tau_{Z'}$ (mm)	Decay Mode	DSID
500	100	10	$\mu\mu$, $e\mu$, ee	501260–501262
500	150	10	$\mu\mu$, $e\mu$, ee	501263-501265
500	200	10	$\mu\mu$, $e\mu$, ee	501266-501268
1000	200	10	$\mu\mu$, $e\mu$, ee	501269-501271
1000	350	10	$\mu\mu$, $e\mu$, ee	501272-501274
1000	450	10	$\mu\mu$, $e\mu$, ee	501275-501277
1500	250	10	$\mu\mu$, $e\mu$, ee	501278-501280
1500	450	10	$\mu\mu$, $e\mu$, ee	501281-501283
1500	600	10	$\mu\mu$, $e\mu$, ee	501284-501286
1500	700	10	$\mu\mu$, $e\mu$, ee	501287-501289
500	100	30	$\mu\mu$, $e\mu$, ee	501290–501292
500	150	30	$\mu\mu$, $e\mu$, ee	501293-501295
500	200	30	$\mu\mu$, $e\mu$, ee	501296-501298
1000	200	30	$\mu\mu$, $e\mu$, ee	501299-501301
1000	350	30	$\mu\mu$, $e\mu$, ee	501302-501304
1000	450	30	$\mu\mu$, $e\mu$, ee	501305-501307
1500	250	30	$\mu\mu$, $e\mu$, ee	501308-501310
1500	450	30	$\mu\mu$, $e\mu$, ee	501311-501313
1500	600	30	$\mu\mu$, $e\mu$, ee	501314-501316
1500	700	30	$\mu\mu$, $e\mu$, ee	501317-501319
500	100	100	$\mu\mu$, $e\mu$, ee	501320–501322
500	150	100	$\mu\mu$, $e\mu$, ee	501323-501325
500	200	100	$\mu\mu$, $e\mu$, ee	501326-501328
1000	200	100	$\mu\mu$, $e\mu$, ee	501329-501331
1000	350	100	$\mu\mu$, $e\mu$, ee	501332-501334

m_S (GeV)	$m_{Z'}$ (GeV)	$c\tau_{Z'}$ (mm)	Decay Mode	DSID
1000	450	100	$\mu\mu$, $e\mu$, ee	501335-501337
1500	250	100	$\mu\mu$, $e\mu$, ee	501338-501340
1500	450	100	$\mu\mu$, $e\mu$, ee	501341-501343
1500	600	100	$\mu\mu$, $e\mu$, ee	501344-501346
1500	700	100	$\mu\mu$, $e\mu$, ee	501347-501349
500	100	300	$\mu\mu$, $e\mu$, ee	501350–501352
500	150	300	$\mu\mu$, $e\mu$, ee	501353-501355
500	200	300	$\mu\mu$, $e\mu$, ee	501356-501358
1000	200	300	$\mu\mu$, $e\mu$, ee	501359-501361
1000	350	300	$\mu\mu$, $e\mu$, ee	501362-501364
1000	450	300	$\mu\mu$, $e\mu$, ee	501365-501367
1500	250	300	$\mu\mu$, $e\mu$, ee	501368-501370
1500	450	300	$\mu\mu$, $e\mu$, ee	501371-501373
1500	600	300	$\mu\mu$, $e\mu$, ee	501374-501376
1500	700	300	$\mu\mu$, $e\mu$, ee	501377-501379
500	100	1000	$\mu\mu$, $e\mu$, ee	501380–501382
500	150	1000	$\mu\mu$, $e\mu$, ee	501383-501385
500	200	1000	$\mu\mu$, $e\mu$, ee	501386-501388
1000	200	1000	$\mu\mu$, $e\mu$, ee	501389-501391
1000	350	1000	$\mu\mu$, $e\mu$, ee	501392-501394
1000	450	1000	$\mu\mu$, $e\mu$, ee	501395-501397
1500	250	1000	$\mu\mu$, $e\mu$, ee	501398-501400
1500	450	1000	$\mu\mu$, $e\mu$, ee	501401-501403
1500	600	1000	$\mu\mu$, $e\mu$, ee	501404-501406
1500	700	1000	$\mu\mu$, $e\mu$, ee	501407-501409

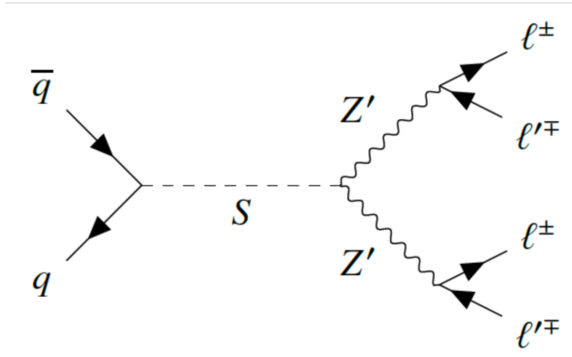

Figure 6.1: Pair-produced Z' model via heavy scalar S, in which the decay of the Z' is displaced from the primary vertex.

considers any child interactions which result in a status 1 (final state) charged particle, the electron distributions are, therefore, dominated by the electrons from brehmsstrahlung radiation. It is, however, important to include this information since these electrons can still be reconstructed as ID tracks and form part of signal DVs.

6.2.2 Background and Standard Model Samples

Only a few SM MC samples are used in the analysis. Because SM processes are generally produced at the interaction point and any potential low-mass backgrounds are suppressed by the dilepton mass cut in the signal region, backgrounds are estimated using data-driven methods. One dilepton filtered $t\bar{t}$ sample is, however, used for validation of the event mixing procedure and is further utilized as a K_S-rich sample in the LRT/VSI systematic error estimate in Section 7.3.5. The sample is generated using Powheg+Pythia 8.230 [81, 83] with the NNPDF2.3lo PDF set [82] and the `A14` min-bias tune and is a subset of the general $t\bar{t}$ production filtering on high p_T lepton activity in the events (with efficiency of ∼10.5%). The only additional SM samples used are for the identification and trigger scale factor studies detailed in Sections 7.3.3-7.3.4. These samples are not processed with LRT or VSI as detailed in Sections 5.1.2-5.1.4 and, instead, are derived into `DAOD_EGAM1` and `DAOD_MUON1` formats intended for isolating high p_T leptonic activity used for tag-and-probe studies. These samples are similarly generated using Powheg+Pythia 8.186 [83, 84], but with the `AZNLOCTEQ6L1` tune. The SM samples used in the analysis are summarized in Table 6.4.

6.3 `DRAW_RPVLL` Processing and Preselection

`DRAW_RPVLL` is a common dedicated stream used in a variety of BSM LLP searches to increase signal sensitivity. It is used for this particular search to filter the `physics_Main`

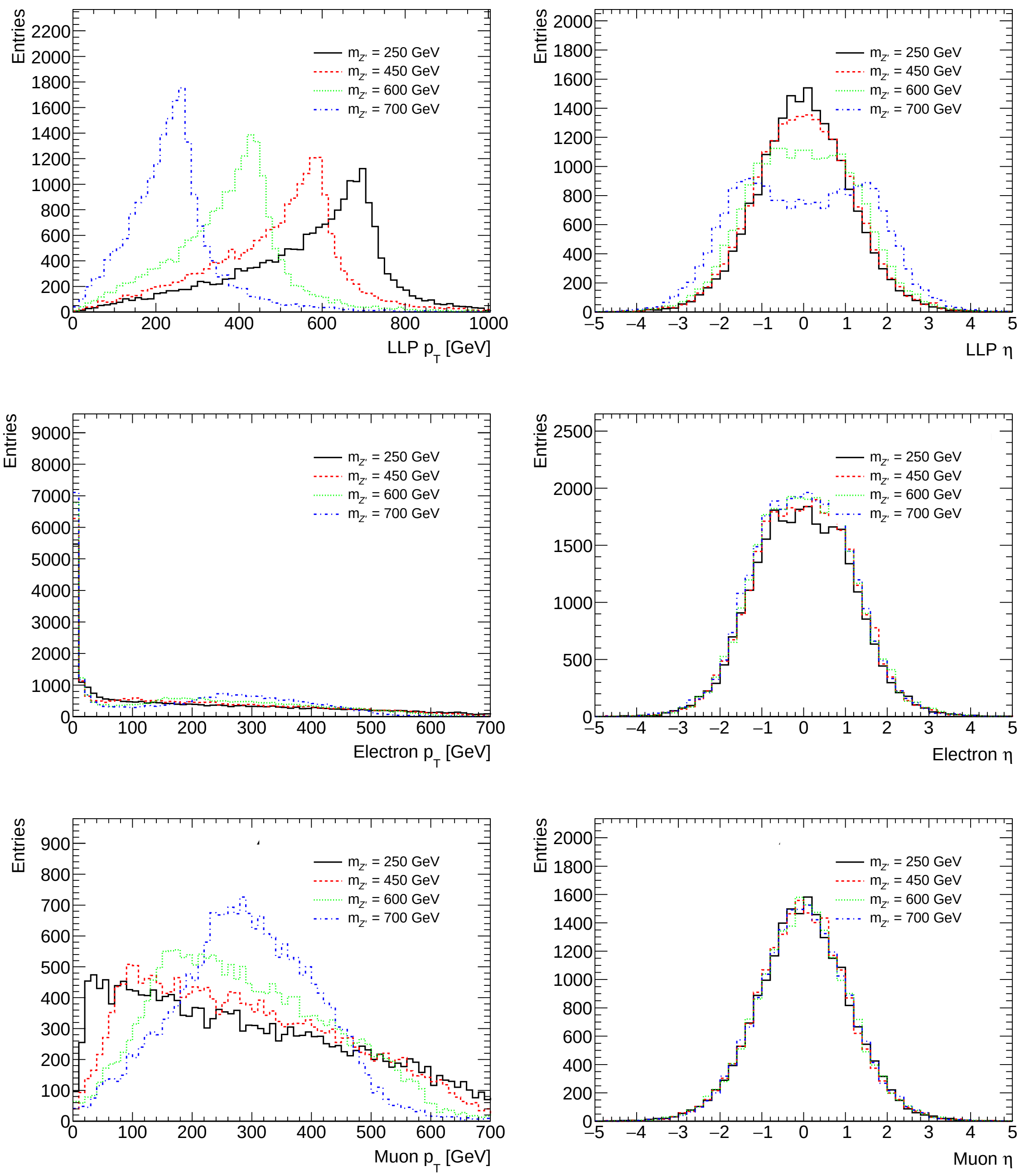

Figure 6.2: Truth-level p_T (left) and η (right) distributions for the signal LLP Z' (top), electrons (middle) and muons (bottom) for a set of Z' signal mc16d samples with a scalar mass of 1500 GeV and Z' decaying to $e\mu$ with a decay length ($c\tau$) of 100 mm and mass of 250, 450, 600, and 700 GeV.

Table 6.4: Standard Model MC samples & DSIDs used in tag-and-probe, tracking, and background studies. Events for the $Z \to \ell\ell$ samples are split by mc16a/mc16d/mc16e periods.

Process	DSID	Cross section (pb)	Events (10^6)	p-tag
$t\bar{t}$	410472	729.77	20	p4800
$Z \to ee$	361106	1901.1	309.71815/386.909/512.8052	p4615
$Z \to \mu\mu$	361107	1901.1	309.6468/388.311/495.3121	p4514

stream to about 10% of its original size via a combination of HLT and offline selections listed in Tables 6.5 and 6.6, respectively. The DRAW_RPVLL also utilizes the RAW data format to access low-level information (detector hits) required to reconstruct displaced tracks and vertices via the algorithms detailed in Sections 5.1.2 and 5.1.4. These algorithms are far too computationally expensive to be run on the full Run II dataset, necessitating the use of offline trigger and filter preselections as detailed in Sections 6.3.1 and 6.3.2, respectively. Including the newly reconstructed objects and dedicated containers for displaced vertices, the standard xAOD data format is designated as DAOD_RPVLL, denoting that the sample has been processed by the LRT and VSI algorithms, among others.

The final processing step derives the DAOD_RPVLL datasets into the DAOD_SUSY15 format, where a second processing of VSI is performed using the unused standard and displaced tracks. The derivation additionally custom processes the data with the intention of file size reduction following the recommendations of the Analysis Model Study Group (AMSG) [85]. A portion of the object information found in the DAOD_RPVLL data is lost in the filtering, but the variables necessary for the analysis are available for derivations with p-tags newer than p4732. While the MC largely follows the details of the above processing, the samples are not filtered using the RPVLL lepton-based selections. However, the trigger and filter matching requirements in the event selection of Section 7.1 guarantee that signal events still pass these requirements.

6.3.1 Trigger

Standard electron and muon HLTs use standard tracking information, making them particularly insensitive to displaced leptons. As a result, the first step of the DRAW_RPVLL filtering requires that the events pass one of the triggers listed in Table 6.5 where the analysis makes use of photon triggers which depend on the electromagnetic showers found in the calorimeters and muon triggers which depend on MS track information to target signal electrons and muons, respectively. This allows for high-d_0 signal electrons and muons to trigger the appropriate HLTs without necessarily having reconstructed ID tracks (electrons without ID tracks are essentially photons). The triggered events can, then, recover the signal lepton ID

Table 6.5: L1 seeds and HLTs used to select events in DRAW_RPVLL filter. When two L1 items or two HLT triggers are given, the former was used in 2015 and 2016 while the latter was used in 2017 and 2018. The single muon HLT trigger uses MS information only. In case where the p_T requirement is higher than that in the trigger, the threshold used in the DRAW_RPVLL filters in Table 6.6 is used for consistency and to simplify the calculation of scale factors.

Description	L1 Trigger	HLT Trigger	Requirement
Single Photon	L1_EM22VHI (L1_EM24VHI)	HLT_g140_loose	One object with $p_T > 160$ GeV
Diphoton	L1_2EM15VH (L1_2EM20VH)	HLT_2g50_loose (HLT_2g50_loose_L12EM20VH)	Two objects with $p_T > 60$ GeV
Single Muon	L1_MU20 (L1_MU21)	HLT_mu60_0eta105_msonly	One object with $p_T > 60$ GeV and $0 < \|\eta\| < 1.05$

tracks when the LRT algorithm is run.

One should note that the trigger menu was updated mid-Run II (2017), giving the listed diphoton trigger a prescale, but an analogous one with a slightly higher threshold L1 seed, HLT_2g50_loose_L12EM20VH, was used instead as it was the unprescaled for 2017-2018. Because the L1 thresholds (L1_2EM15VH or L1_2EM20VH) are significantly below those of the appropriate HLT thresholds, the change is expected to have minimal impact on the analysis.

6.3.2 Filter

For each of the triggers of Table 6.5 and targeted signal regions of ee, $e\mu$, and $\mu\mu$, there is a corresponding filter of offline selections which are detailed in Table 6.6. In each case, the filter p_T requirements are at or above the thresholds of the respective HLT to ensure that the object is in the trigger plateau where the trigger is most efficient.

Similar to the trigger selections, the filters which select electrons also accept photons because pre-LRT and high-d_0 electrons can often be misidentified as photons. To compensate, two steps were taken to limit the data-rate as well as select the di-electron vertices of interest. First, no identification requirements were placed on any of the filter objects except those labeled "loose". Second, the single photon filter is required to have a second associated object passing the given kinematic cuts.

One feature specific to the muon filter is the cut on the transverse impact parameter, d_0. Because the analysis is concerned with displaced vertices reconstructed using ID tracks, the signal muons must have an associated ID track. However, as was described in Section 6.3.1, the triggers selecting signal muons depend on MS track information. As such, the signal muons are required to be a combination of their ID and MS tracks, as described in

Table 6.6: Offline filters used to select muon, photon, and electron candidates. *The $|d_0|$ requirement is imposed only on `Combined` muons.

Filter	Object 1	p_T [GeV]	$\|\eta\|$	$\|d_0\|$ [mm]	Object 2	p_T [GeV]	$\|\eta\|$	$\|d_0\|$ [mm]
μ	μ	> 60	< 1.07	$> 2.0^*$				
γ	γ (loose)	> 160	< 2.5	–	γ (loose)	> 10	< 2.5	–
					e	> 10	< 2.5	> 2.0
					μ	> 10	< 2.5	$> 2.0^*$
e	e	> 160	< 2.5	> 2.0				
$\gamma\gamma$	γ (loose)	> 60	< 2.5	–	γ (loose)	> 60	< 2.5	–
ee	e	> 60	< 2.5	> 2.0	e	> 60	< 2.5	> 2.0
$e\gamma$	e (loose)	> 60	< 2.5	–	γ (loose)	> 60	< 2.5	–
$e\gamma$	e	> 60	< 2.5	> 2.0	γ (loose)	> 60	< 2.5	–

Section 5.3. However, detailed studies reveal that signal muons can often have their MS track combined with a random track of low p_T and small $|d_0|$. Fortunately, these tracks are not related with one another and, hence, the combined tracks tend to have a poor χ^2 fit, providing a powerful discriminant with no significant loss of efficiency. Thus, the above d_0 cut is only applied to combined muons with a fit quality of $\chi^2/n_{dof} < 5$ and, if this quality constraint is satisfied, the kinematic cuts are applied to the combined track. Otherwise, the kinematic cuts are applied to the MS track, which is not relevant to this analysis.

Chapter 7
Search for Dilepton Displaced Vertices

The main components of the analysis are discussed in the following sections, namely, the selections that define the signal DVs, the data-driven background estimations, and the systematic uncertainties on the signal efficiencies. Results for the full Run II dataset are presented in Section 7.4.

7.1 Event Selection

Before identifying and selecting the primary analysis object, dilepton DVs, events undergo basic selections to ensure data quality and remove potential background contributions. These selections include requirements on the following:

- `GoodRunsList`: GRLs from Section 6.1 remove events from incomplete lumi blocks.
- Cleaning: events flagged with problems in the LAr calorimeters, TileCal, and SCTs or incomplete events from detector downtime or data corruption are removed.
- PV: at least one PV is required to exist on the beam line ($|z_{PV}| < 200$ mm) with at least two associated tracks.
- Trigger: after passing the `DRAW_RPVLL` filtering, events are required to pass one of the HLTs in Table 6.5 as other HLTs not included in the table are also used in the filtering for different studies.
- Cosmic veto: events with dimuon verticess having $\Delta R_{\cos} = \sqrt{(|\Delta\phi| - \pi)^2 + (\Sigma\eta)^2} < 0.01$ are removed to eliminate background contributions.

The cosmic veto will be motivated in detail in Section 7.2.1, but, in principle, a cosmic-ray muon can be reconstructed as a back-to-back and oppositely-charged pair of muons if it passes through the ID, and therefore can also be reconstructed as signal DV. However, the back-to-back nature of the muons can be exploited by imposing a $\Delta R_{\cos} < 0.01$ cut to any signal muon pairs forming a DV found in the event, where $\Sigma\eta = \eta_1 + \eta_2$ and $\Delta\phi = \phi_1 - \phi_2$. In this analysis, $\Sigma\eta$ is used because cosmic ray muons passing through the detector will be reconstructed back-to-back where the η of the muons would be equal and opposite in sign. An alternative variable, such as $\Delta|\eta| = |\eta_1| - |\eta_2|$, would also remove back-to-back cosmic rays, but would also reject highly collimated signal events. The cosmic veto eliminates $\lesssim 1\%$ of signal events. Both the event-level and vertex-level requirements are summarized in Table 7.3.

7.1.1 Vertex Selection

The vertex selection is applied to vertices reconstructed with the secondary vertexing algorithm detailed in Section 5.1.4. Signal vertices are required to have a pair of signal leptons, either two electrons, two muons, or an electron-muon pair. Signal leptons are defined in Section 7.1.2 with different requirements depending on the lepton type. Other tracks, including non-leptonic tracks, are permitted in signal vertices. Vertices with exactly one signal lepton and a non-leptonic track are used for the validation region. Finally, a control region is defined using vertices with exactly two non-leptonic tracks. The validation and control regions are used in the background and systematic uncertainty estimates.

In all regions, vertices are also required to be in the fiducial region satisfying $r < 300$ mm and $|z| < 300$ mm. Vertices are also required to be sufficiently displaced from any PV, with a transverse displacement (R_{xy}) of at least 2 mm to suppress prompt decay backgrounds and, additionally must satisfy $\chi^2/n_{dof} < 5$ to reject poorly reconstructed vertices, following the standard recommendation from the Tracking Combined Performance (CP) group. A map of the detector material [86–89] in the analysis fiducial volume is used to veto photon conversions resulting in ee, $e\mu$, and ex (where x represents any non-leptonic ID track) vertices. While it is possible that particle interactions with material could produce $\mu\mu$ vertices, the rate for producing a $\mu\mu$ final state by photon conversion is significantly smaller than for electron channels. Thus, the material map veto is neither needed nor applied for muon vertices. It has also been previously shown that the background from the Drell-Yan process would be negligible since the high DV mass cut is well above Upsilon resonances [79]. Similarly, any vertex which is reconstructed inside a disabled Pixel module [90] for a given run is rejected using disabled module maps. These maps were applied to both data and MC for consistency.

7.1.2 Lepton Selection

After basic quality requirements have been imposed on the DVs, additional selections are applied to the constituent leptons as well as to the lepton pairs surviving those cuts.

Table 7.1: Signal electron definitions.

$p_T > 10$ GeV
$\lvert\eta_{clus}\rvert < 2.47$
Bad cluster removal
No crack veto
Modified `VeryLooseLLH` identification working point
Pass overlap removal

Electron Selection

Electron selections are based on the extensively studied standard recommendations from the Electron-Gamma (EGamma) CP group with specific modifications to account for the highly displaced signal leptons in LLP scenarios. In particular, no isolation criteria are placed on signal electrons due to the high boost of the LLPs that can significantly collimate the decay electrons and no ID track quality criteria are imposed due to the highly displaced nature of the electron tracks[3]. As noted in Section 5.2, the standard `VeryLooseLLH` identification working point is modified to remove cuts on d_0 and the number of Pixel hits to improve sensitivity to signal leptons. The standard kinematic requirements, $|\eta_{clus}| < 2.47$ and $p_T > 10$ GeV, are imposed without the crack region veto and signal electrons are rejected if they are associated with a bad, or low quality, EMC cluster. Signal electrons must, finally, pass an overlap removal process intended to ensure that each ID track is only associated with a single physics object. Generally, ambiguity is resolved between jets, electrons, and muons based on their energy and calorimeter signatures and precedence is given to higher p_T objects when two of the same type share an ID track. Table 7.1 summarizes the signal electron definitions. The impact of these changes is shown in Figure 7.1 where the gain in sensitivity for a set of Z' signal mc16e samples is evident both for the use of LRT in addition to ST and for the modification of the standard identification working point.

Muon Selection

Muon selections are similarly based on standard recommendations from the Muon CP group with modifications implemented to improve sensitivity to signal muons. No isolation criteria are imposed due to the highly collimated muons and no ID track quality are imposed due to the highly displaced nature of the muon tracks[3]. The standard kinematic requirements, $p_T > 10$ GeV and $|\eta| < 2.5$, and same overlap removal procedure are applied to signal muons. As detailed in Section 5.3, signal muons are required to be `Combined` muons and the standard `Loose` muon identification working point has the Pixel hit requirement removed.

[3]The standard track quality criteria recommendation from the Tracking CP group is $|d_0 \text{ significance}| < 5$ and $|\Delta z_0 \sin(\theta)| < 0.5$ mm.

Table 7.2: Signal muon definitions.

$p_T > 10$ GeV
$|\eta| < 2.5$
Modified `Loose` identification working point
`Combined`
Pass overlap removal

Table 7.2 summarizes the signal muon definitions. The impact of these changes is shown in Figure 7.1 where the gain in sensitivity for a set of Z' signal mc16e samples is evident both for the use of LRT in addition to ST and for the modification of the standard identification working point.

Dilepton Displaced Vertex Selection

There are a few small additional requirements imposed on signal lepton pairs to identify the signal dilepton DVs. The dilepton pair are required to match the HLT object(s) from a trigger in Table 6.5 and the leptons must additionally match the appropriate filters in Table 6.6. The dilepton pair must be oppositely charged and have an invariant mass of at least 12 GeV to suppress low-mass SM particles. This dilepton DV mass cut is in contrast to the standard DV reconstruction mass, which is calculated assuming that all tracks are pions and suppresses SM contributions from lower mass particles such as J/Ψ, Υ, or B hadrons. Table 7.3 summarizes all event and vertex level cuts.

7.1.3 Signal Acceptance and Efficiency

Acceptance, efficiency, and signal efficiency distributions are presented here. Generally the selections impacting the signal yield most significantly are the requirements that a DV be reconstructed, the material veto in electron channels, and object type, trigger and filter matching. For all signal efficiencies shown, the total systematic uncertainties of Section 7.3.6 are included while for cutflows, only the raw number of vertices are used in calculating the signal yields. The signal efficiency is defined as the ratio of reconstructed signal DVs passing the full selection criteria to truth signal DVs generated. Acceptance is defined as the ratio of truth signal DVs passing truth-level selection criteria to truth signal DVs. Finally, the efficiency is the ratio of reconstructed signal DVs passing the full selection criteria to the number of truth signal DVs in the acceptance:

$$\text{Signal Efficiency} = \text{Acceptance} \times \text{Efficiency}. \tag{7.1}$$

Note, this equation also applies at the event level, where signal efficiency is the ratio

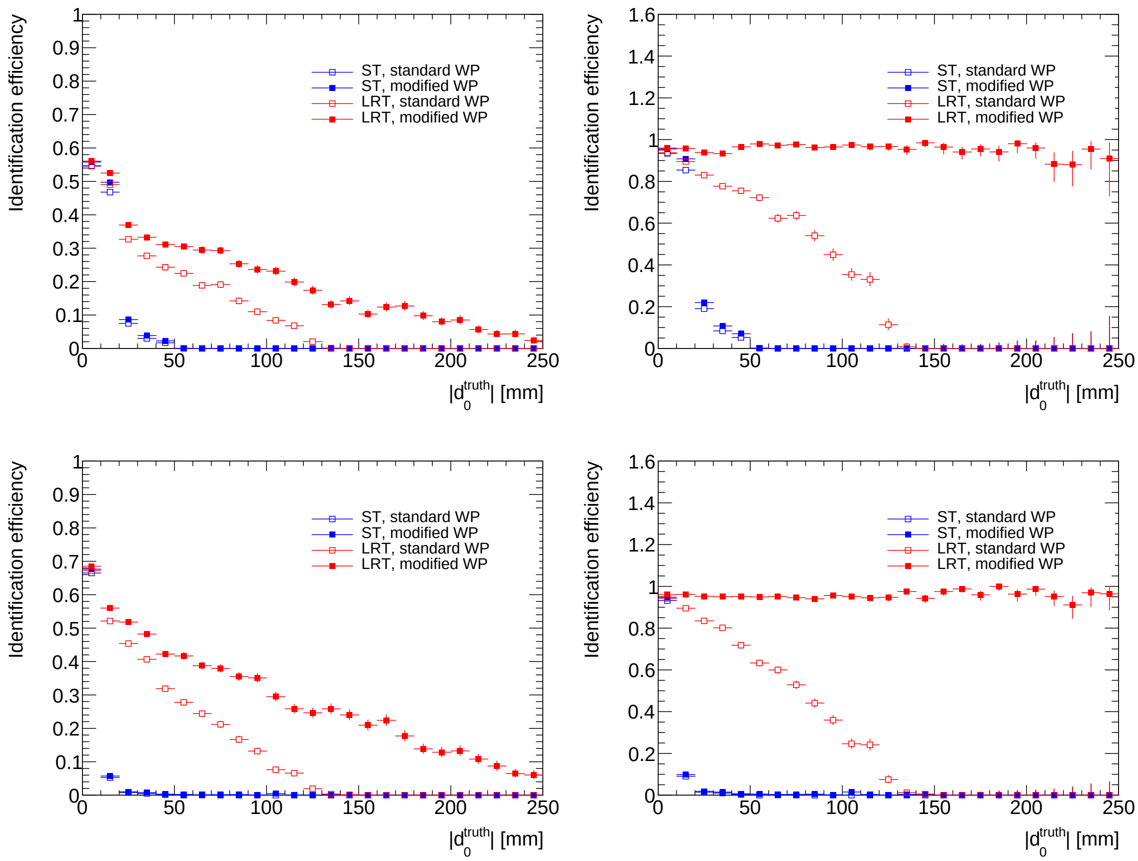

Figure 7.1: Identification efficiencies for electrons (top) and muons (bottom) reconstructed as ST and LRT for standard and modified working points. A combined set of Z' signal mc16e samples with a scalar mass of 1500 GeV, Z' mass of 450 GeV and all decay lengths ($c\tau$) was used. The left plots represent the efficiency for a truth signal lepton to pass the identification working points while the right plots represent the efficiency for a truth signal lepton reconstructed as the appropriate lepton type to pass the same identification working points. The left identification efficiencies are therefore with respect to the truth signal leptons while the right are with respect to the correctly reconstructed leptons.

of events with at least one reconstructed signal DV passing full selection criteria to truth events with at least one signal DV generated. While event-level signal efficiencies can be used for certain reinterpretations, vertex-level signal efficiencies are more reinterpretable and presented in the following. In the following, cutflows and signal efficiency distributions and maps are presented for a representative set of Z' mc16a samples with a scalar mass of 1000 GeV and all Z' decay modes, where the Z' mass and decay length ($c\tau$) are varied depending on the distribution.

Table 7.3: Signal event and vertex level cuts.

Event Selections
GoodRunsList
Event cleaning
$\|z_{PV}\| < 200$ mm
Trigger filter
Cosmic veto
Vertex Selections
$r < 300$ mm, $\|z\| < 300$ mm
$R_{xy} > 2$ mm
$\chi^2/n_{dof} < 5$
Material map veto (for electron channels)
Disabled module veto
Two signal leptons (see Tables 7.1– 7.2)
Trigger matching
Filter matching
Opposite charge
$m_{\ell\ell} > 12$ GeV

Cutflows

Figure 7.2 presents an example of the truth-matched vertex level cutflows for a Z' with a mass of 350 GeV and decay lengths ($c\tau$) of 10, 100, and 1000 mm. As noted previously, the primary loss is in the vertex reconstruction for all decay lengths ($c\tau$) with additional losses for electron channels due to the 40% fiducial volume coverage of the material map veto. This is, however, less impactful for the 10 mm decay length ($c\tau$) due to the relatively low decay radius of the signal Z', where the material map veto does not reject many DVs. All lifetimes experience a similar loss in efficiency due to the high p_T requirements of the trigger and filter matching. For large lifetimes, this effect can become more severe as the electron children can deposit their energy outside the EMC and muon children may not leave enough hits in the muon chambers.

Lepton Efficiencies

The signal efficiency from Equation 7.1 can also be broken down into several individual component efficiencies in order to understand where some of the losses in the cutflows from Figure 7.2 originate from. Efficiencies associated with the track reconstruction, lepton reconstruction, and lepton identification for each lepton type are studied in the following. The tracking efficiency is defined as the fraction of truth signal leptons that are matched to a reconstructed ID track satisfying the looser tracking criteria for vertexing in Section 5.1.4.

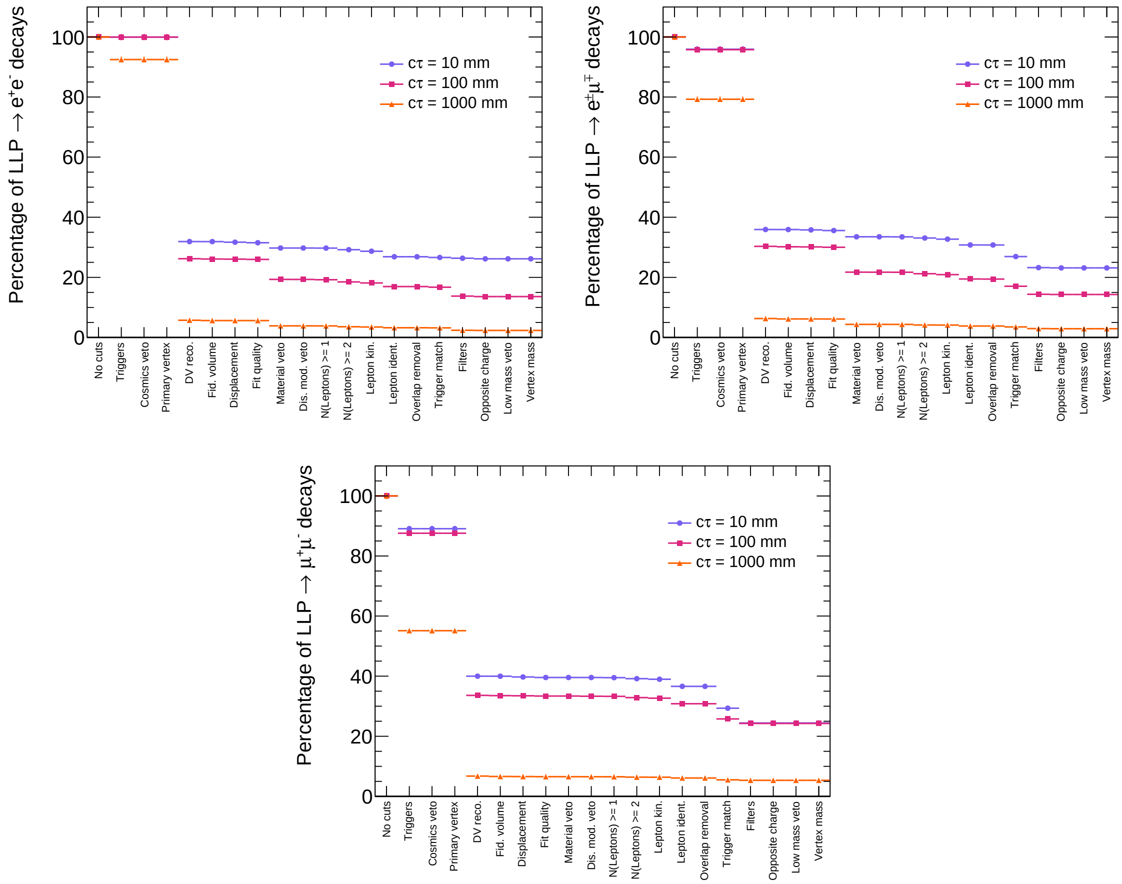

Figure 7.2: Percentage of Z' decays passing each cut in the signal cutflow for the ee (top left), $e\mu$ (top right), and $\mu\mu$ (bottom) decay modes for a set of Z' signal mc16a samples with a scalar mass of 1000 GeV and Z' mass of 350 GeV and decay lengths ($c\tau$) of 10, 100, and 1000 mm.

The lepton reconstruction efficiency is the fraction of truth matched tracks that belong to a reconstructed lepton of the correct type and the identification efficiency is the fraction of reconstructed leptons satisfying signal quality and identification criteria from Section 7.1.2. By separating the effects of each step in identifying signal leptons, it is possible to isolate the dependence on impact parameters to the specific effects and understand the primary sources for efficiency loss. Figure 7.3 shows these efficiencies for the same samples used in Figure 7.1 as a function of d_0 and the number of Pixel hits, once that information is available from a truth matched track. Loose truth kinematic cuts are applied on the signal lepton, $p_T > 0.4$ GeV and $\eta < 2.5$, but otherwise no other kinematic cuts are applied to the truth or reconstructed leptons.

Tracking efficiency depends strongly on impact parameters, decreasing from $\sim 60-80\%$

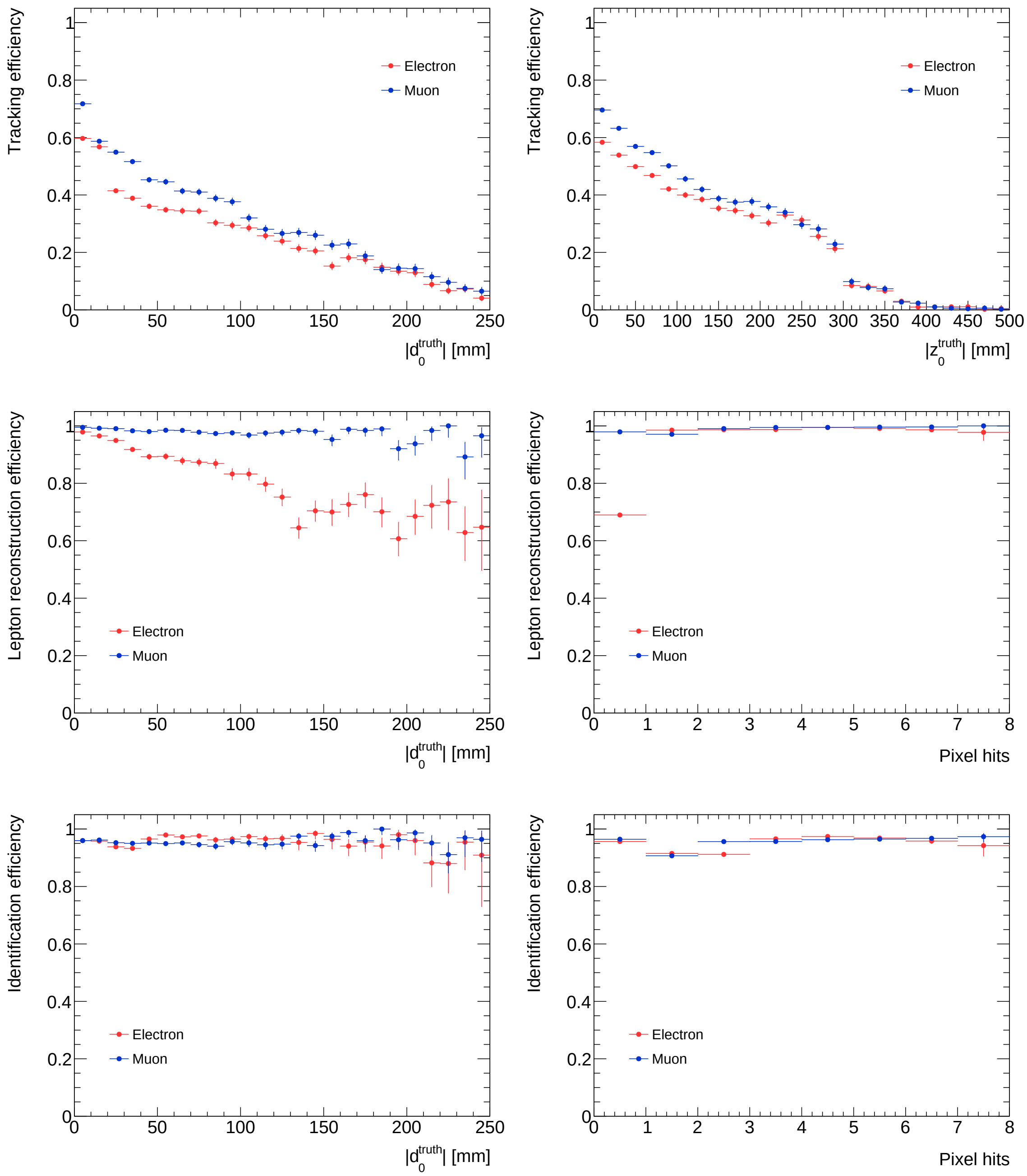

Figure 7.3: Lepton efficiencies for a set of Z' signal mc16e samples with a scalar mass of 1500 GeV, Z' mass of 450 GeV and all decay lengths ($c\tau$): tracking efficiency (top), lepton reconstruction efficiency (middle) for reconstructed tracks, and identification efficiency (bottom) for reconstructed leptons (see text) as function of the truth signal leptons' d_0 (left) and number of Pixel hits for truth matched tracks (right). This information is not available for truth signal leptons that are not reconstructed and, so, tracking efficiency is given as a function of z_0 instead.

to ∼5% at large d_0. The largest decrease is in the lowest d_0 bin(s) where LRT begins to take over from ST, indicating that the LRT/VSI systematic is the dominant one when considering any trends in impact parameters. While there are slight differences in the tracking efficiencies between electrons and muons, the most prominent difference can be seen in the lepton reconstruction efficiency. In the larger d_0 region, electron reconstruction begins to degrade due to the increase in reconstructed tracks with no Pixel hits, as shown in Figure 7.3. This difference is attributed to the ambiguity between electrons and photons where, specifically, a photon is reconstructed if the object has no track, a track with fewer than 4 Silicon hits (7 for LRTs), or has no Pixel hits and is associated with a conversion vertex. This effect is not evident for the muon reconstruction due to the addition of the MS tracking information for `Combined` muon tracks. The tracking efficiency is the most significant loss in efficiency for both lepton types and naturally depends on the LLP boost and, thus, decay position which impacts the tracking information available for the decay particles. The systematic associated with the tracking is estimated in Section 7.3.5.

Vertex Efficiencies

The DV reconstruction stage of the cutflows in Figure 7.2 is the most significant loss in efficiency and can be similarly studied in more detail by separating the DV reconstruction efficiency into component tracking and vertexing efficiencies. Tracking efficiency can be defined as the efficiency with which at least two charged truth children of a signal LLP are reconstructed as ID tracks. Vertexing efficiency, then, is the efficiency of those reconstructed tracks also forming a DV and being associated with the correct physics objects and passing basic quality criteria. Finally, reconstruction efficiency is simply the product of the tracking and vertexing efficiencies. An example of these efficiencies is given in Figure 7.4 for a representative set of Z' signal mc16e samples with a scalar mass of 500 GeV, Z' mass of 100 GeV and all decay lengths ($c\tau$). Muon channels are slightly more efficient. The efficiencies decrease slightly with increasing pileup with a more notable trend in the vertexing efficiency, as is expected. The dip in the vertexing efficiency (and, thus, reconstruction efficiency) at very low radii is due to the $|d_0| > 2$ mm cut applied as in Table 5.3. At larger radii, outside the Pixel layers, $\mathrm{R}_{\mathrm{xy}}^{\mathrm{truth}} \gtrsim 120$ mm, the vertexing efficiency increases slightly. It should be noted that Pixel hits are not required for tracks used in secondary vertexing, per the track selections listed in Table 5.3.

Signal Efficiencies

For the samples used in Figure 7.2, acceptance, efficiency and signal efficiency distributions can be extracted as a function of several basic kinematics. Figure 7.5 presents the total signal efficiency as a function of R_{xy}, p_T, η, ϕ, z, and pileup (μ) for the all decay modes at

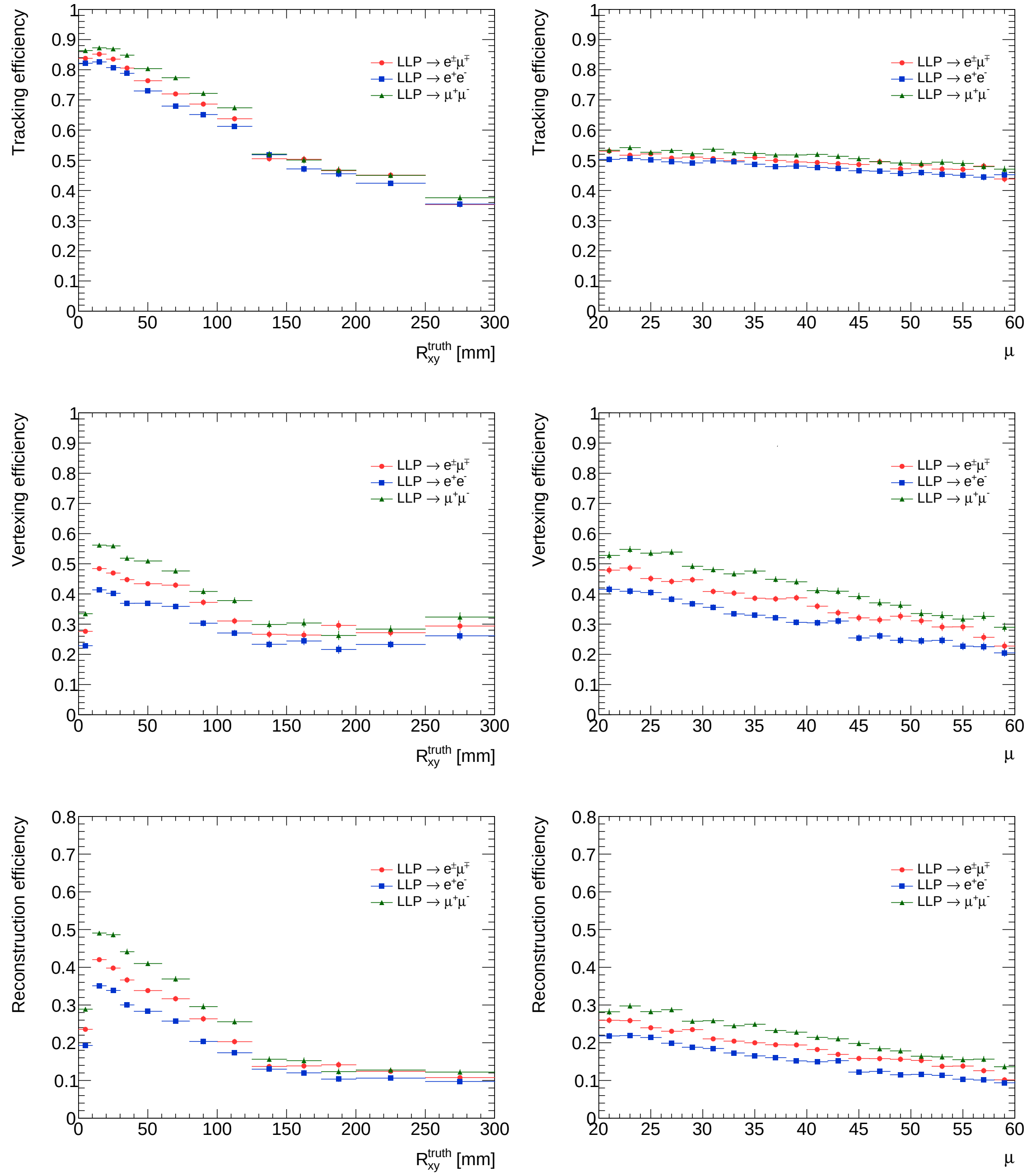

Figure 7.4: Tracking efficiencies (top), vertexing efficiencies (middle) and total reconstruction efficiencies (bottom) for a set of Z' signal mc16d samples with a scalar mass of 500 GeV, Z' mass of 100 GeV and all decay lengths ($c\tau$). Efficiencies are given as a function of the truth DV radius (left) and average pileup (right).

the decay length ($c\tau$) of 100 mm. For all decay modes, there is a notable decrease in signal efficiency for increasing R_{xy}, $|\eta|$, $|z|$, and μ. The decrease in the efficiency at large radii is due to the loss of Pixel hits necessary for track reconstruction, leading to a low vertex reconstruction efficiency in this regime. The ϕ distribution is flat and efficiency decreases modestly for increasing pileup, both of which is expected. For this particular set of signal mc16a samples, the signal efficiency is 14-25%.

As noted in Section 7.1.3, the signal efficiencies can be separated into acceptance and efficiency, where the truth and reconstruction level information can be studied separately. Analogous to the distributions in Figure 7.5, the acceptances, efficiencies, and total signal efficiencies are shown in Figure 7.6 for the decay length ($c\tau$) of 100 mm as a function of R_{xy} and p_T of the truth Z'. It is evident that there is a loss of acceptance for low p_T and loss of efficiency for increasing R_{xy}. This is expected since low momentum LLPs (for a given LLP mass) are less likely to generate high p_T signal leptons that can pass the triggers and filters before the reconstruction stage. Similarly, reconstruction efficiency decreases with decay length as there is insufficient hits for the track/vertex reconstruction.

Efficiency Maps

Efficiency maps needed for reinterpretation for other BSM searches are also extracted as a function of η vs. R_{xy} and η vs. p_T. Having these maps for several Z' masses and lifetimes makes the results of this analysis more reinterpretable and Figure 7.7 presents a representative set of these maps for a Z' with decay length ($c\tau$) of 100 mm. In the innermost regions, the signal efficiency is 20-30% but decreases significantly for increasing η and efficiencies can fluctuate in regions of large p_T where statistics are limited.

Lifetime Extrapolations

Finally, the acceptances and signal efficiencies can be extrapolated over different decay lengths ($c\tau$) using a collection of Z' mc16a signal samples generated at several decay lengths. First, consider the probability density function for the observed lifetime of a Z' generated with lifetime τ_{gen}:

$$P_{\text{decay}}(t, \tau_{\text{gen}}) = \frac{1}{\tau_{\text{gen}}} e^{-t/\tau_{\text{gen}}}. \tag{7.2}$$

Then, because the individual events themselves do not depend on the generated lifetime, τ_{gen}, the probability of observing events with a different generated lifetime, τ_{target}, can be emulated by applying a weight to each of the individual events:

$$w(t) = \frac{P(t, \tau_{\text{target}})}{P(t, \tau_{\text{gen}})} = \frac{\tau_{\text{gen}}}{\tau_{\text{target}}} \exp -[(\frac{1}{\tau_{\text{target}}} - \frac{1}{\tau_{\text{gen}}})t], \tag{7.3}$$

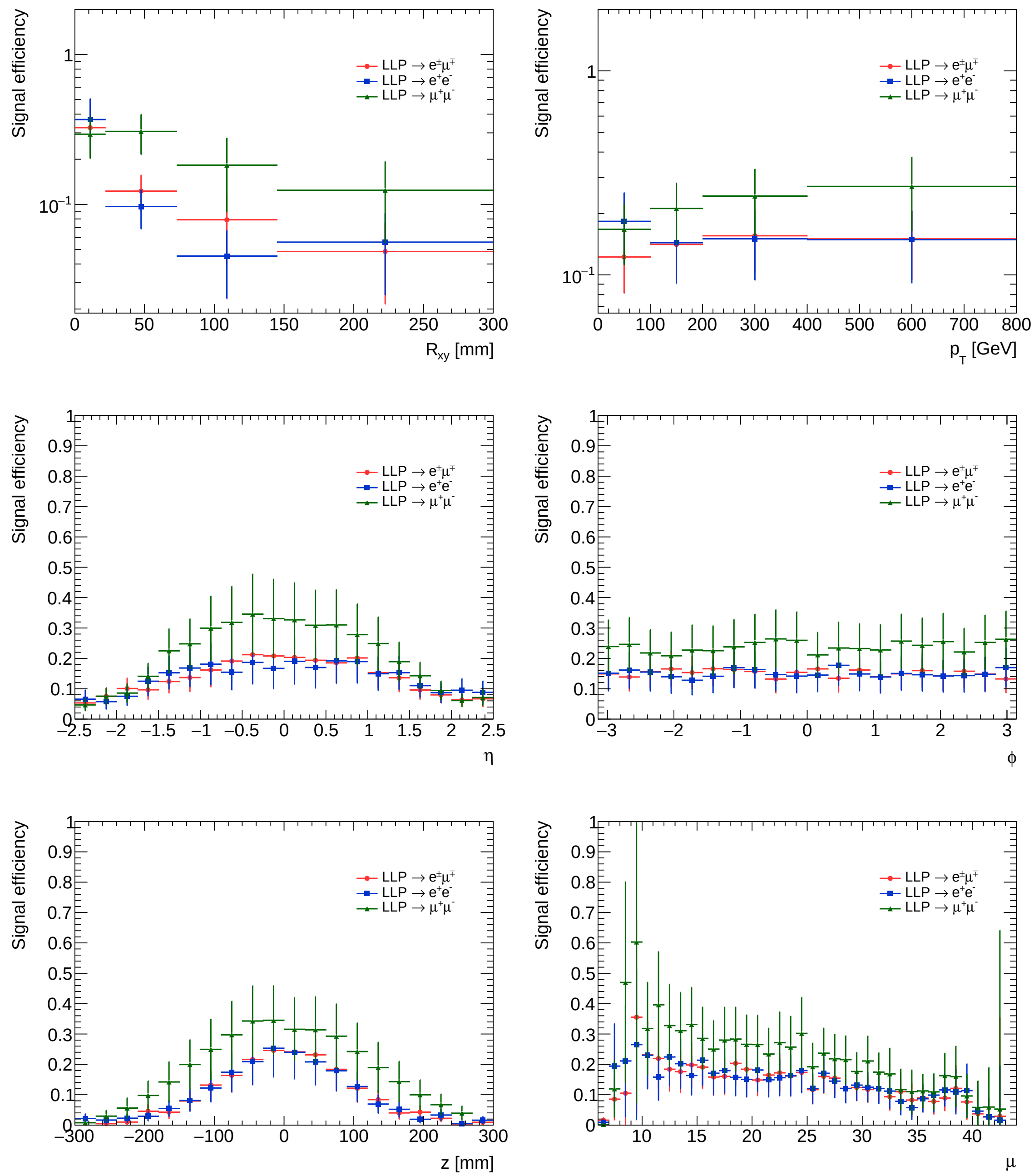

Figure 7.5: Vertex-level signal efficiency as a function of truth R_{xy} (top left), p_T (top right), η (middle left), ϕ (middle right), z (bottom left), and μ (bottom right) of the Z' in the signal mc16a samples with a scalar mass of 1000 GeV and Z' mass of 350 GeV and decay length ($c\tau$) of 100 mm.

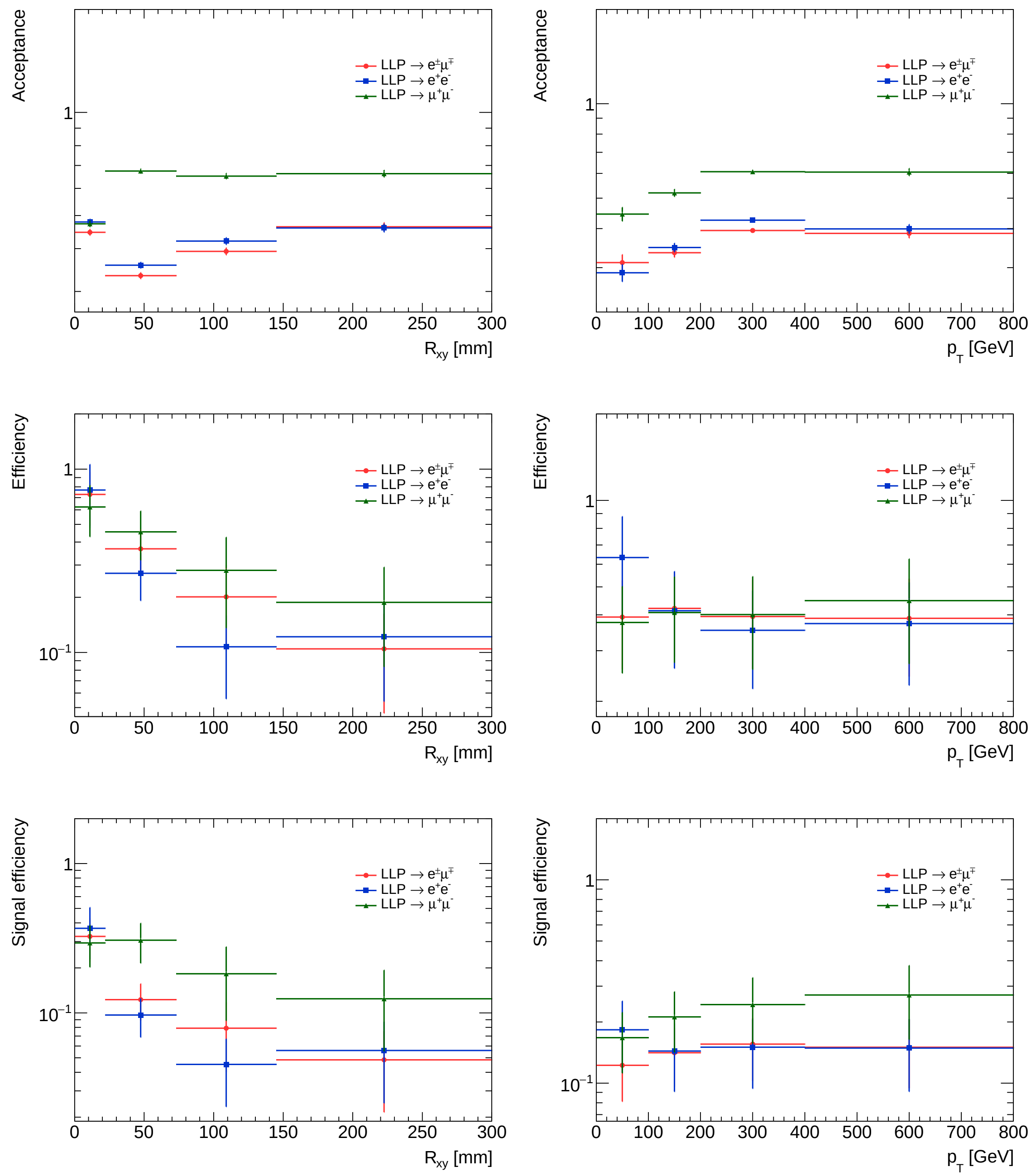

Figure 7.6: Vertex-level acceptance (top), efficiency (middle) and signal efficiency (bottom) as a function of truth R_{xy} (left) and p_T (right) for the three Z' decay modes in Z' signal mc16a samples with a scalar mass of 1000 GeV and Z' mass of 350 GeV, and decay length ($c\tau$) of 100 mm.

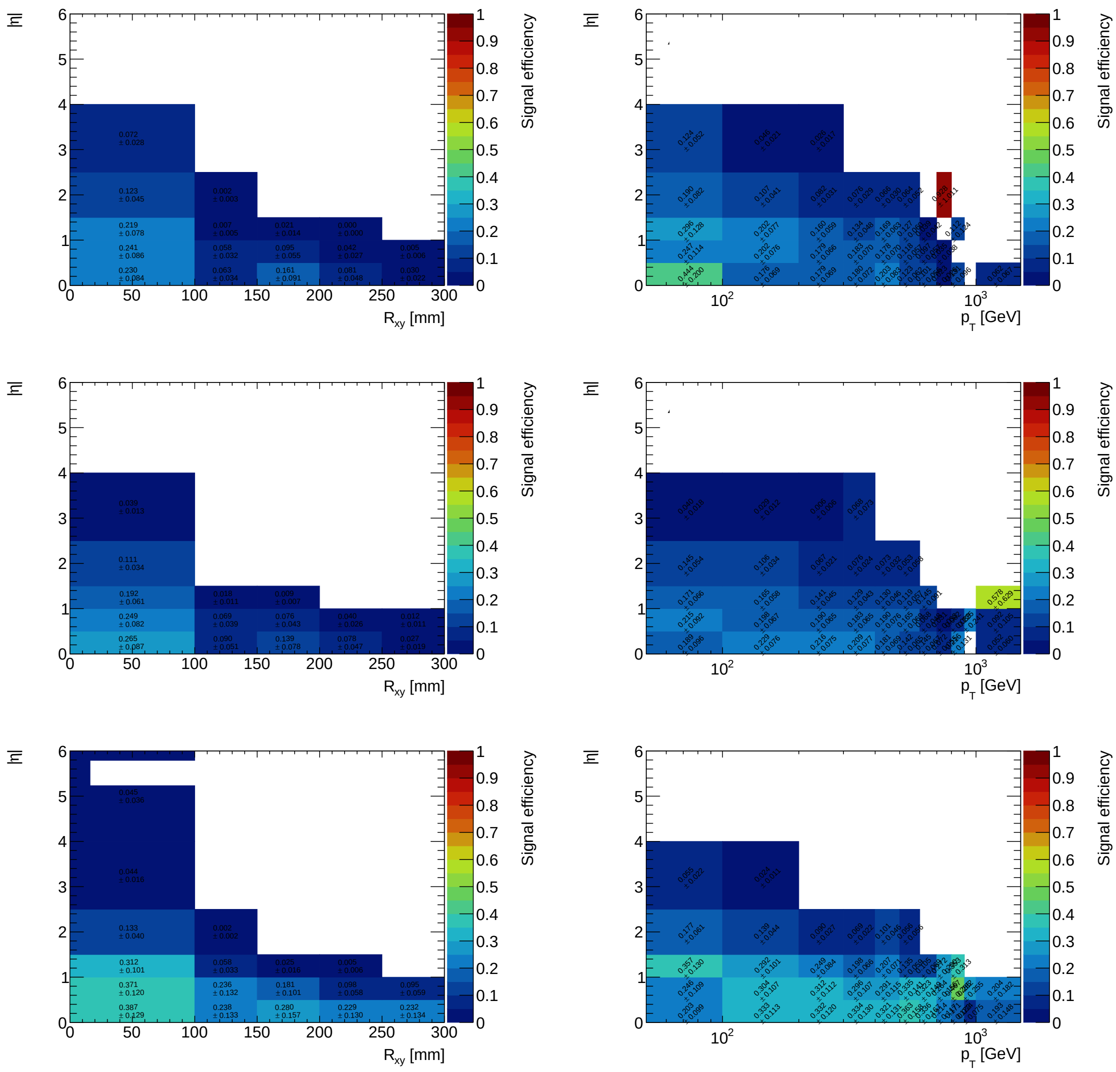

Figure 7.7: Vertex-level signal efficiency maps binned in η vs. R_{xy} (left) and η vs. p_T (right) for the ee (top), $e\mu$ (middle), and $\mu\mu$ (bottom) decay mode using a set of Z' signal mc16a samples with a scalar mass of 1000 GeV, Z' mass of 350 GeV and Z' decay length ($c\tau$) of 100 mm.

for observed lifetime t. Finally, the number of events is then estimated by independently extrapolating each of the five generated lifetimes and taking the weighted mean at each lifetime with:

$$N_{eff}(t) = \frac{[\sum w(t)]^2}{\sum w(t)^2} \tag{7.4}$$

as the weight, representing the effective number of events generated. Similarly, the associated error is also the weighted mean of the errors from the extrapolations.

Figure 7.8 presents the acceptances and selection efficiencies for four different scalar/Z' mass points at different decay lengths ($c\tau$) from 1 to 10000 mm. For the same scalar mass, the more massive Z' have better acceptance and efficiency due to its comparatively low boost and decay radius. The more massive scalar mass points also have generally higher efficiencies due to the high p_T lepton children decay products being able to pass the high p_T threshold of the signal triggers and filters. The colored bands in Figure 7.8 represent the statistical and total uncertainties, respectively, where an example of the relative total uncertainties is given in Figure 7.29.

A closure test of the extrapolation procedure can also be performed, comparing each generated signal efficiency point to the extrapolated curve. Figure 7.9 presents an example of this closure test for a set of mass points and decay modes where, again, the colored bands represent the total uncertainty. Despite the good agreement shown in the closure test, a conservative systematic uncertainty of 2% is assigned to the procedure. This systematic uncertainty is obtained as a conservative estimate by removing a generated signal efficiency from the extrapolation and comparing the extrapolated value to the generated one.

A summary of the signal efficiencies for the combined, luminosity weighted MC samples for the entire Z' signal grid is presented in Table 7.4.

7.2 Background Estimation

This analysis has very low background due to the chosen selections in Section 7.1. In particular, the $R_{xy} > 2$ mm and $m_{\ell\ell} > 12$ GeV cuts strongly suppress the SM background contributions from low-mass processes and material interactions. Studies from the early Run II analysis revealed that no significant contributions from photon conversions or other material interactions exist beyond a DV mass of 8 GeV even without the $p_T > 10$ GeV track momentum requirement or material veto applied and no significant SM contributions from hadronic decays exist in the region $6 < m_{\ell\ell} < 12$ GeV [91]. The only remaining background contributions, then, are from cosmic ray muons and the random crossing of two uncorrelated tracks. Both backgrounds are estimated using data-driven techniques.

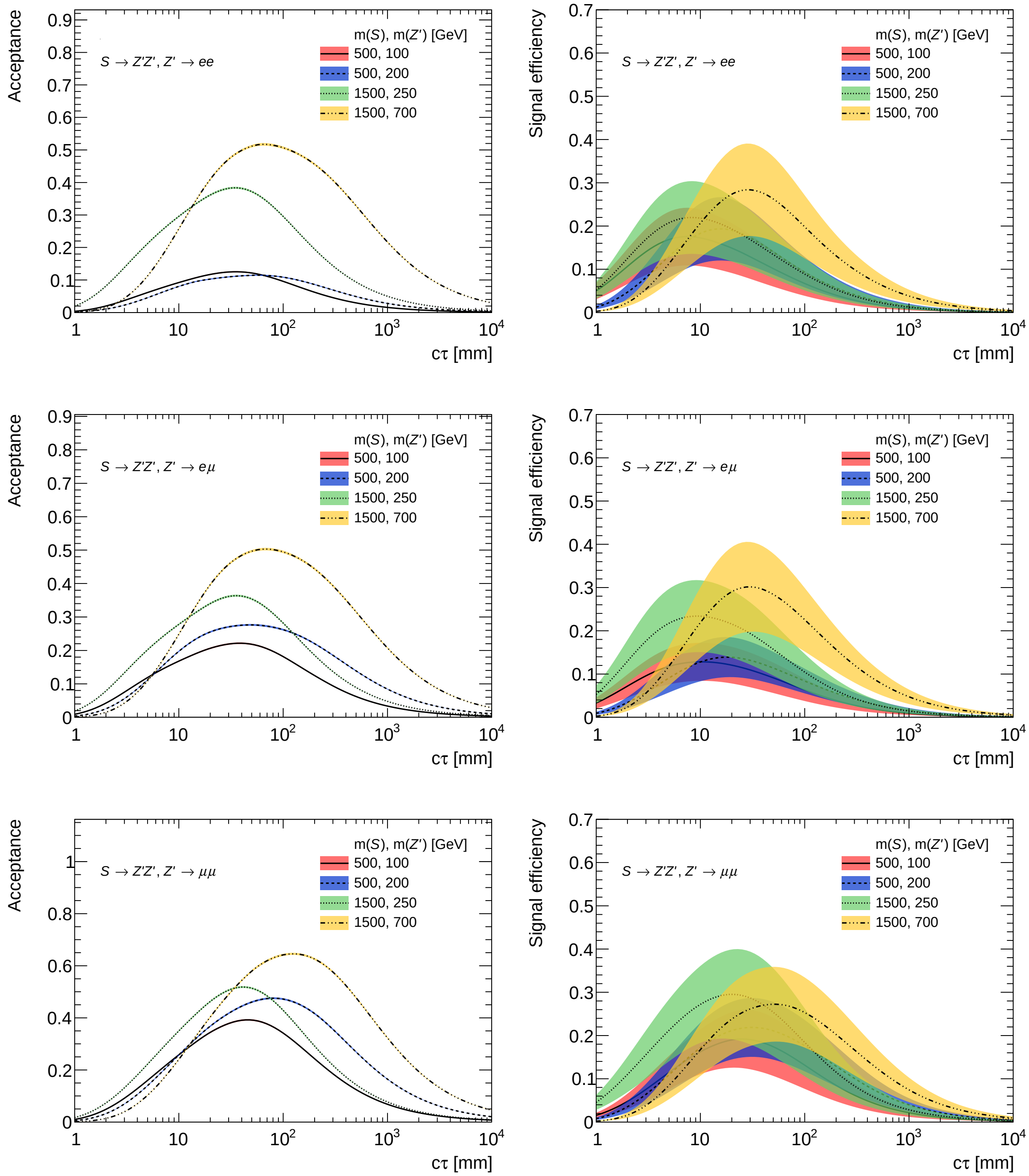

Figure 7.8: Vertex-level acceptance (left) and signal efficiency (right) as a function of decay length ($c\tau$) for a set of Z' signal mc16a samples with a scalar mass of 500 or 1500 GeV and Z' mass of 100, 200, 250, or 700 GeV with Z' decaying to ee (top), $e\mu$ (middle), and $\mu\mu$ (bottom) final states. The colored bands represent the statistical (left) and total (right) uncertainties.

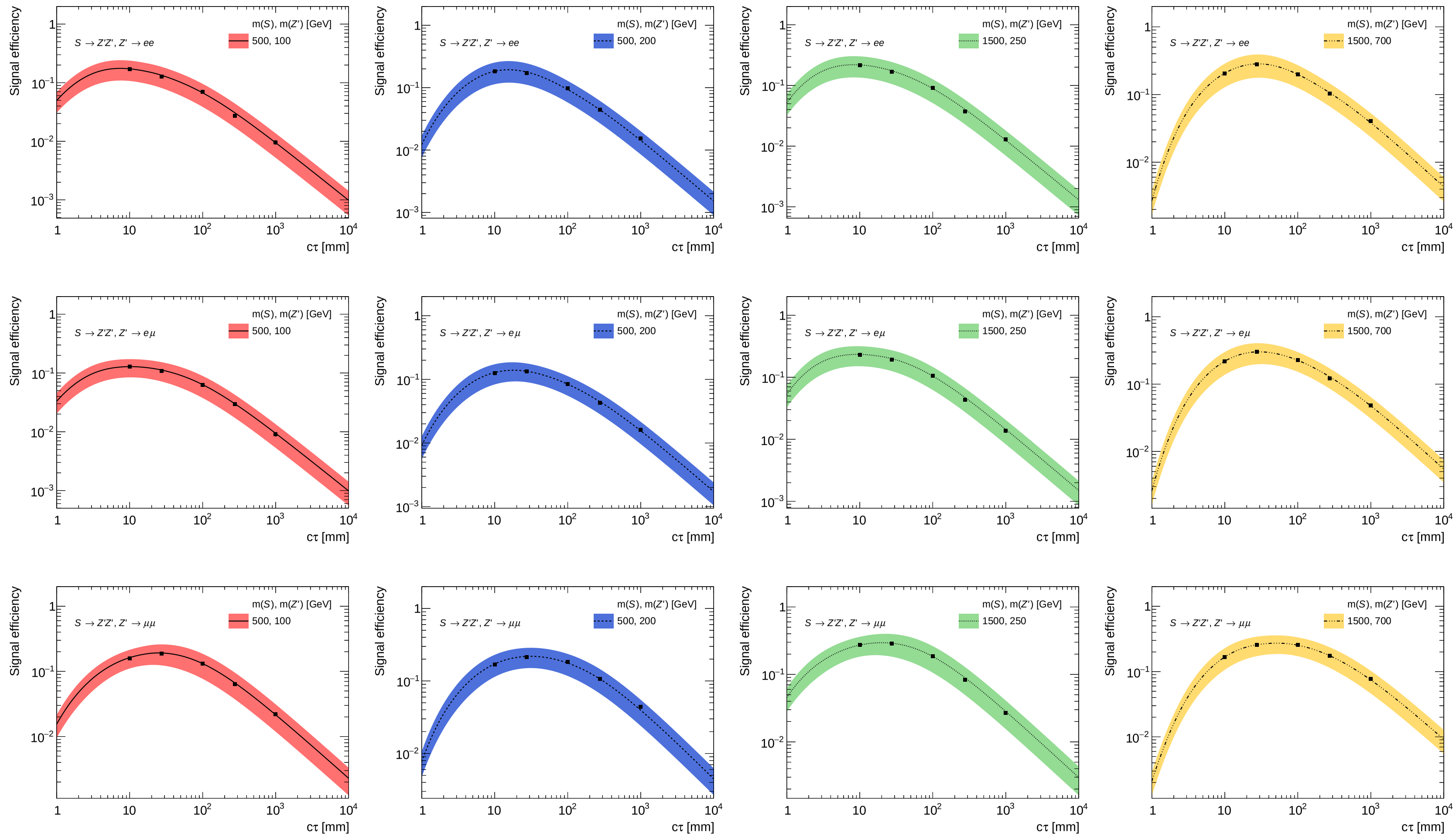

Figure 7.9: Signal efficiency closure test as a function of decay length ($c\tau$) for a set of Z' signal mc16a samples with a scalar mass of 500 or 1500 GeV and Z' mass of 100, 200, 250, or 700 GeV with Z' decaying to ee (top), $e\mu$ (middle), and $\mu\mu$ (bottom) final states. The colored bands represent the total uncertainties.

Table 7.4: MC samples & signal efficiencies for Z' signal model. Each sample contains 10000 events.

m_S (GeV)	$m_{Z'}$ (GeV)	$c\tau_{Z'}$ (mm)	Decay Mode	Signal Efficiency (%)
500	100	10	$\mu\mu$, $e\mu$, ee	14.6, 11.1, 14.5
500	150	10	$\mu\mu$, $e\mu$, ee	15.3, 11.9, 16.6
500	200	10	$\mu\mu$, $e\mu$, ee	14.8, 10.9, 15.4
1000	200	10	$\mu\mu$, $e\mu$, ee	21.5, 20.8, 25.1
1000	350	10	$\mu\mu$, $e\mu$, ee	21.7, 22.5, 25.8
1000	450	10	$\mu\mu$, $e\mu$, ee	16.6, 18.2, 19.0
1500	250	10	$\mu\mu$, $e\mu$, ee	24.1, 19.8, 18.3
1500	450	10	$\mu\mu$, $e\mu$, ee	24.8, 24.7, 22.1
1500	600	10	$\mu\mu$, $e\mu$, ee	21.2, 25.2, 23.5
1500	700	10	$\mu\mu$, $e\mu$, ee	15.0, 18.7, 17.4
500	100	30	$\mu\mu$, $e\mu$, ee	16.0, 9.6, 10.9
500	150	30	$\mu\mu$, $e\mu$, ee	18.1, 10.8, 13.0
500	200	30	$\mu\mu$, $e\mu$, ee	19.0, 11.2, 14.8
1000	200	30	$\mu\mu$, $e\mu$, ee	22.9, 17.5, 19.6
1000	350	30	$\mu\mu$, $e\mu$, ee	25.7, 21.5, 23.1
1000	450	30	$\mu\mu$, $e\mu$, ee	23.3, 22.3, 23.1
1500	250	30	$\mu\mu$, $e\mu$, ee	24.4, 16.6, 14.4
1500	450	30	$\mu\mu$, $e\mu$, ee	28.2, 21.9, 18.6
1500	600	30	$\mu\mu$, $e\mu$, ee	26.7, 26.2, 24.0
1500	700	30	$\mu\mu$, $e\mu$, ee	22.6, 25.6, 23.9
500	100	100	$\mu\mu$, $e\mu$, ee	10.7, 5.1, 5.3
500	150	100	$\mu\mu$, $e\mu$, ee	13.3, 6.2, 6.5
500	200	100	$\mu\mu$, $e\mu$, ee	15.3, 7.2, 7.9
1000	200	100	$\mu\mu$, $e\mu$, ee	14.9, 9.0, 9.3
1000	350	100	$\mu\mu$, $e\mu$, ee	19.6, 12.7, 12.3

m_S (GeV)	$m_{Z'}$ (GeV)	$c\tau_{Z'}$ (mm)	Decay Mode	Signal Efficiency (%)
1000	450	100	$\mu\mu$, $e\mu$, ee	20.5, 15.3, 14.6
1500	250	100	$\mu\mu$, $e\mu$, ee	14.7, 8.3, 7.0
1500	450	100	$\mu\mu$, $e\mu$, ee	20.6, 12.7, 9.9
1500	600	100	$\mu\mu$, $e\mu$, ee	21.4, 15.8, 13.4
1500	700	100	$\mu\mu$, $e\mu$, ee	22.0, 19.3, 17.0
500	100	300	$\mu\mu$, $e\mu$, ee	5.4, 2.3, 2.3
500	150	300	$\mu\mu$, $e\mu$, ee	7.3, 3.0, 3.0
500	200	300	$\mu\mu$, $e\mu$, ee	9.0, 3.8, 3.8
1000	200	300	$\mu\mu$, $e\mu$, ee	7.6, 4.3, 4.1
1000	350	300	$\mu\mu$, $e\mu$, ee	11.4, 6.4, 5.9
1000	450	300	$\mu\mu$, $e\mu$, ee	13.2, 8.3, 7.6
1500	250	300	$\mu\mu$, $e\mu$, ee	7.1, 3.6, 3.1
1500	450	300	$\mu\mu$, $e\mu$, ee	11.1, 6.3, 4.9
1500	600	300	$\mu\mu$, $e\mu$, ee	13.0, 8.4, 6.7
1500	700	300	$\mu\mu$, $e\mu$, ee	15.2, 10.7, 9.0
500	100	1000	$\mu\mu$, $e\mu$, ee	1.7, 0.7, 0.7
500	150	1000	$\mu\mu$, $e\mu$, ee	2.4, 1.0, 1.0
500	200	1000	$\mu\mu$, $e\mu$, ee	3.5, 1.3, 1.4
1000	200	1000	$\mu\mu$, $e\mu$, ee	2.4, 1.4, 1.4
1000	350	1000	$\mu\mu$, $e\mu$, ee	4.0, 2.2, 2.0
1000	450	1000	$\mu\mu$, $e\mu$, ee	5.2, 3.0, 2.6
1500	250	1000	$\mu\mu$, $e\mu$, ee	2.1, 1.1, 0.9
1500	450	1000	$\mu\mu$, $e\mu$, ee	3.7, 2.0, 1.6
1500	600	1000	$\mu\mu$, $e\mu$, ee	4.8, 2.8, 2.1
1500	700	1000	$\mu\mu$, $e\mu$, ee	6.2, 4.0, 3.1

7.2.1 Cosmic Ray Muons

Cosmic ray muons traversing the detector volume can leave hits that result in two back-to-back ID tracks being reconstructed traveling in opposite directions due to the assumption that tracks originate from the center of the detector and travel outwards. The back-to-back nature of the reconstructed muons can be exploited to strongly suppress the background. The muons should have $\sum \eta \approx 0$ and $|\Delta\phi| \approx \pi$, which motivates the event-level cosmic veto: $\Delta R_{\text{cos}} = \sqrt{(|\Delta\phi| - \pi)^2 + (\Sigma\eta)^2} < 0.01$. Figure 7.10 shows the scatter plot of $\sum \eta$ versus $|\Delta\phi|$ for all dimuon DVs passing the full signal cutflow in the cosmic control region, $\Delta R_{\text{cos}} < 0.01$. A large cluster of entries at $|\Delta\phi| = \pi$ and $\sum \eta = 0$ is evident.

Potential contamination of the control region from two cosmic rays crossing one another, called di-cosmics, and creating a signal DV is also considered where the primary difference between single cosmic rays and di-cosmics is the relationship between the impact parameters of the reconstructed muons. Di-cosmic DVs typically have impact parameters which are unrelated to one another because the two tracks come from different muons and, as such, the sum/difference in the transverse/longitudinal impact parameters can be used as a discriminant between single and di-cosmic ray events. Figure 7.10 shows the impact parameters of the two tracks for single cosmic ray muons are similar in d_0 and z_0 as expected if the two tracks belong to the same track, $|d_0^1 + d_0^2| < 2$ mm and $|z_0^1 - z_0^2| < 25$ mm [91]. No off diagonal entries are found, indicating no significant di-cosmic contamination. This is consistent with the previous study of di-cosmic background [91]. It should be noted that any randomly crossing cosmic ray muons are included in the random track crossing background estimate described in Section 7.2.2.

To estimate the cosmic background, the tail of the ΔR_{cos} distribution is fit with an exponential function and extrapolating the function into the signal region, $\Delta R_{\text{cos}} > 0.01$, where the χ^2/n_{dof} fit quality is used to determine the start value of the fit. The start value searches over the range 0.0005 to 0.0025 with an optimal value of 0.0012 for all years considered separately and as one combined Run II dataset. Systematic uncertainty associated with the exponential fit is estimated by varying the start value, bin width for the ΔR_{cos} distribution, and fit function and comparing the background estimate to the nominal value. All fits, however, estimate zero background events and the systematic uncertainties are typically several orders of magnitude lower than the statistical uncertainty (10^{-9} to 10^{-6} compared to 10^{-2}). As such, all cosmic background estimates are reported with statistical uncertainties only.

The fit for the full Run II data is show in Figure 7.11 along with the fits for each year performed separately. The integral for full Run II data is 3.6×10^{-8} events, yielding a background estimate of 0.00 ± 0.04 (stat.) events.

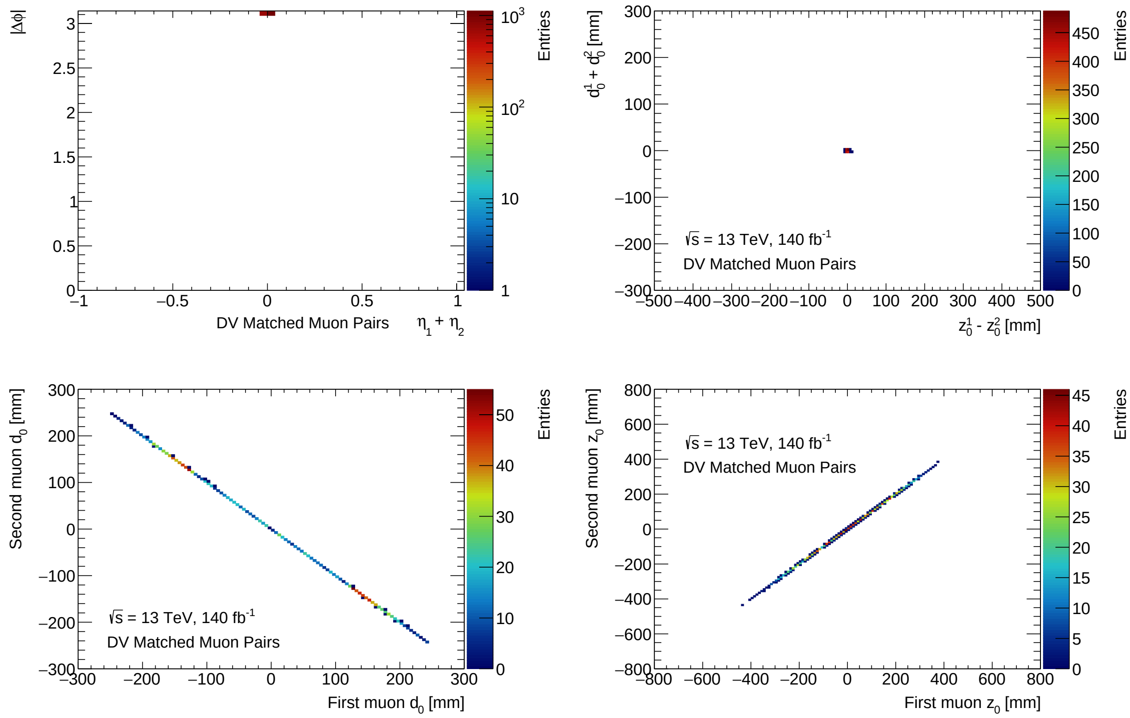

Figure 7.10: The distribution of $|\Delta\phi|$ vs. $\sum \eta$ (top left), $z_0^1 - z_0^2$ vs. $d_0^1 + d_0^2$ (top right), d_0^2 vs. d_0^1 (bottom left), and z_0^2 vs. z_0^1 (bottom right) for cosmic ray muons that form DVs in full Run II data.

7.2.2 Random Track Crossings

The main source of background for the analysis is the random crossing of uncorrelated tracks forming a DV. This background includes the crossing of collision tracks not coming from the PV as well as non-collision tracks such as muon tracks from beam induced backgrounds and cosmic rays.

Event Mixing Strategy

The event mixing is the procedure used to estimate the background from random track crossing where tracks from different events are collected to find the probability of these uncorrelated track pairs crossing. First, tracks are collected from events if they do not originate from the PV and pass the minimum kinematic requirements ($p_T > 10$ GeV and $|\eta| < 2.5$). If the tracks are associated with electrons or muons, they are also required to pass the signal selections from Tables 7.1 and 7.2, respectively. Second, a toy event is constructed by randomly sampling two tracks from different events and a PV from any of the events containing a signal lepton. Each combination of two events as track sources

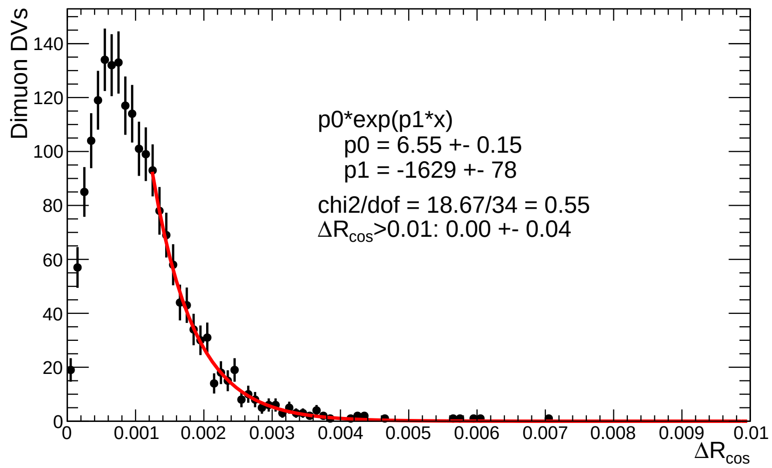

Figure 7.11: Fit to the ΔR_{cos} distributions below the cosmic ray veto for the combined full Run II data. The exponential fits start at 0.0012.

can only be used once, but each track can be sampled up to five times for non-leptonic tracks and ten times for leptonic tracks for the sake of statistics. Third, all the geometric track qualities associated with the PV are recalculated with respect to the new PV and the VSI algorithm from Section 5.1.4 is run over the toy event. Finally, the remaining vertex selections from Sections 7.1.1 and 7.1.2 are applied if a DV is successfully reconstructed with the trigger and filter cuts applied only to the relevant leptons. The probability of crossing, p_{xing}, for a given vertex type (any combination of leptonic or non-leptonic tracks) can be extracted using:

$$N_{\text{vx}}^{\text{mixed}} = N_{\text{pairs}}^{\text{mixed}} \times p_{\text{xing}} \tag{7.5}$$

for the number of successfully reconstructed signal DVs, $N_{\text{vx}}^{\text{mixed}}$, from the mixed candidate track pairs, $N_{\text{pairs}}^{\text{mixed}}$. Then, the estimate of the random crossing background for the number of observed candidate track pairs, $N_{\text{pairs}}^{\text{obs}}$, in the original, unmixed events is given by:

$$N_{\text{vx}} = N_{\text{pairs}}^{\text{obs}} \times p_{\text{xing}} = N_{\text{pairs}}^{\text{obs}} \times \frac{N_{\text{vx}}^{\text{mixed}}}{N_{\text{pairs}}^{\text{mixed}}}. \tag{7.6}$$

Figure 7.12 displays the way in which the VSI algorithm reconstructs a two-track vertex, which is particularly convenient here due to its relevance to the background and toy event nature.

Validations

Several studies are performed on MC in order to validate the event mixing strategy. Simple validations are performed on signal MC where the events are not mixed at all and the VSI

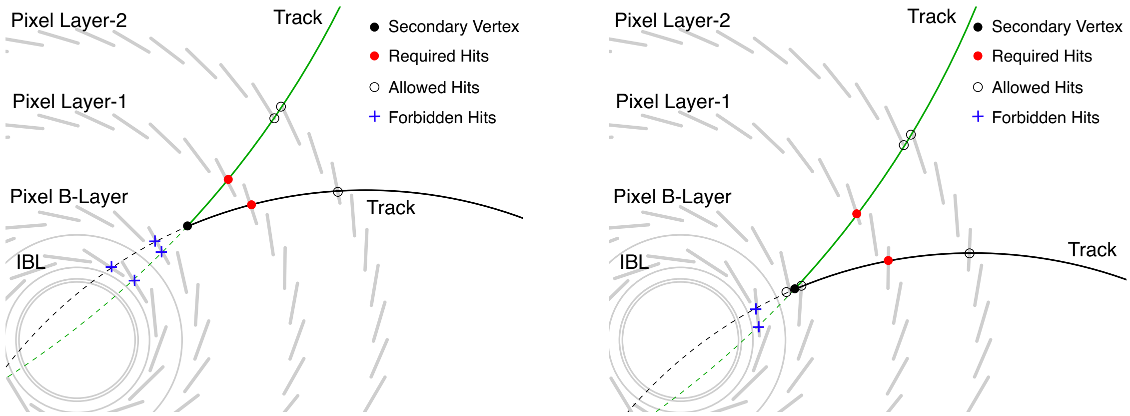

Figure 7.12: An example two-track toy event exhibiting how the VSI reconstruction algorithm forms DVs [63].

algorithm is tested to ensure it successfully recreates the events in the sample. The shifting of the signal tracks given a new PV without mixing the tracks themselves is also validated in signal MC, revealing this process underestimates the final DV yield by ∼1-3%. Finally, the $t\bar{t}$ MC from Table 6.4 can be exploited to compare the random track crossing estimate with the actual number in the sample, since the MC signal region does not need to remain blind.

Unfortunately, zero signal DVs were observed over the 20 million events. Instead the semi-leptonic, "track-muon" and "track-electron," and non-leptonic, "track-track" are studied and the results are summarized in Table 7.5.

Figure 7.13 shows a comparison of the kinematic distributions of the DVs in $t\bar{t}$ MC with those from mixed events. The DVs are reconstructed using track-track combinations, which is the most statistically rich region, and despite the relatively good agreement, the statistics are too limited to conclude that the distributions have been successfully recreated in the event mixing. The number of track-track DVs observed, 3037, is consistent with the prediction, 2639 ± 482 (stat.), and the semi-leptonic DV regions did not have enough statistics to provide meaningful distributions. All average crossing probabilities are on the order of 10^{-7}.

The track-track and semi-leptonic DV regions can also be validated in data because they are orthogonal to the signal region where both tracks are required to be identified as leptons. The results of these validations are summarized in Table 7.6 using 2016 data which provides more statistics for comparison in the track-track combination and kinematic distributions for the mixed and original, unmixed events for this sample are given in Figure 7.14. There is good agreement in the kinematic distributions and the number of observed DVs, 37392, is consistent with the prediction, 39447 ± 2116 (stat.). Similar to the MC, all

Table 7.5: Number of observed and predicted DVs in $t\bar{t}$ MC. The predicted number of vertices is obtained using the number of seed pairs in the data $N_{\text{pairs}}^{\text{obs}}$ and the average crossing probability p_{xing} via Eq. 7.6.

	track-track	track-electron	track-muon
$N_{\text{pairs}}^{\text{obs}}$	6.95×10^9	2.82×10^6	9.59×10^7
Mixed candidate pairs	7.90×10^7	3.54×10^4	2.08×10^6
Mixed signal DVs	30 ± 5.5	0	1 ± 1
Average p_{xing} ($\times 10^{-7}$)	3.80 ± 0.69	0	4.80 ± 4.80
Predicted DVs	2639 ± 482	0	46 ± 46
Observed DVs	3037	1	1

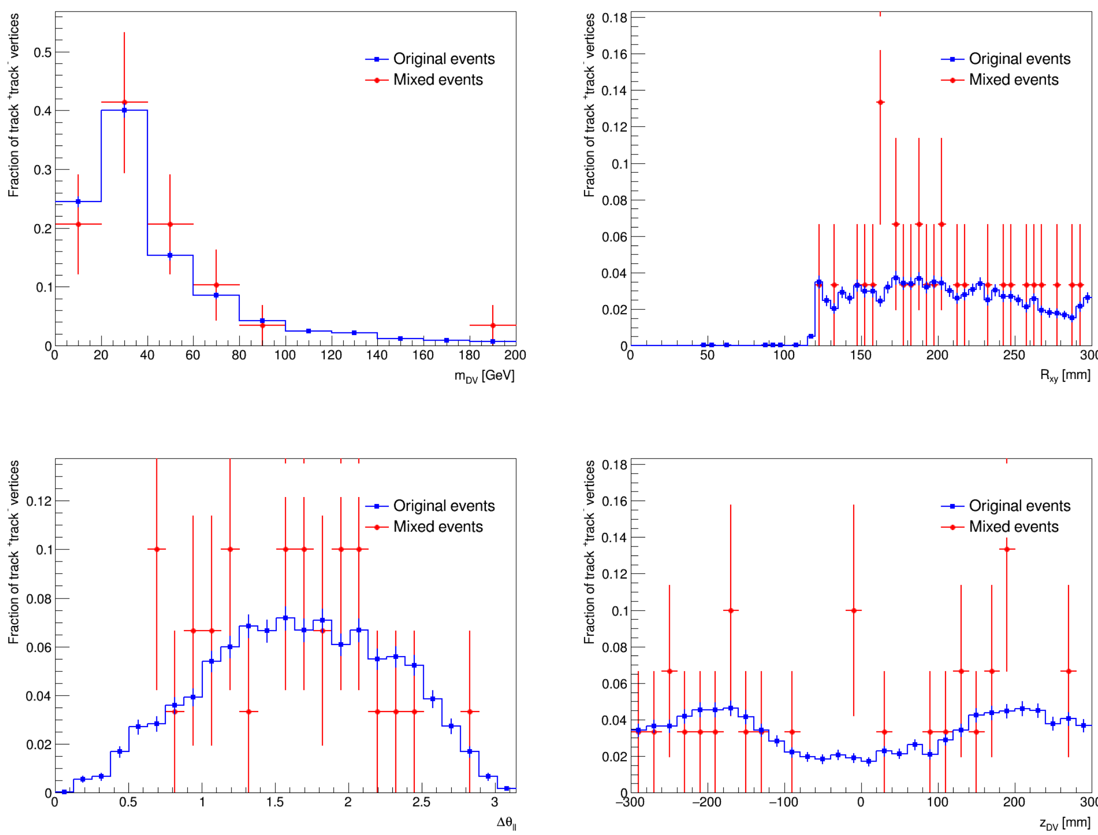

Figure 7.13: Track-track DV yields in $t\bar{t}$ MC as a function of the DV mass (top-left), R_{xy} (top-right), two track opening angle, $\Delta\theta$ (bottom-left), and z (bottom-right), shown for both the original, unmixed (blue) events and the mixed events (red). The mixed events have been normalized to the unmixed events.

crossing probabilities are on the order of 10^{-7}. Given that the track-track channel has the most statistics, the difference of 5.6% between the prediction and observed number of DVs in this channel is assumed to be the systematic uncertainty for all leptonic channels.

Table 7.6: Number of observed and predicted DVs in 2016 data. The predicted number of vertices is obtained using the number of seed pairs in the data $N_{\text{pairs}}^{\text{obs}}$ and the average crossing probability p_{xing} via Eq. 7.6.

	track-track	track-electron	track-muon
$N_{\text{pairs}}^{\text{obs}}$	1.19×10^{11}	9.75×10^{7}	1.43×10^{9}
Mixed candidate pairs	1.05×10^{9}	7.20×10^{6}	3.65×10^{7}
Mixed signal DVs	348 ± 19	2 ± 1	5 ± 2
Average p_{xing} ($\times 10^{-7}$)	3.31 ± 0.23	2.78 ± 1.96	1.37 ± 0.61
Predicted DVs	39447 ± 2116	27 ± 19	196 ± 87
Observed DVs	37392	14	163

Estimate

With the estimation strategy validated, the event mixing results in each of the signal regions and for each year are summarized in Table 7.7. Across all years, zero signal DVs were reconstructed for the ee and $e\mu$ regions and seven were reconstructed for the $\mu\mu$ region. The results summed over all years yield a full Run II random track crossing background estimate of 0.0000 ± 0.0070 (stat.) ± 0.0000 (syst.) for the ee channel, 0.0000 ± 0.0097 (stat.) $\pm$ 0.0000 (syst.) for the $e\mu$ channel, and 0.0245 ± 0.0092 (stat.) $\pm$ 0.0014 (syst.) for the $\mu\mu$ channel. An upper limit of three DVs is assumed for the channels with zero background events following the ATLAS recommendations [92].

7.2.3 Final Background Estimate

Combining the full Run II estimates from cosmic ray muon (for the $\mu\mu$ channel only) and random track crossing backgrounds yields the final background estimates:

$$N_{ee}^{\text{bkg}} = 0.0000 \pm 0.0070 \text{ (stat.)} \pm 0.0000 \text{ (syst.)}, \tag{7.7}$$

$$N_{e\mu}^{\text{bkg}} = 0.0000 \pm 0.0412 \text{ (stat.)} \pm 0.0000 \text{ (syst.)}, \tag{7.8}$$

$$N_{\mu\mu}^{\text{bkg}} = 0.0245 \pm 0.0410 \text{ (stat.)} \pm 0.0014 \text{ (syst.)}, \tag{7.9}$$

where the cosmic ray muon background is included for the $e\mu$ channel following the preliminary recommendations from Section 7.4.1.

Table 7.7: Number of observed and predicted DVs in full Run II data. The predicted number of vertices is obtained using the number of seed pairs in the data $N^{\text{obs}}_{\text{pairs}}$ and the average crossing probability p_{xing} via Eq. 7.6.

2015			
	ee	$e\mu$	$\mu\mu$
$N^{\text{obs}}_{\text{pairs}}$	610	19	129
Mixed candidate pairs	1.84×10^5	3.33×10^4	6.43×10^4
Mixed signal DVs	0	0	1 ± 1
Average p_{xing}	0	0	1.56×10^{-5}
Predicted DVs	0	0	$(2.01 \pm 2.01) \times 10^{-3}$
2016			
	ee	$e\mu$	$\mu\mu$
$N^{\text{obs}}_{\text{pairs}}$	4.40×10^3	1.29×10^3	2.90×10^3
Mixed candidate pairs	5.92×10^6	8.36×10^5	1.49×10^6
Mixed signal DVs	0	0	3 ± 1.7
Average p_{xing}	0	0	2.02×10^{-6}
Predicted DVs	0	0	$(5.85 \pm 3.38) \times 10^{-3}$
2017			
	ee	$e\mu$	$\mu\mu$
$N^{\text{obs}}_{\text{pairs}}$	2.06×10^4	1.49×10^3	2.29×10^3
Mixed candidate pairs	1.27×10^7	4.89×10^5	6.89×10^5
Mixed signal DVs	0	0	3 ± 1.7
Average p_{xing}	0	0	4.36×10^{-6}
Predicted DVs	0	0	$(9.97 \pm 5.76) \times 10^{-3}$
2018			
	ee	$e\mu$	$\mu\mu$
$N^{\text{obs}}_{\text{pairs}}$	2.50×10^4	2.07×10^3	3.28×10^3
Mixed candidate pairs	2.68×10^6	1.38×10^5	2.20×10^5
Mixed signal DVs	0	0	0
Average p_{xing}	0	0	0
Predicted DVs	0	0	0
Total			
	ee	$e\mu$	$\mu\mu$
$N^{\text{obs}}_{\text{pairs}}$	5.01×10^4	1.48×10^3	8.59×10^3
Mixed candidate pairs	2.15×10^7	1.50×10^6	2.46×10^6
Mixed signal DVs	0	0	7 ± 2.6
Average p_{xing}	0	0	2.85×10^{-6}
Predicted DVs	0	0	$(2.45 \pm 0.92) \times 10^{-2}$

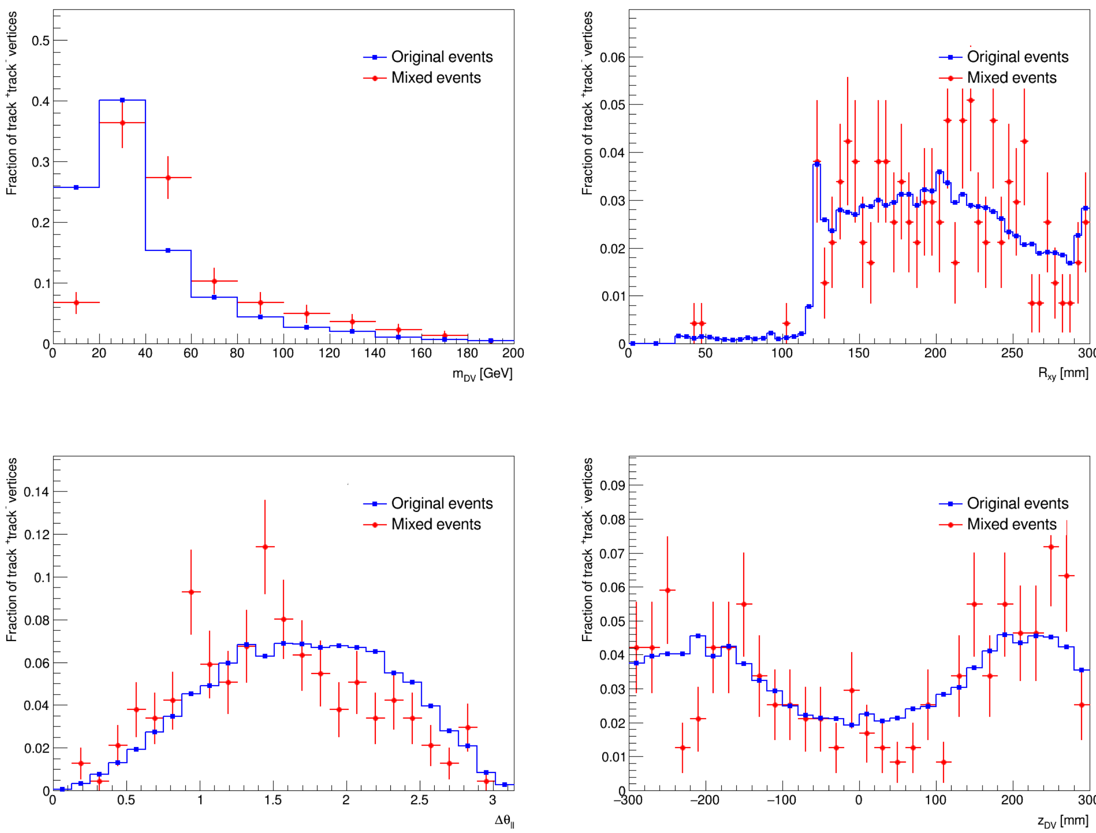

Figure 7.14: Track-track DV yields in 2016 data as a function of the DV mass (top-left), R_{xy} (top-right), two track opening angle, $\Delta\theta$ (bottom-left), and z (bottom-right), shown for both the original, unmixed (blue) events and the mixed events (red). The mixed events have been normalized to the unmixed events.

7.3 Systematic Uncertainties

The signal efficiencies from Section 7.1.3 have several associated errors including the statistical error from the limited number of signal MC events as well as several systematic uncertainties which are summarized here. When studying the signal efficiency in MC, several corrective weights, called scale factors, are applied to the MC to more closely match the data/detector properties of the appropriate data-taking period. In particular, weights associated with imperfect modeling of pileup distributions, identification efficiencies, trigger efficiencies, and track and vertex reconstruction efficiencies in MC each have an associated systematic uncertainty included in the signal efficiency. Using Equation 4.2 to estimate the expected yield of any particular model also needs to include the 0.83% [41] uncertainty on the full Run II luminosity and the theoretical uncertainty calculated by the MC generators on σ. The systematic uncertainties on the background estimates are also summarized in Section 7.3.7.

7.3.1 MC Modeling

Several theoretical systematic uncertainties are considered for the MC generation of the signal Z' samples, namely the uncertainty on the cross section, uncertainties on the factorization and renormalization scales, the inter-PDF and intra-PDF uncertainties, and uncertainties associated with initial-state radiation (ISR), final-state radiation (FSR), and multiple parton interactions (MPI). The theoretical cross section is calculated by the the MC generator in Section 6.2.1 with zero associated uncertainty. Generally, the remaining uncertainties are determined by applying alternative methods or weights during MC generation and comparing the truth-level acceptance of the alternatively generated samples to the nominal acceptance for the same parameter point. The scale and PDF uncertainties are estimated by varying the MC generation procedure for alternative signal samples not considered here. Uncertainties from the variation in factorization and renormalization scales are considered negligible with a maximum deviation of 0.34% in the acceptance. The inter-PDF uncertainty is estimated by varying the PDF set used in MC generation where the largest deviation of 5% is conservatively assigned for all signal samples. Similarly, the intra-PDF uncertainty is estimated by varying the weight set used within the nominal `NNPDF23LO` PDF set and the largest deviation of 1.4% is conservatively used for all signal samples. Finally, the ISR, FSR, and MPI uncertainties are estimated by varying the `A14` tune in Z' MC generation with the largest combined deviation of 3% conservatively applied for all signal samples. Added in quadrature, a conservative 6% systematic uncertainty associated with the MC modeling is used for all signal samples.

7.3.2 Pileup Modeling

Weights are applied to MC samples to correct the pileup distributions to match those in data more closely [93]. This reweighting procedure reproduces reasonably well the pileup distributions in data as presented in Figure 7.15 for the same alternative signal samples used in Section 7.3.1. Variations in the weight propagated through the signal efficiency typically results in an uncertainty of a few percent, as summarized in Table 7.11.

7.3.3 Lepton Identification and Reconstruction

Due to the use of modified electron and muon identification working points, potential differences in the lepton reconstruction efficiency between data and MC has been investigated. Because these modified working points specifically remove d_0 and Pixel hit requirements for identification, the d_0-dependent uncertainty is included in the LRT/VSI systematic er-

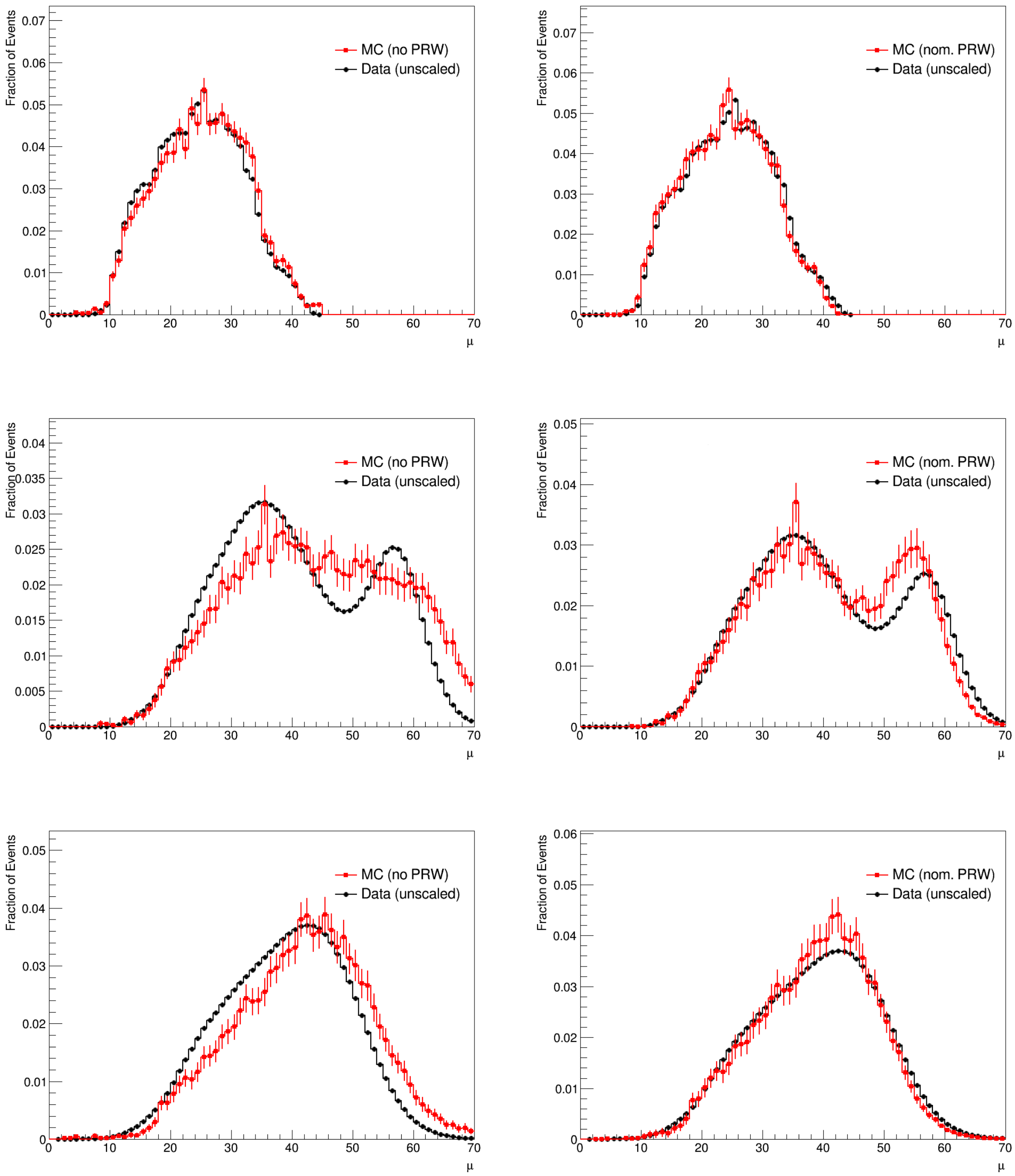

Figure 7.15: Number of pileup vertices in data and in MC without (left) and with (right) pileup reweighting using the nominal weight. The top row compares mc16a with 2015 and 2016 data, the middle row compares mc16d with 2017 data, and the bottom row compares mc16e with 2018 data. For 2015 and 2016 data, the average interactions over lumi-blocks is compared while for 2017 and 2018 the actual interactions for each event are compared.

ror discussed in Section 7.3.5. Indeed, Figure 7.16 shows that the identification working points used do not have any significant d_0 dependence above the relevant p_T thresholds in mc16d. All leptons are required to pass the signal kinematic, quality, and overlap removal cuts. The thresholds are for the different pairings of lepton trigger and DRAW_RPVLL filter requirements for single electrons, pairs of electrons, and single muons. It is evident that the reconstructed leptons have negligible dependence on the leptons' transverse impact parameter, except for muons, which have a modest dependence. In the region where the modified muon identification efficiency begins to decrease, $|d_0| \gtrsim 150$ mm, statistics are quite limited, even for the signal MC and this dependence becomes less pronounced for increasing LLP boost. These modified working points can, therefore, be considered as independent of lepton impact parameter, allowing the use of the tag-and-probe results of the following study.

Tag-and-Probe Strategy

Standard tag-and-probe studies can be performed over the prompt $Z \to \ell\ell$ MC from Table 6.4 given the lack of impact parameter dependence of the identification working points. The tag electron and probe electron [94–96] are selected using the cuts defined in Table 7.8. Similarly, the tag and probe muons [97] are defined with the selections in Table 7.9. In addition, tag-and-probe pairs must have opposite charge, $|m(\ell^+\ell^-) - m(Z)| < 10$ GeV, and $\Delta R(\text{tag}, \text{probe}) > 0.4$. The ΔR cut ensures that the probe lepton does not match to the trigger RoI of the tag lepton.

Care must be taken to remove background contributions in data when using the invariant dilepton mass as the discriminating variable between signal and background. Background templates are formed using probes that pass the denominator requirements from Tables 7.8 and 7.9 with an inverted modified identification working point. Due to the loose requirements of the working point, the signal leptons have a small contribution in the base background in which the cuts are inverted. This contribution is estimated by the signal contamination template, which is formed by inverting the same cut in MC, where all leptons are required to be truth-matched to a Z-boson such that the distributions consist of only signal leptons. Normalization is performed differently for the denominator and numerator background templates where both use a high-mass side-band region, $120 < m_{ee} < 250$ GeV. For the denominator, signal contamination is removed in the tails of the background template before normalizing it to the distribution. For the numerator, the base background template is normalized to the same-sign invariant mass distribution in data where probes are required to pass the modified identification working point. The same-sign distribution is used for the numerator due its lower signal contamination than the opposite-sign distribution.

The invariant mass distributions for selected lepton pairs where the MC distribution has been normalized to the distribution for each respective data taking period are shown in Figure 7.17. Mass spectra before the background subtractions are on the far left and

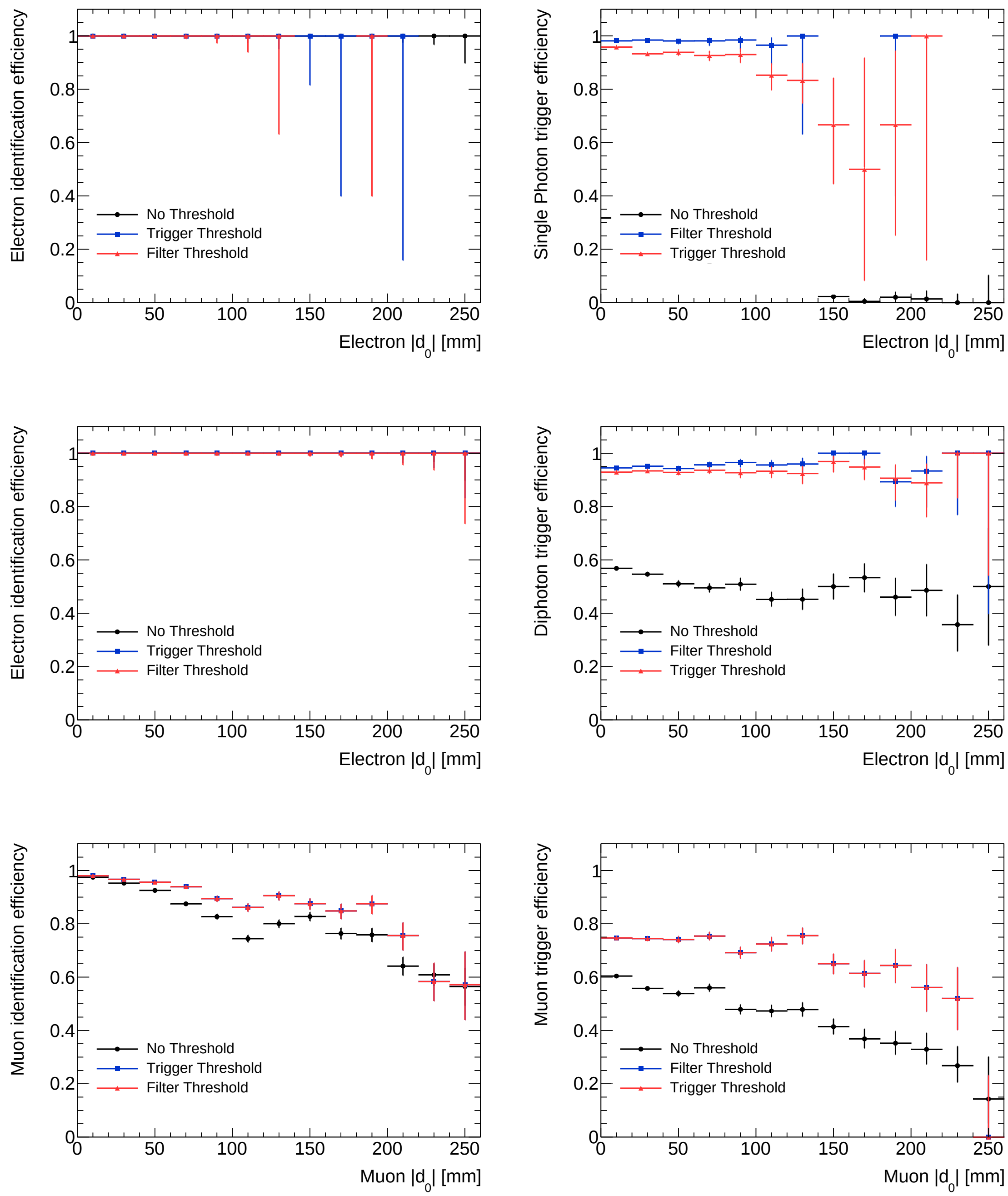

Figure 7.16: Identification (left) and trigger (right) efficiency as a function of the lepton transverse impact parameter for the single γ and single e (top), $\gamma\gamma$, $e\gamma$ and ee (middle), and μ (bottom). Efficiences are extracted from the mc16d samples which contain a scalar mass of 500 GeV and Z' mass of 100 GeV, all decay lengths ($c\tau$), and all decay modes. Efficiencies with three different lepton p_T thresholds are shown: (1) no additional threshold, (2) threshold matching the trigger value, (3) threshold matching the appropriate filter values from Table 6.6.

Table 7.8: Object selection criteria for tag-and-probe electrons in $Z \to \ell\ell$ studies.

Cut	Tag	Identification probe	Trigger probe
p_T (GeV)	> 27	> 10	> 30
Trigger	`HLT_e26_lhtight_nod0_ivarloose`	–	–
(2015 only)	(`HLT_e24_lhmedium_L1EM20VH`)		
$\|\eta\|$	< 1.37 or $1.52 - 2.47$	< 2.47	< 2.47
Identification	TightLH	–	Modified VeryLooseLH
Object quality	Yes	Yes	Yes
Track isolation	$p_T^{cone0.2} < 0.1$	–	–
Jet veto	No	Yes	Yes

Table 7.9: Object selection criteria for tag-and-probe muons in $Z \to \ell\ell$ studies.

Cut	Tag	Identification probe	Trigger probe
p_T (GeV)	> 28	> 10	> 30
Trigger	`HLT_mu26_ivarmedium`	–	–
(2015 only)	(`HLT_mu20_iloose_L1MU15`)		
$\|\eta\|$	< 2.4	< 2.5	< 1.05
Identification	Medium and Combined	–	Modified Loose and Combined
Isolation	Loose	–	–
d_0 significance	< 3	–	–
$\Delta z_0 \sin\theta$ (mm)	< 0.5	–	–

middle right while the distributions after the subtractions are on the middle left and far right and show good improvement in the agreement between data and MC.

Tag-and-Probe Results

The results from the tag-and-probe procedure are used to define the identification efficiency:

$$\epsilon_{\text{Identification}} = \frac{\text{Number of identification probes passing identification}}{\text{Number of identification probes}}. \tag{7.10}$$

The efficiencies and ratio of MC vs. data are plotted in η vs. E_T and ϕ vs. η for electrons and muons, respectively. The results are summarized in Figures 7.18-7.19, giving the modified

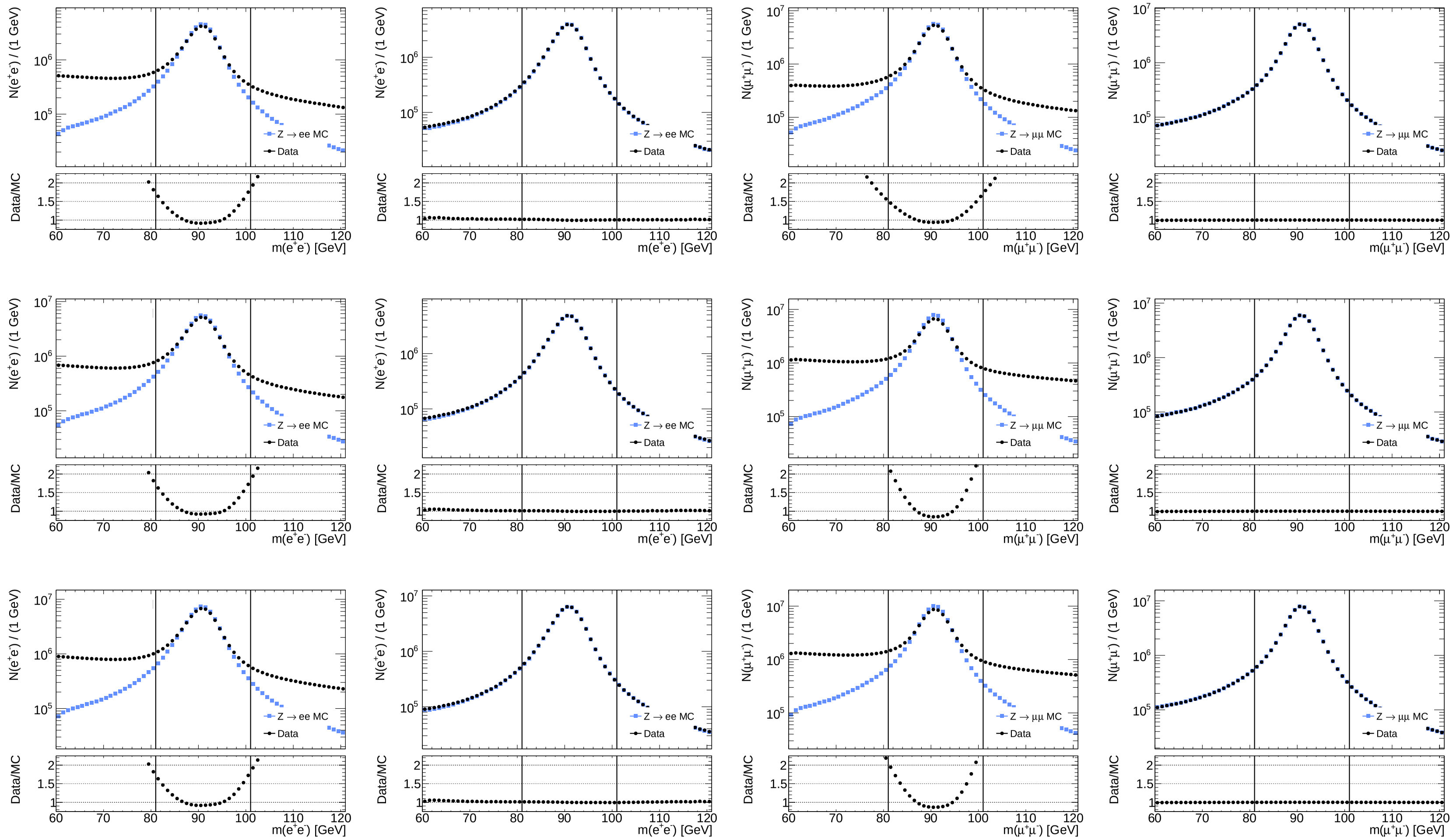

Figure 7.17: Invariant mass distributions of the tag and probe electron pairs used to study the efficiencies of the modified electron working point, `ElectronLikelihoodVeryLooseOfflineConfig2017_nod0_Smooth` (far left and middle left), and modified `Loose` muon working point (middle right and far right) in the 2015/2016 data and the $Z \to \ell\ell$ mc16a sample (top), 2017 data and mc16d (middle), and 2018 and mc16e (bottom). The distributions are given for both before (far left and middle right) and after (middle left and far right) the background subtractions. The MC is normalized to the data in the signal region, the central region delineated by the two lines.

identification scale factors, statistical errors, and systematic errors for each MC period[4].

Scale factor values for the modified lepton identification working points are close to 1.00 in most regions. The modified electron identification working point, `ElectronLikelihoodVeryLooseOfflineConfig2017_nod0_Smooth`, has scale factors $\sim$1.00 except in the less well modeled crack region where it can be as large as 1.02 and in the high E_T and η region where it can be as small as $\sim$0.90. The statistical uncertainties have values as large as $\sim$10% but typically $\lesssim$2%. For the modified `Loose` muon identification working point, scale factors vary from 0.98 to 1.01 and the statistical errors are small, typically $\lesssim$0.5% outside a small region near the center of the detector.

Systematic uncertainties for the scale factors have two contributions, variations on the tag requirements and the Z mass window used for the signal region. For electrons, the tag requirements are changed to have an isolation requirement of $E_T^{cone0.4}$ <5 GeV and a loosened identification requirement of MediumLH. For muons, the tag requirements are changed to have its track-quality criteria and identification requirement modified to d_0 significance $<$ 2.5 mm and $|\Delta z_0 \sin\theta| <$ 0.4 mm and `Tight`. The mass window is changed from 10 GeV to 5 and 15 GeV around the Z boson mass for both leptons. The average variations in the efficiencies in data and MC are then used as the systematic error. The non-closure in each period is less than 0.01% and 0.02% for electrons and muons, respectively, so no additional systematic is added. These systematic uncertainties added in quadrature yield a total systematic error of $\sim$1% and are added to the appropriate statistical uncertainties.

7.3.4 Signal Triggers

As mentioned in Section 6.3.1, the signal HLT selection is based on the lack of impact parameter dependence of the triggers where electrons are selected using photon triggers that depend on calorimeter signals and muons are selected using MS information exclusively. Thus, the lack of ID track information for significantly displaced leptons at the trigger stage, prior to the LRT algorithm running, can be circumvented. Conveniently, this also allows studies on the differences between MC and data trigger efficiencies to be considered independent of any d_0 dependence in LRT/VSI covered by the uncertainties in Section 7.3.5 As has been shown in Figure 7.16, the photon triggers `HLT_g140_loose` and `HLT_2g50_loose` have no significant d_0 dependence after imposing p_T thresholds of this analysis and, as such, the standard tag-and-probe analysis with prompt $Z \to ee$ MC can be used to study the efficiency of these triggers. Similarly, the muon trigger `HLT_mu60_0eta105_msonly` also has no significant d_0 dependence in the statistically rich regions ($|d_0| \lesssim$ 150 mm) because of

[4]Scale factors are applied to MC, so 2015 and 2016 data are combined and compared against mc16a, 2017 data is compared to mc16d, and 2018 data is compared to mc16e.

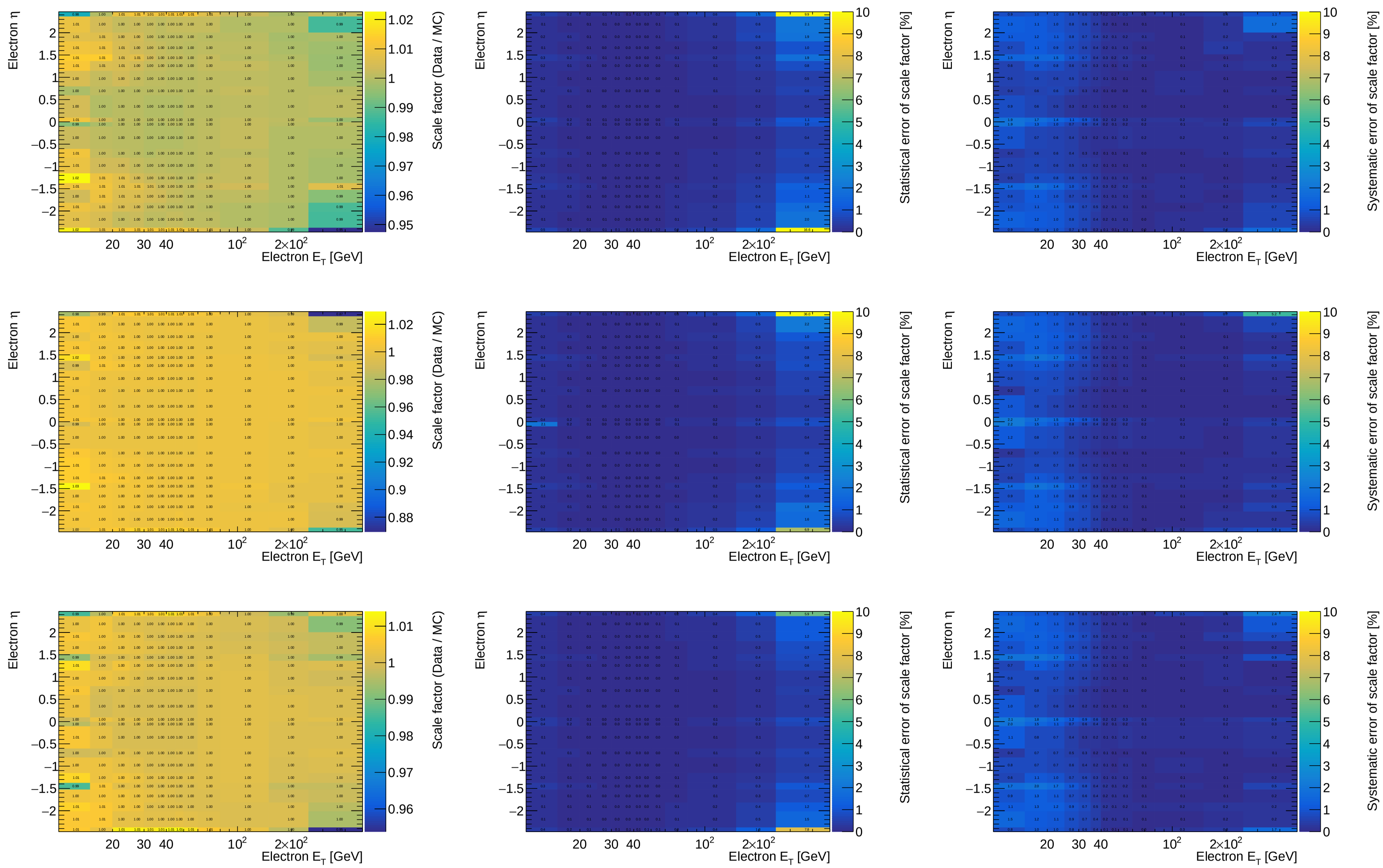

Figure 7.18: Scale factors (left) with their statistical (middle) and systematic (right) error for the modified electron identification working point, `ElectronLikelihoodVeryLooseOfflineConfig2017_nod0_Smooth`, as a function of the probe E_T and η extracted from a comparison of 2015/2016 data and mc16a (top), 2017 data and mc16d (middle), and 2018 data and mc16e (bottom).

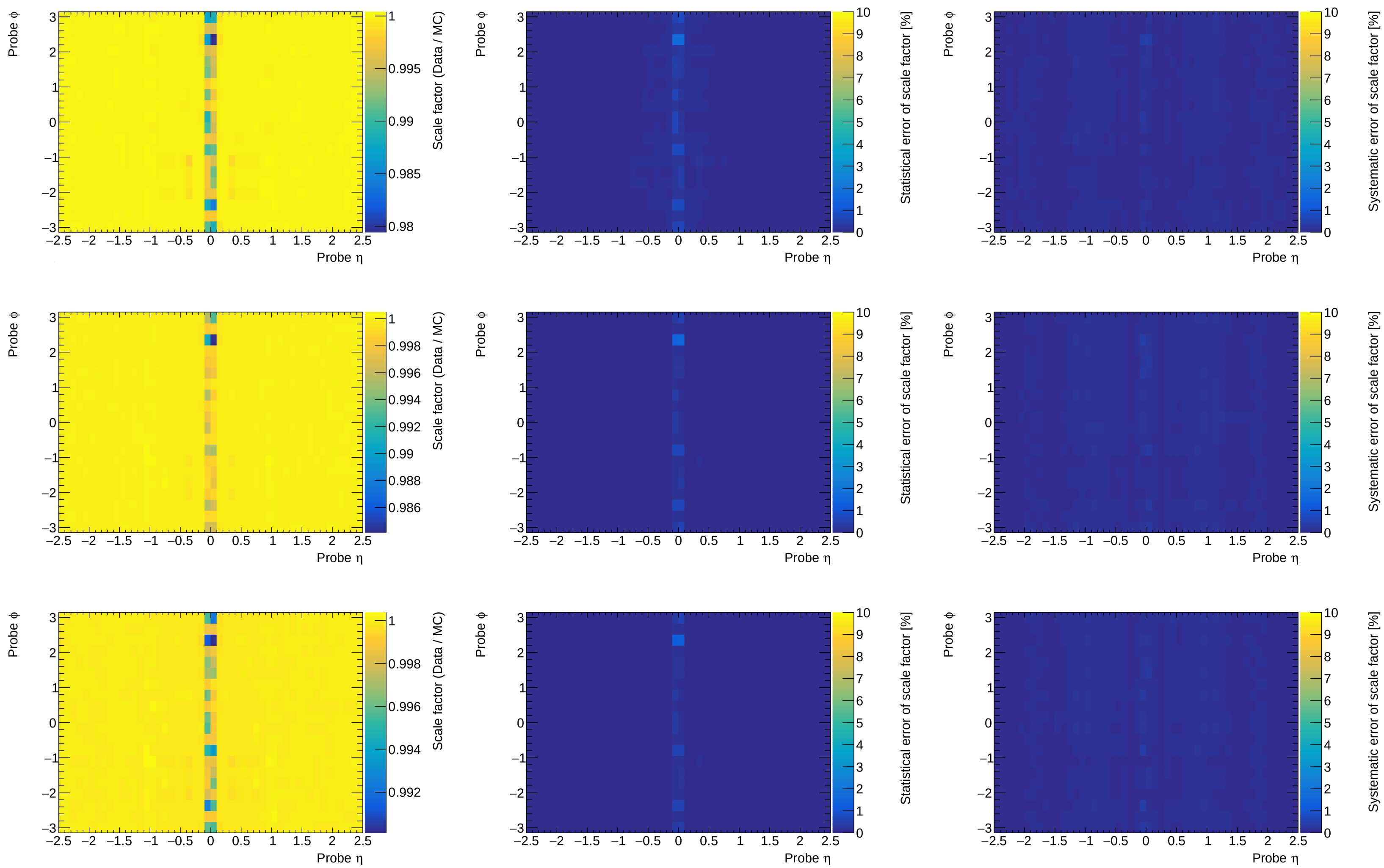

Figure 7.19: Scale factors (left) with their statistical (middle) and systematic (right) error of the modified `Loose` muon working point as a function of the probe η and ϕ extracted from a comparison of 2015/2016 data and mc16a (top), 2017 data and mc16d (middle), and 2018 data and mc16e (bottom).

its reliance on MS rather than ID information[5]. It is evident that with no additional p_T cuts on the signal leptons beyond the kinematic ones, each of the triggers has low efficiency at large impact parameters. As the thresholds are raised to those of the respective trigger values, however, this dependence is reduced, especially for the photon triggers. Increasing these thresholds to the values of the filters of Table 6.6 eliminates the dependence from the triggers except the small dependence for the muon trigger at large transverse and longitudinal impact parameters.

Tag-and-Probe Strategy

Using the same MC samples as in Section 7.3.3, scale factors and systematic errors can be derived for the photon and muon triggers. When studying the efficiencies of the diphoton trigger, the single photon trigger `HLT_g50_loose` is measured instead to determine a scale factor that can later be applied to electron pairs assuming the probability to match the diphoton version is simply the product of the probability for each to independently match the single photon version. While the prescription from Section 7.3.3 was particularly beneficial for identification efficiency studies, trigger efficiency studies involve considerably less background and signal contamination due to the additional stipulations that the leptons must meet the p_T threshold and pass the modified identification working points such that the results of this tag-and-probe study are independent of those in Section 7.3.3. Thus, the denominator background is estimated similar to the numerator background, where the same-sign distribution of the denominator is used to scale the background template and is subtracted directly without correcting for signal contamination.

The agreement in the mass distribution is quite good when the MC is normalized to the data in the signal region, as evident in Figures 7.20-7.21, for each data taking and corresponding MC period. Mass spectra before the background subtractions are on the far left and middle right (left) while the distributions after the subtractions are on the middle left and far right (right) and show good improvement in the agreement between data and MC for the photon (muon) triggers. The agreement between the mass distributions for each of the HLTs and in each period indicate that the simplified background subtraction method is sufficient for the study. When compared to Figure 7.17, the mass spectra of Figures 7.20 and Figure 7.21 are most significantly impacted by the the additional p_T requirements for the probe lepton, removing low momentum leptons from the tails, and the identification requirement to reject background.

As an additional check for muon modeling in MC, the χ^2/n_{dof} is compared between probe muons in data and MC. This value represents the quality of the match between the ID

[5] For the maximal LLP decay length studied in the analysis, $c\tau = 1000$ mm, muons with $d_0 > 150$ mm account for only 20% of the signal muons decreasing to $\sim$6% for an intermediate decay length of 100 mm and $\sim$0% for the minimal decay length of 10 mm.

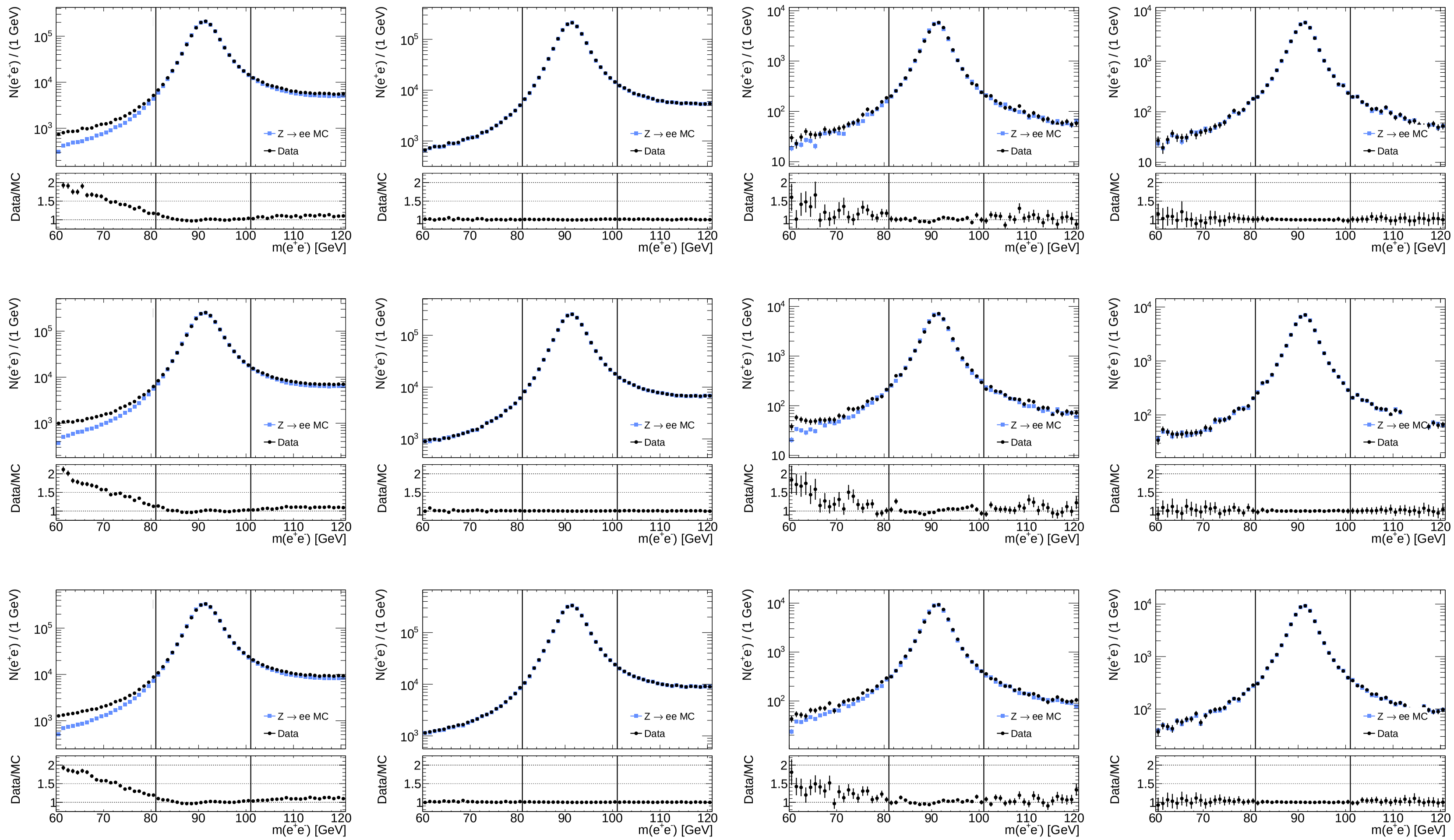

Figure 7.20: Invariant mass distributions of the tag and probe electron pairs used to study the efficiencies of the HLT_g50_loose trigger (far left and middle left) and the HLT_g140_loose trigger (middle right and far right) in the 2015/2016 data and the $Z \to \ell\ell$ mc16a sample (top), 2017 data and mc16d (middle), and 2018 and mc16e (bottom). The distributions are given for both before (far left and middle right) and after (middle left and far right) the background subtractions. Only pairs with a probe electron $p_T > 60$ GeV (far left and middle left) and $p_T > 160$ GeV (middle right and far right) are considered. The MC is normalized to the data in the signal region, the central region delineated by the two lines.

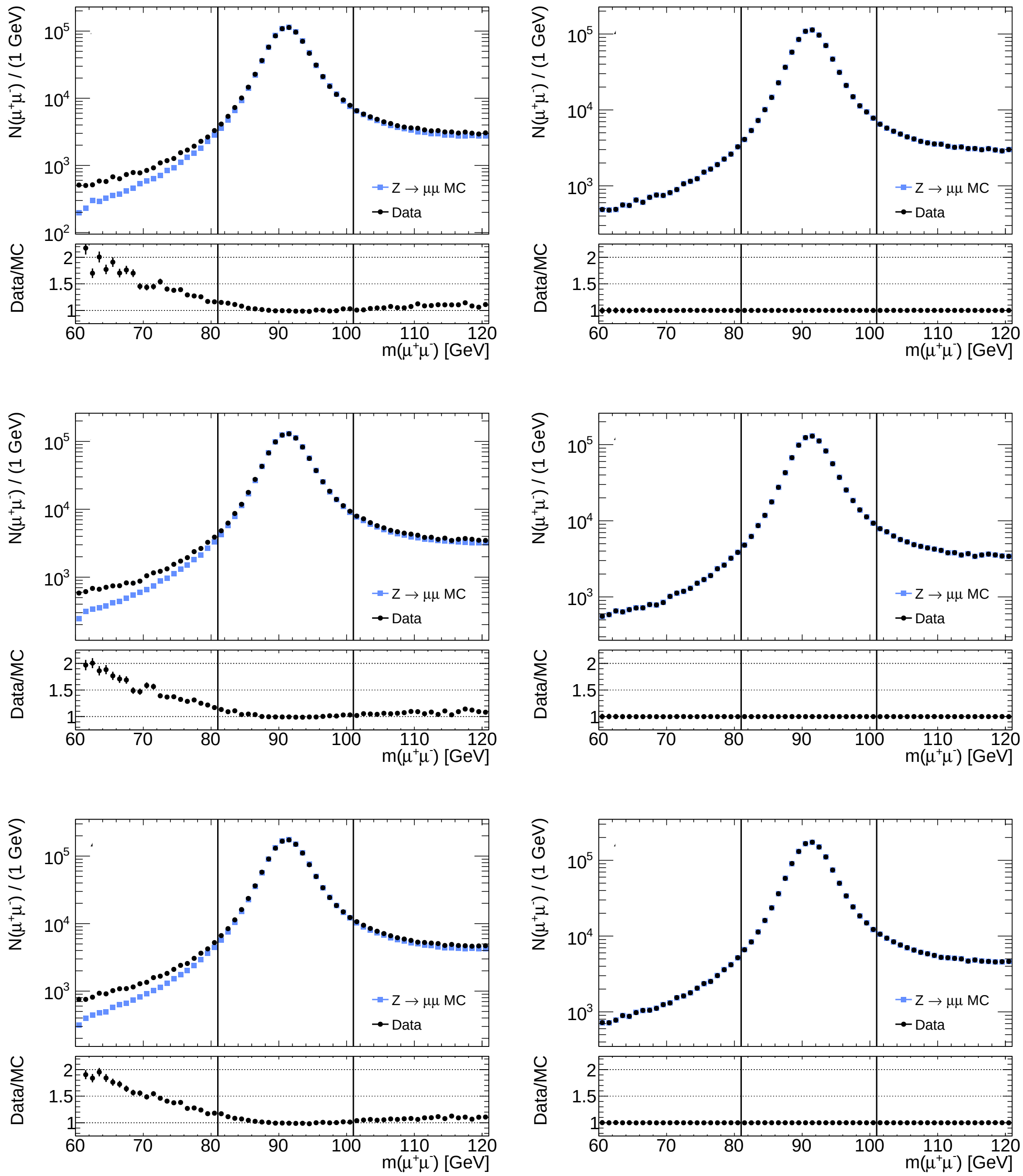

Figure 7.21: Invariant mass distributions of the tag and probe muon pairs used to study the efficiencies of the HLT_mu60_0eta105_msonly trigger in the 2015/2016 data and the $Z \rightarrow \ell\ell$ mc16a sample (top), 2017 data and mc16d (middle), and 2018 and mc16e (bottom). The distributions are given for both before (left) and after (right) the background subtractions. The MC is normalized to the data in the signal region, the central region delineated by the two lines. Only probes with $p_T > 60$ GeV are considered.

and MS track that form `Combined` muon and it is important to know how well MC models the muons that pass the $\chi^2/n_{dof} < 5$ quality criteria imposed by the `DRAW_RPVLL`. The goodness of fit is shown in Figure 7.22 for the modified muon identification and signal muon trigger studies performed on each data-taking period and corresponding MC campaign. It is evident that, in all cases, the data distribution has a higher tail but most of the data and MC (> 99%) satisfy the χ^2/n_{dof} requirement in the region where there is good agreement (∼0.2%) in the first bin, $\chi^2/n_{dof} < 1$, containing ∼97% of the probe muons and, hence, no correction for the discrepancy will be applied. There have also been no background subtractions performed on the data which would improve the quality distribution, matching the MC more closely.

Tag-and-Probe Results

Analogous to Equation 7.10, the efficiency for the triggers can be defined as:

$$\epsilon_{\text{Trigger}} = SF_{\text{Identification}} \times \frac{\text{Number of trigger probes matched to trigger}}{\text{Number of trigger probes}} \tag{7.11}$$

with the added factor accounting for the identification requirement on the probes. The scale factors for each trigger use the same standard binning as the corresponding lepton identification scale factor. Despite some residual p_T and z_0 dependence in the ratio of trigger efficiencies, there are no significant trends above the relevant filter thresholds in regions with good statistics. Figures 7.23-7.25 summarize the results of the tag-and-probe study with the trigger scale factors, statistical errors, and systematic errors for each MC period.

The average scale factor for `HLT_g50_loose` and `HLT_g140_loose` are each ∼0.99 above the appropriate filter threshold and outside the crack region and extreme values in $|\eta|$. The statistical errors can be as large as 8% in the crack regions, but are ∼0.2% elsewhere. The scale factors for `HLT_mu60_0eta105_msonly` vary between 0.98 and 1.01 with an average of 1.0 and the statistical error is typically $1-4\%$ outside regions where there are small gaps in the detector.

Systematic errors from the same two sources as for Section 7.3.3 are added in quadrature, yielding ∼0.1% and ∼0.2% for the diphoton and single photon triggers, respectively. The non-closure in each period is less than 0.15% and 0.33% for the diphoton and single photon triggers, respectively, so no additional systematic is added. With the same procedure for systematic uncertainties as for the modified muon identification working point, errors of $\sim 1\%$ are added to the statistical uncertainties. The non-closure in each period is less than 0.01%, so no additional systematic is added.

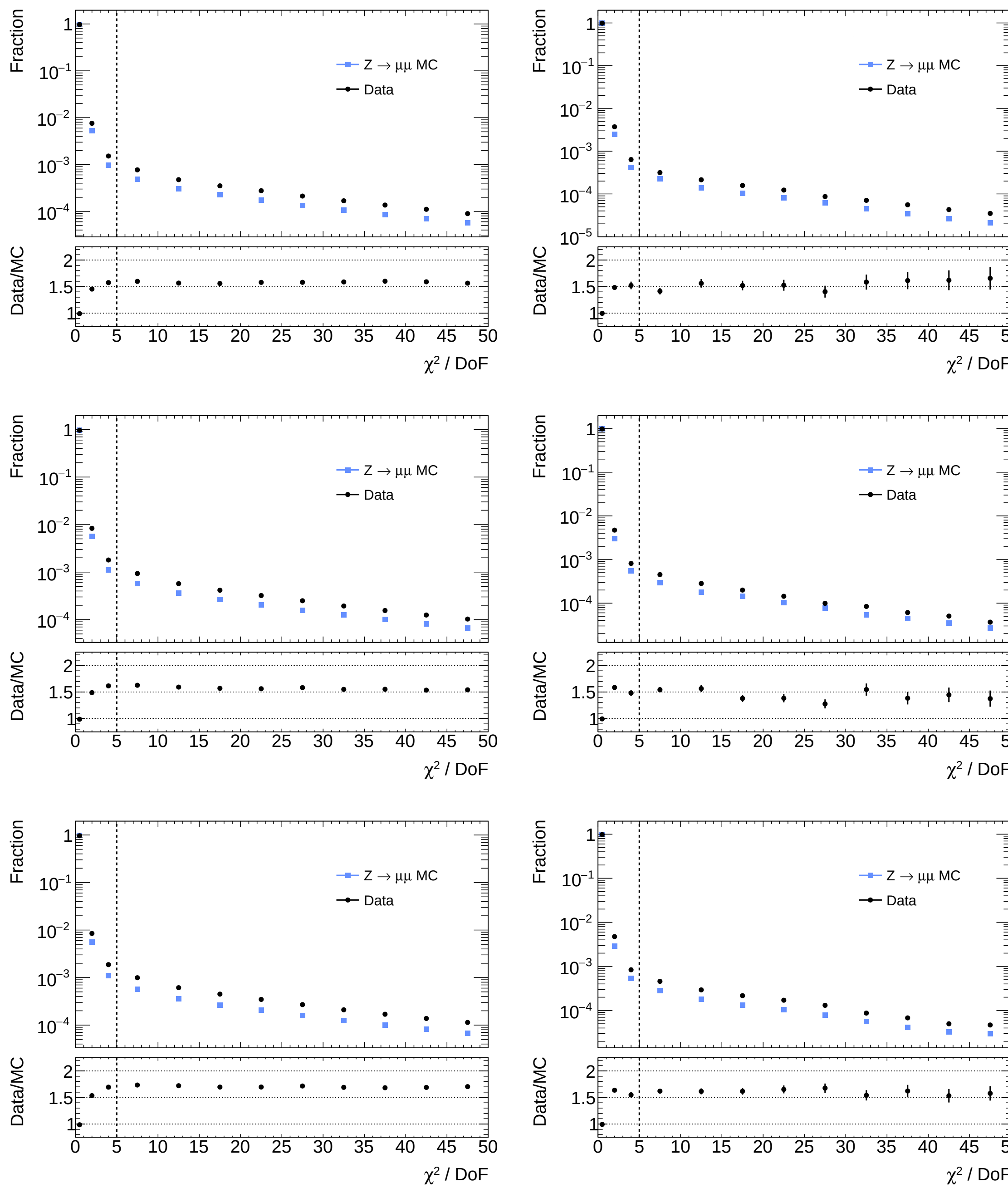

Figure 7.22: Goodness of the combined fit of the ID and MS tracks for probe muons that pass the modified `Loose` identification working point (left) and match the `HLT_mu60_0eta105_msonly` trigger (right) in the 2015/2016 data and mc16a (top), 2017 data and mc16d (middle), and 2018 data and mc16e (bottom). Only probes with $p_T > 60$ GeV are considered. Both distributions are normalized to unit area.

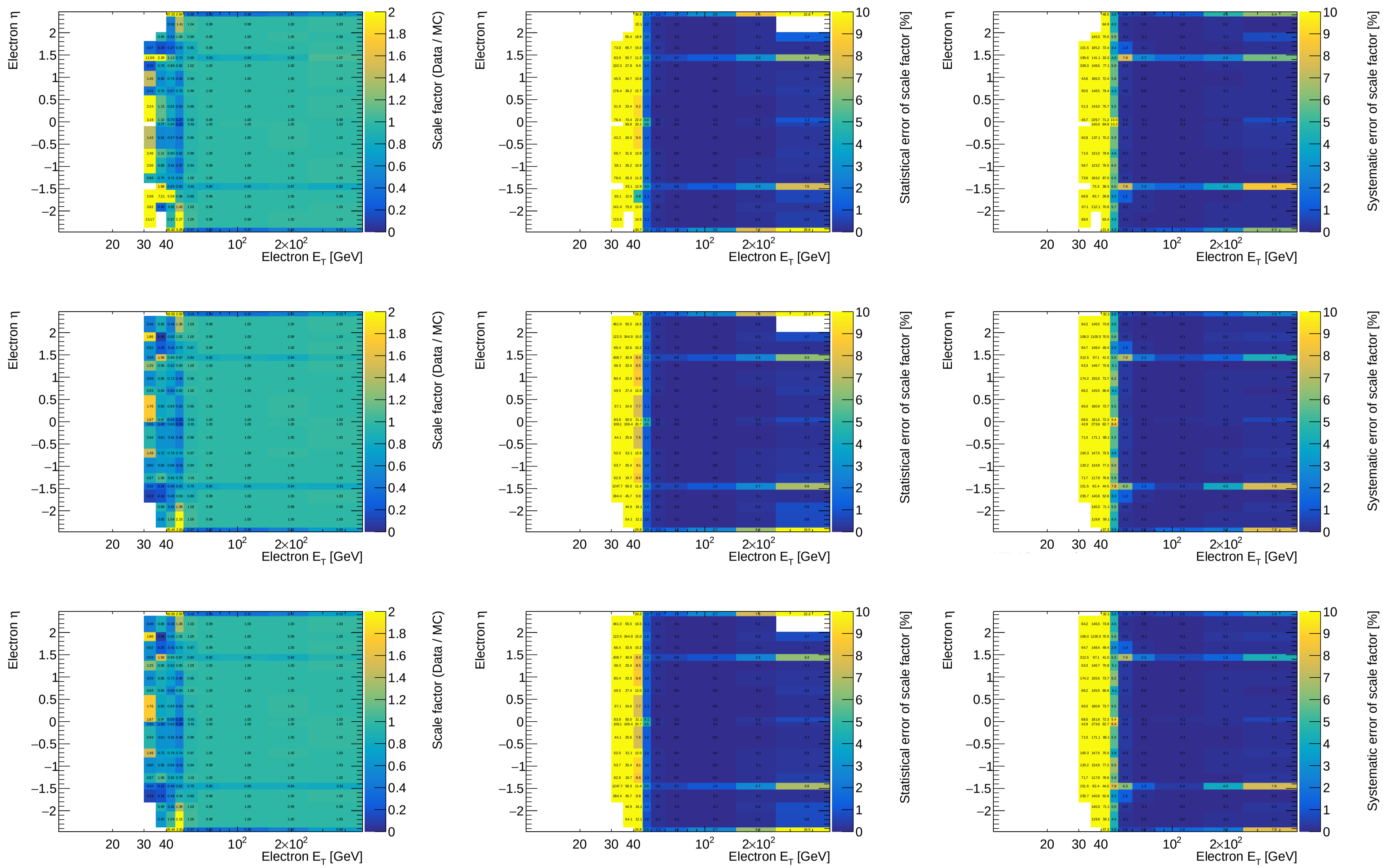

Figure 7.23: Scale factors (left) with their statistical (middle) and systematic (right) error for the `HLT_g50_loose` trigger as a function of the probe E_T and η extracted from a comparison of 2015/2016 data and mc16a (top), 2017 data and mc16d (middle), and 2018 data and mc16e (bottom).

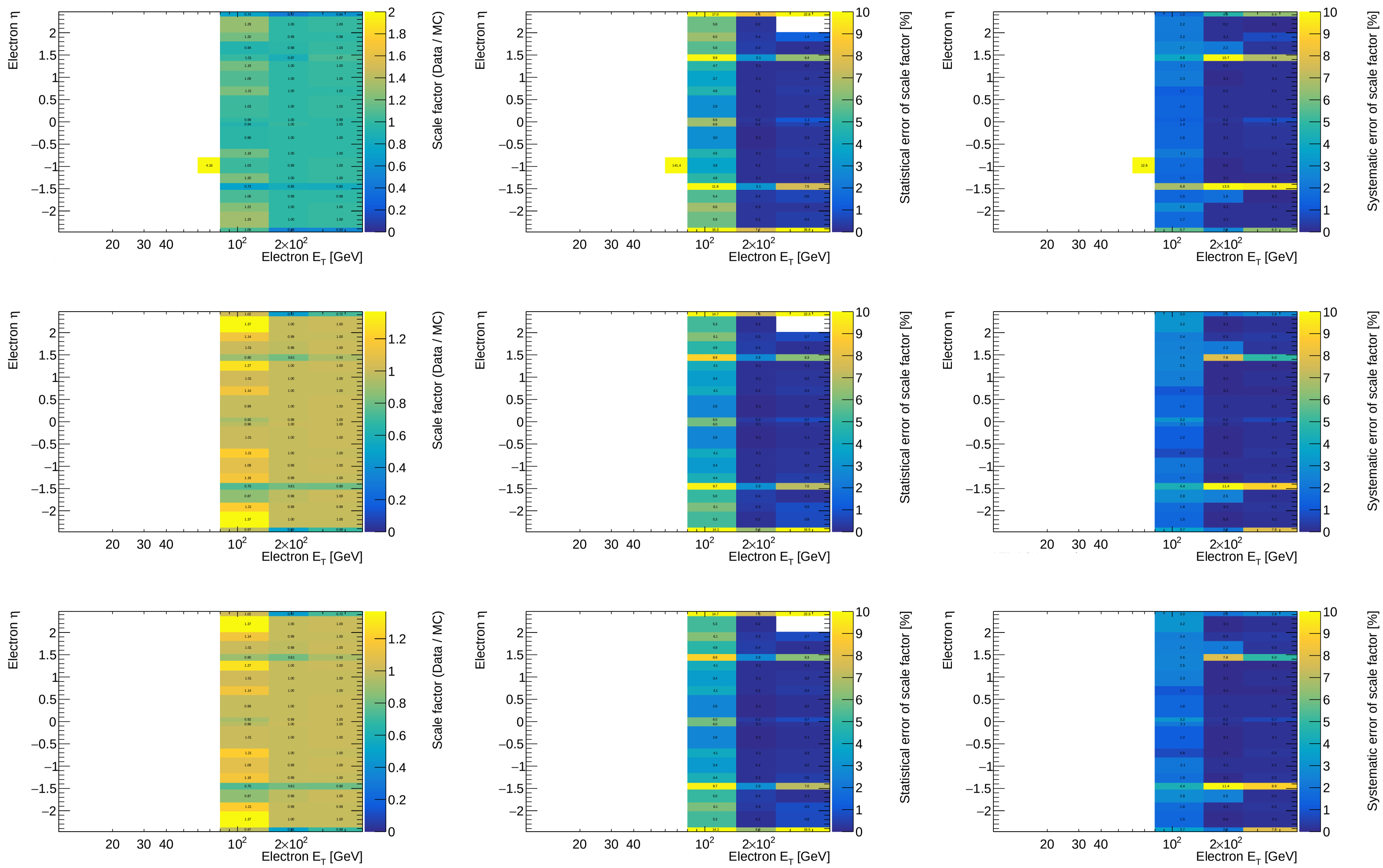

Figure 7.24: Scale factors (left) with their statistical (middle) and systematic (right) error for the `HLT_g140_loose` trigger as a function of the probe E_T and η extracted from a comparison of 2015/2016 data and mc16a (top), 2017 data and mc16d (middle), and 2018 data and mc16e (bottom).

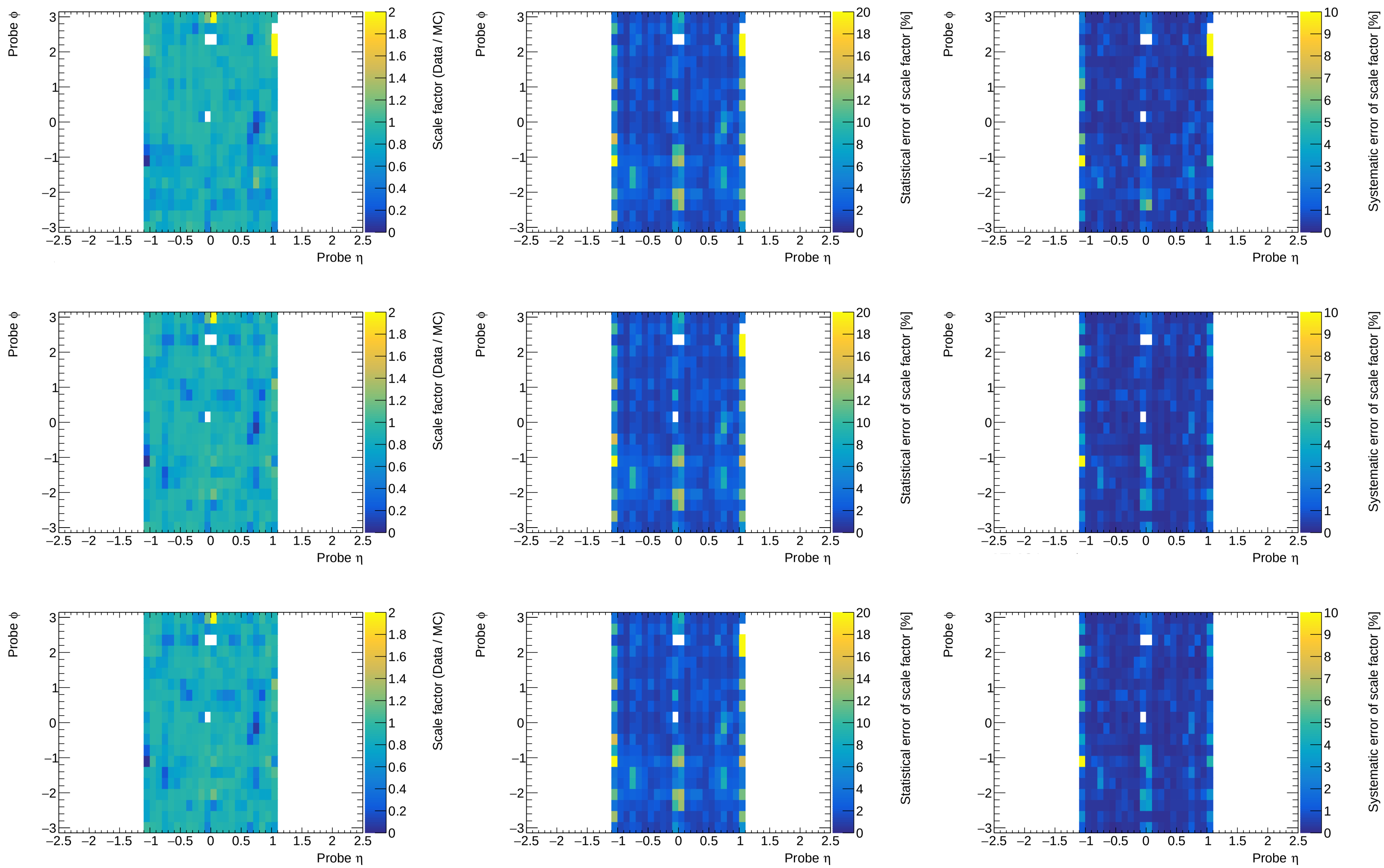

Figure 7.25: Scale factors (left) with their statistical (middle) and systematic (right) error for the `HLT_mu60_0eta105_msonly` trigger as a function of the probe η and ϕ extracted from a comparison of 2015/2016 data and mc16a (top), 2017 data and mc16d (middle), and 2018 data and mc16e (bottom). Only probes with $p_T > 60$ GeV are considered.

Table 7.10: Signal event and vertex level cuts.

K_S Vertex Selections
Opposite charge
470 MeV $< m_{\pi\pi} <$ 530 MeV
$\|\Delta z_0\| < 2$ mm
Decay length $>$ 15 mm

7.3.5 Large Radius Tracking and Secondary Vertexing

The dominant nonstandard systematic uncertainty for this analysis is the one attributed to the differences between data and MC in performance of the LRT and VSI algorithms of Sections 5.1.2 and 5.1.4. The decays $K_S \to \pi^+\pi^-$ provide a long-lived particle to use in the systematic error estimate as its 26.8 mm decay length ($c\tau$) is in the range of interest for this analysis. However, K_S kinematics do not resemble those of the signal LLPs and, therefore, are not an ideal sample for studying the LRT/VSI systematic error. Unfortunately this is the only sample that covers the decay length of interest with adequate statistics and hence is used to estimate the systematic error for two-track DVs. The standard tracking uncertainty, $\gtrsim 1.7\%$ [98], is well understood, as reported by the Tracking CP group. This analysis uses the same dilepton filtered $t\bar{t}$ samples as Section 7.2.2 and uses the difference in K_S yields between data and MC as an estimate of the systematic uncertainty and adds it in quadrature to this standard tracking uncertainty. Due to the long-lived nature of the K_S, the pion tracks can be reconstructed using either the ST or LRT algorithms and, thus can form vertices consisting of two STs, two LRTs, or one ST and one LRT. For this reason, the systematic error is estimated for each of the three track type combinations. As a conservative measure, deviations from the data in the ST/ST vertices predicted by MC are also included in the systematic estimation, since the standard uncertainty assigned for single tracks did not include the VSI algorithm used in reconstructing DVs.

Unfortunately, K_S tracks have relatively low p_T and the MC statistics are limited and, hence, the signal triggers and event filters cannot be imposed. The vertex-specific selections detailed in Section 7.1.1 are applicable, but the lepton-specific selections detailed in Section 7.1.2 are either ignored or modified and new cuts are added as motivated by literature [99]. The cuts applied to reconstructed K_S DVs are summarized in Table 7.10.

Comparing K_S yields between MC and data as a function of different kinematics revealed that MC underestimates the yield at low p_T, R_{xy}, and ℓ, but overestimates the yield at high values due to a known mismodeling in the K_S p_T distribution. The ST/ST K_S p_T spectrum is, therefore, adjusted to reproduce the data after sideband subtraction (380-440 and 560-620 MeV), assuming a linear background near the K_S mass peak. The same adjustment (scale factor binned in p_T) is then applied to the ST/LRT and LRT/LRT samples since the results of the ST/ST can be considered from a well understood region. An example of this p_T rescaling is given in Figure 7.26

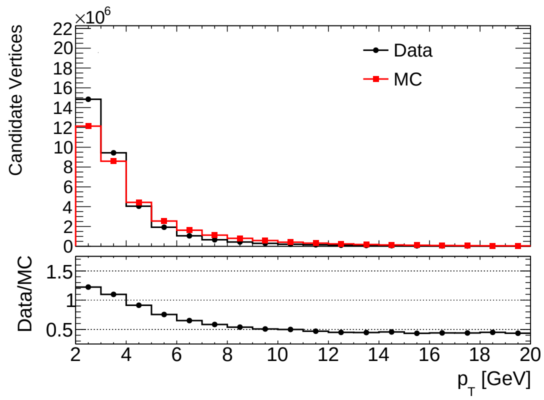

Figure 7.26: Reconstructed K_S yields before (left) and after (right) p_T scaling for mc16a/d/e $t\bar{t}$ and combined full Run II data as a function of p_T.

Figure 7.27 shows the good agreement in the mass, p_T, and z spectra between K_S (all vertex types combined) in the combined MC periods and full Run II data. Differences in the pileup distributions are as expected and differences in the ℓ spectrum are correlated with the differences in the R_{xy} spectrum. The residual discrepancy as a function of R_{xy} is attributed to the systematic error in LRT/VSI where, different trends are seen in each MC period, so the systematic uncertainties are estimated separately. The K_S yield in MC is normalized to the data when comparing the trends of the kinematics, where the ST/ST, ST/LRT, and LRT/LRT K_S distributions are individually normalized to estimate the systematic errors.

The K_S radial distribution is rebinned to loosely align with the tracking layers, as noted. In each bin, sideband subtractions are performed and the distributions are normalized independently for each vertex type. Figure 7.28 presents the scale factors used for each vertex type and in each MC period, binned in R_{xy}. The scale factor is extracted by fitting the ratio of the five larger radial bins to a linear function. The fitted line is then extrapolated into the three lower radial bins and compared with calculated scale factors if there is a K_S signal. For the ST/ST vertices, the three calculated scale factors are consistent with the fitted line. For the ST/LRT vertices, there is a K_S signal in the third bin, but the scale factor is higher than the linear parameterization by $\sim$20%. For the LRT/LRT vertices, there is no K_S signal in the first three bins. These consistency checks indicate that a linear function is a reasonable description of the dependence of the scale factor on R_{xy}. The scale factor typically varies between $\sim$0.8 and $\sim$1.2, but can be significantly larger in small R_{xy}

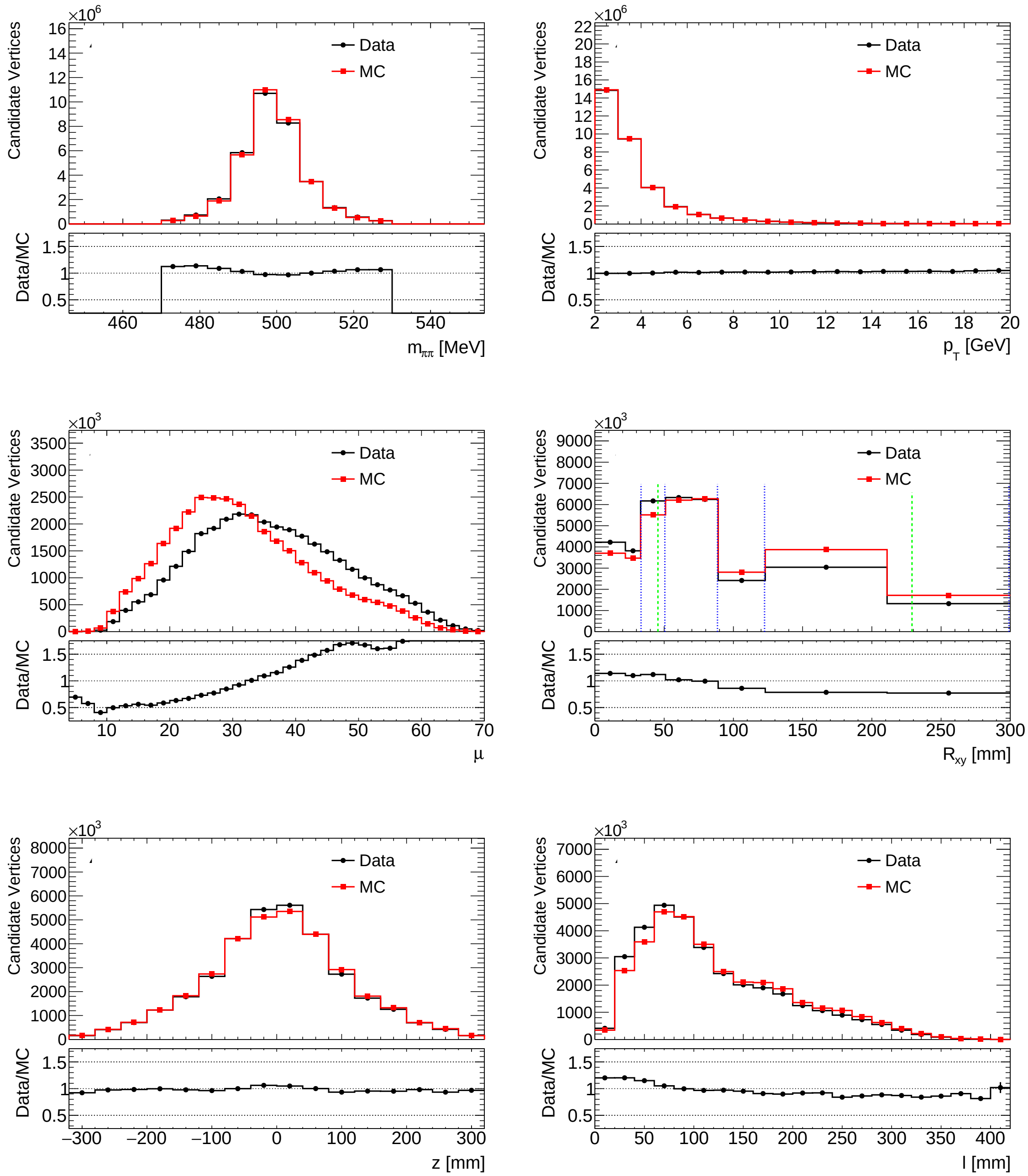

Figure 7.27: Reconstructed K_S yields after p_T scaling for mc16a/d/e $t\bar{t}$ and combined full Run II data for $\pi\pi$ invariant mass (top left), p_T (top right), pileup (middle left), R_{xy} (middle right), z (bottom left), and ℓ (bottom right). For the radial distribution, the blue dashed lines indicate the four Pixel layers and the first layer of SCT. The green dotted lines indicate the Inner Support Tube (45.5 mm) and Pixel Support Tube (229 mm).

Table 7.11: Uncertainties on signal efficiencies for the Z' model.

	Relative Signal Efficiency Uncertainty [%]		
Uncertainty Source	ee	$e\mu$	$\mu\mu$
Statistical	0-0.2	0-0.2	0-0.2
MC Modeling	6	6	6
Pileup Reweighting	1.5-4.0	1.6-3.5	1.6-3.6
Lepton Identification	0	0	0
Triggers	0.1-0.3	0.4-1.4	1.1-1.5
LRT and VSI	37.6-45.4	32.9-42.9	31.5-46.0

for ST/LRT and LRT/LRT DVs, which have limited statistics. However, the large scale factor has limited impact because the region is dominated by ST/ST DVs, where the scale factors are much closer to 1.

Due to the separation of the K_S sample into three vertex categories and the value of the K_S lifetime, statistics in the first two bins of the ST/LRT and first three bins of the LRT/LRT vertex distributions are limited and the total error on the scale factor includes statistical errors from the extrapolation of the linear function into the low appropriate bins. Additional systematic errors are added to the statistical error of each bin where these systematic errors include the standard 1.7% from standard tracking and the error associated with the mismodeling of the vertex type distribution. The MC does not properly recreate the K_S candidate vertex distribution by vertex type where, specifically, the MC tends to underestimate the number of ST/ST vertices and overestimate the number of vertices containing LRT tracks. The nominal normalization for each vertex type is compared to the normalization used for all vertex types combined with the relative difference added as a systematic to the scale factor.

7.3.6 Uncertainties on Signal MC

After estimating the individual systematic uncertainties, each one can be propagated to the signal efficiency by applying alternative weights associated with varying each scale factor up or down by one sigma. The alternative signal efficiency is then compared to the nominal value and the difference is taken as the propagated systematic uncertainty with the total systematic uncertainty being the sum of all propagated systematic uncertainties added in quadrature. A summary of the propagated systematic uncertainties on the full Run II signal efficiencies is given in Table 7.11. The systematic error associated with the DV reconstruction is the dominant source of uncertainty in all cases.

An example of the systematic errors extrapolated over decay length ($c\tau$) using the one of the Z' mc16a signal samples used in Figure 7.8 is shown in Figure 7.29. It is evident

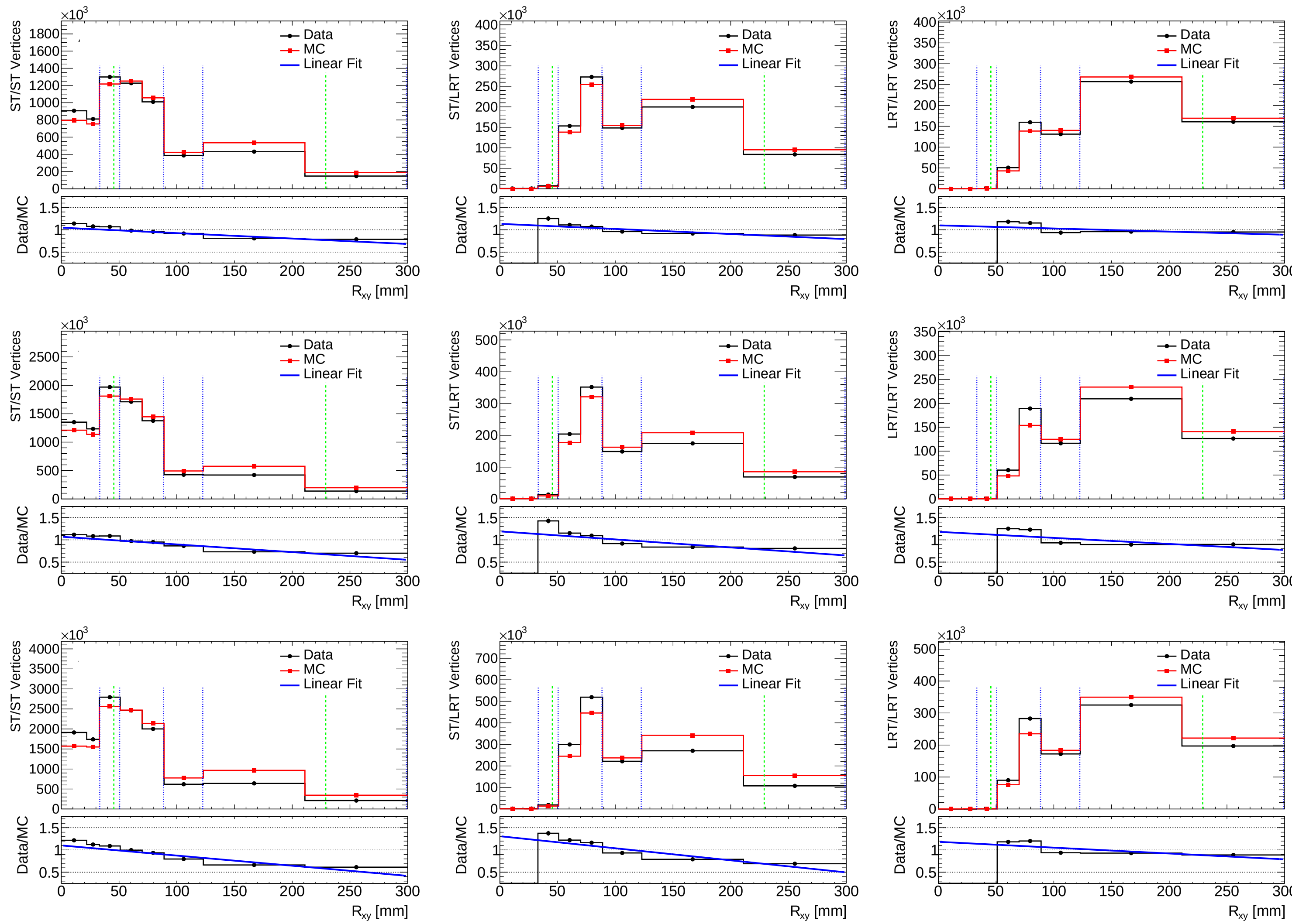

Figure 7.28: Reconstructed K_S yields as a function of R_{xy} for 2015/2016 data and mc16a (top), 2017 data and mc16d (middle), and 2018 data and mc16e (bottom) with the three different vertex types, ST/ST (left), ST/LRT (middle), and LRT/LRT (right). The line shows the linear fit to the scale factor. Only statistical errors are shown. The green dotted lines indicate the Inner Support Tube (45.5 mm) and Pixel Support Tube (229 mm).

from these examples that, for all models and at all lifetimes, the LRT/VSI systematic error dominates the overall systematic error.

7.3.7 Uncertainties on Background Estimates

The systematic uncertainty on the cosmic ray muon background, as described in Section 7.2.1, is estimated by varying the binning in $\Delta R_{\cos}$, the start value for the exponential fit, and the fit function itself. Each of the variations resulted in a difference from the nominal estimate of several orders of magnitude smaller than the statistical error from the optimized fit and, as such, no systematic uncertainty is added to the estimate. The systematic uncertainty on the random crossing background, as described in Section 7.2.2, is assumed to be the 5.6% discrepancy between the predicted and observed number of DVs in the track-track channel of 2016 data.

7.4 Results

7.4.1 Signal Region Results in Data

The full Run II dataset results are shown for the signal regions in Figure 7.30. Unlike the signal MC signal samples, the data are preselected and filtered following the prescriptions in Section 6.3. The observation of two signal events is inconsistent with the full Run II background estimate in the $e\mu$ channel. The single event in the $\mu\mu$ channel is not consistent with the corresponding background estimate in that region. Thus, there must either be an explanation for the three observed events as unaccounted background or they are truly signal BSM events. The following analysis of the observed signal region events in data and extracted limits are made with the caveat that, at the time of this dissertation's publication, the treatment of the events is an ongoing debate among experts in the ATLAS experiment and the following prescriptions are the recommendation of this analysis as a result of preliminary investigation of the events.

The recommendations for treatment of the three observed signal events in data are as follows. Unfortunately, the two events in the $e\mu$ signal region are actually cosmic ray muons where one of the two high-p_T muons shared a high-p_T ID track with a reconstructed low-p_T electron. In each case, one muon fails the modified signal identification criteria and, therefore, an electron is kept during overlap removal and the vertex is considered in the $e\mu$ region rather than the $\mu\mu$ region. The details of the two cases are as follows:

- Case 1: An ID track with p_T of 554 GeV is reconstructed as an electron with p_T of 4.1 GeV while a muon of p_T of 1614 GeV fails overlap removal and quality criteria. The $\Delta R_{\cos}$ is 0.0007 for the signal $e\mu$ pair and 0.0016 if the muon passed lepton selection.

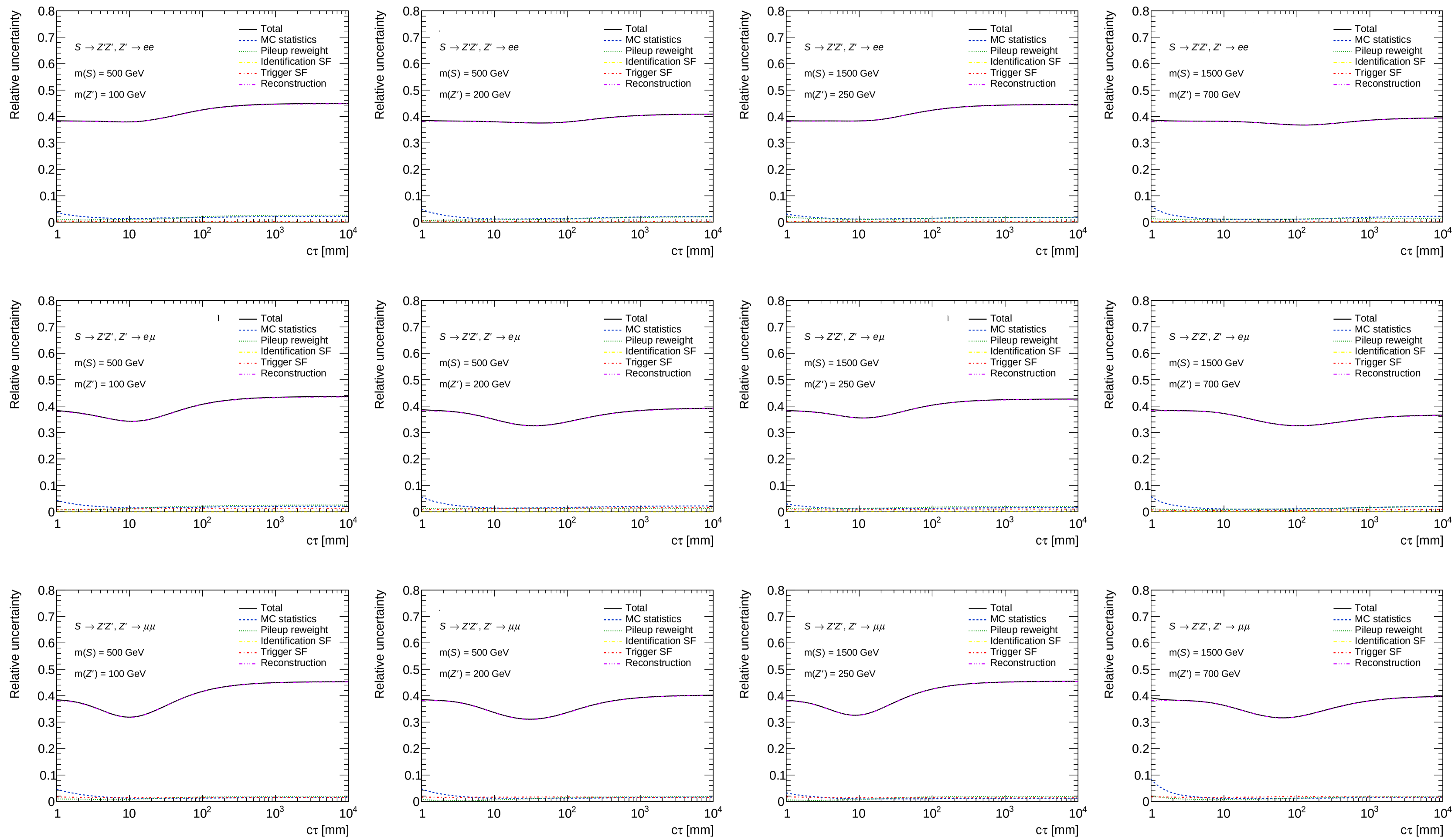

Figure 7.29: Vertex-level systematic errors as a function of decay length ($c\tau$) for a set of Z' signal mc16a samples with a scalar mass of 500 or 1500 GeV and Z' mass of 100, 200, 250, or 700 GeV with Z' decaying to ee (top), $e\mu$ (middle), and $\mu\mu$ (bottom) final states.

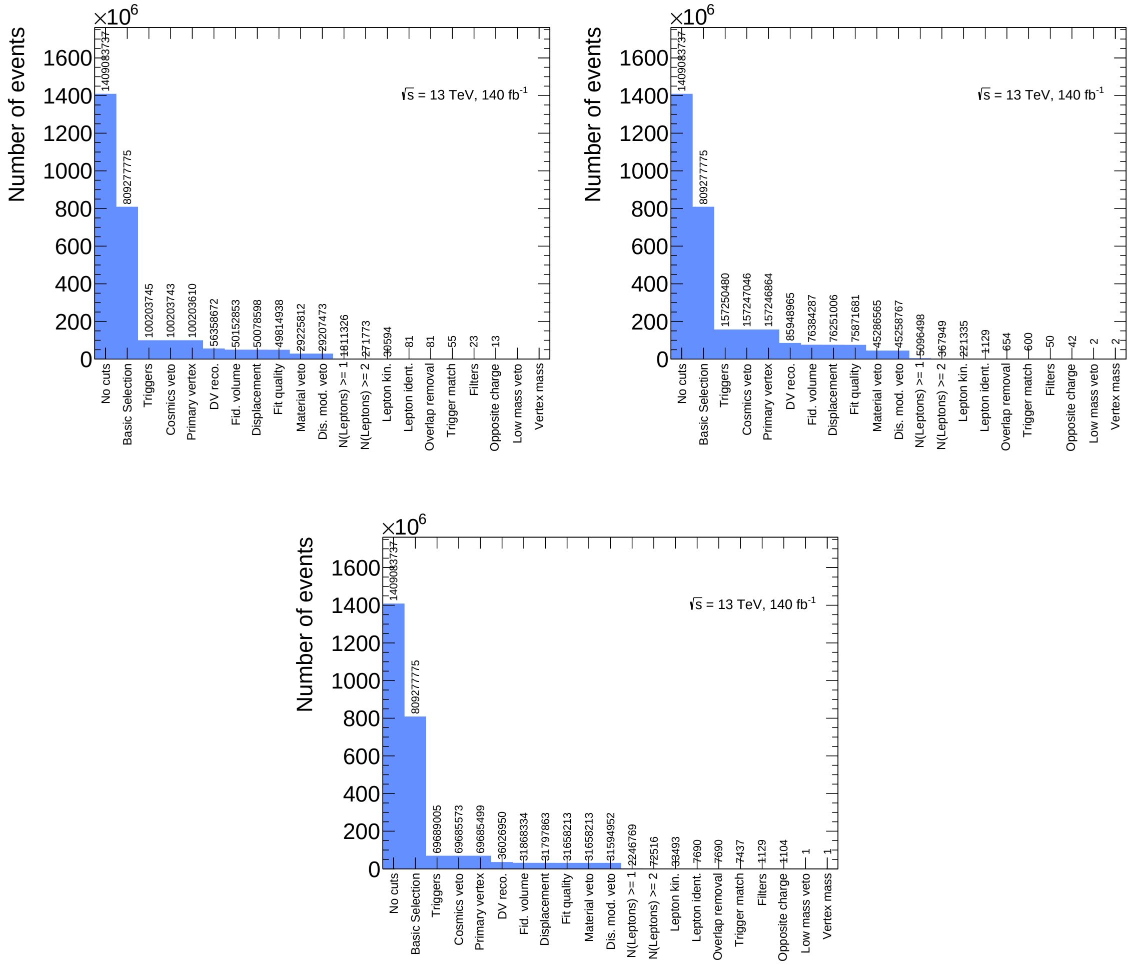

Figure 7.30: Event-level signal cutflows for full Run II data. Note that all three signal events come from the 2017 data.

These values are significantly below the cosmic veto of 0.01 and hence the event is a classic example of a cosmic ray.

- Case 2: An ID track with p_T of 109 GeV is reconstructed as an electron with p_T of 4 GeV while a muon of p_T of 105 GeV fails overlap removal and quality criteria. The $\Delta R_{\cos}$ is 0.0023 for the signal $e\mu$ pair and 0.0004 if the muon passed lepton selection. These values are significantly below the cosmic veto of 0.01 and hence the event is another classic example of a cosmic ray.

This motivates the tightening of the cosmic veto to include all DVs formed by two muons as well as the consideration of any $e\mu$ DVs to allow for the misreconstruction of a muon as an electron. Tightening the cosmic veto would not introduce any significant systematic error as it removes a small fraction of the signal ($\lesssim 1\%$). The tightened cosmic veto was applied for the signal samples and removes the two observed events in data. The resulting upper limits are presented in Section 7.4.3.

In the case of the $\mu\mu$ event, one would expect both tracks to pass the pre-selection criteria for secondary vertexing in Table 5.3. However, only one of the tracks satisfy the criteria due to the implementation of the pre-selection requirements are applied. When forming two-track vertex seeds, only one of the tracks is required to pass the minimum d_0 cut. As such, one of the two muons in the DV has a $d_0 < 2$ mm while the other has larger d_0. The track for the the lower d_0 muon has a large χ^2/n_{dof} as a `Combined` muon ($\sim 1100/41$). There is also a third ID track highly collimated with the larger d_0 muon which is not vertexed with the nearby muon and is not added to the $\mu\mu$ DV due to its impact on the vertex fit. These preliminary results suggest that the DV may actually be a muon-track or multi-track DV rather than a $\mu\mu$ DV and is likely a result of poor muon reconstruction. Introducing some fit quality cut on the muons that are not associated with the signal filters could, in the future, remove this background. As such, an upper limit (UL) on the cross section times branching ratio ($\sigma \times$ BR) can be set for each scalar and Z' mass point and each Z' decay mode following Equation 4.2 and using the following statistical procedure.

7.4.2 Statistical Methods

The ULs are set using *HistFitter v1.1.0* [100], the dedicated ATLAS tool for limit setting using a modified Frequentist method. Let $n_{\text{pred}} = \mu \cdot s + b$ be the number of predicted events, with the number of signal events, s, number of background events, b, and signal strength μ. Here, $\mu = 0$ represents the background only hypothesis and $\mu = 1$ represents the nominal signal plus background hypothesis. Then, the number of observed events, n_{obs}, has its PDF modeled by a Poisson distribution with mean $\lambda = n_{\text{pred}} = \mu \cdot s + b$ where this PDF is also known as a likelihood function, $L(\mu) = \text{Pois}(n|\mu)$. To account for the systematic uncertainties from Section 7.3, variables known as nuisance parameters are introduced, making s and b functions of the respective uncertainties. These nuisance parameters are assumed to have PDFs modeled by Gaussian distributions such that the full likelihood function for n_{obs} is:

$$L(\mu, \theta) = \text{Pois}(n_{\text{obs}}|n_{\text{pred}}) \cdot \text{Gaus}(\Theta_s|\theta_s, \sigma_s) \cdot \text{Gaus}(\Theta_b|\theta_b, \sigma_b) \tag{7.12}$$

for global observables, Θ_s and Θ_b corresponding to nuisance parameters, θ_s and θ_b, with uncertainties, σ_s and σ_b, for signal and background yields, respectively [101, 102].

The agreement between the signal hypothesis with a given μ and observation in the data is determined with a hypothesis test using the one-sided profile likelihood ratio test statistic:

$$q_\mu = \begin{cases} -2\ln\lambda(\mu) & \hat{\mu} \le \mu \\ 0 & \hat{\mu} > \mu, \end{cases} \tag{7.13}$$

for the profile likelihood ratio $\lambda(\mu) = \frac{L(\mu,\hat{\hat{\theta}})}{L(\hat{\mu},\hat{\theta})}$ [103]. The maximum likelihood estimates, $\hat{\mu}$ and $\hat{\theta}$, are the parameters that globally maximize the likelihood function while $\hat{\hat{\theta}}$ is a conditional maximum likelihood estimate which maximizes the likelihood function for the given μ [101, 102].

The PDFs cannot be calculated directly using the asymptotic approach [103] due to the low background of the analysis. Instead, the PDFs for q_μ can then be estimated by performing thousands of pseudo-experiments sampling values of n_{obs} and Θ from Equation 7.12 to calculate the value of q_μ for a given μ and θ. The p-value of the test statistic then determines compatibility of the signal hypothesis with the data observation where:

$$p_\mu = P(q_\mu \ge q_\mu^{\text{obs}}|\mu,\theta) = \int_{q_\mu^{\text{obs}}}^{\infty} f(q_\mu,\theta)dq_\mu \tag{7.14}$$

for the probability density function, $f(q_\mu,\theta)$. This p-value also represents the probability that a given value of q_μ is at least as incompatible with the signal hypothesis as the data observation with q_μ^{obs}. Equation 7.14 depends, however, on θ, where different θ can give a variety of p_μ when the maximum value is desired. Thus, $\hat{\hat{\theta}}_\mu^{\text{obs}}$ is used to estimate the maximum p_μ in a process known as profiling.

For a desired confidence level (CL), typically 95%, the frequentist approach is to then solve for the value of q_μ for which Equation 7.14 is equal to $1 - \text{CL}$. Using this nomenclature, CL_{s+b} represents the nominal signal plus background scenario where $\mu = 1$ and CL_b represents the background only scenario where $\mu = 0$. The modified frequentist approach adopted by the LHC defines the signal CL, CL_s, as:

$$\text{CL}_s = \frac{1-\text{CL}_{s+b}}{1-\text{CL}_b} = \frac{p_\mu}{p_{\mu=0}} = \frac{p_\mu}{1-p_b}, \tag{7.15}$$

for $p_b = 1 - P(q_0 \ge q_0^{\text{obs}}|0,\hat{\hat{\theta}}_0^{\text{obs}})$ following Equation 7.14 [104]. This definition conveniently avoids setting any exclusion limits on models with no sensitivity that could generate arbitrarily small p-values in scenarios where the background prediction can be much higher than n_{obs}[6].

Finally, using Equation 7.4 and the signal efficiency, ϵ, limits are set on $\sigma \times \text{BR}$ using the relation:

$$n_{\text{obs}} = \mathcal{L}_{int.} \times \sigma \times \text{BR} \times \epsilon = \mu \cdot\ s + b. \tag{7.16}$$

[6] n_{obs} being smaller than b can lead to small p_μ, excluding a model without adequate justification. Equation 7.15, instead, allows for this case which leads to large p_b and, thus, large CL_s.

Similarly, expected limits can be estimated by using pseudo-data assuming the PDF for the background only hypothesis, $\mu = 0$, is true and taking the median value of μ after performing several pseudo-experiments.

7.4.3 Upper Limits

Using the prescription from Section 7.4.2, background estimate from Section 7.2.3, systematic uncertainties from Section 7.3, and the observed number of events listed in Section 7.4.1, the expected and observed ULs at 95% CL on $\sigma \times$ BR are calculated separately for each decay channel and extrapolated as a function of decay length, $c\tau$, using the same lifetime reweighting procedure as in Section 7.1.3. Naturally, points along $c\tau$ where the signal efficiency is highest are also the regions where the most stringent limits can be set following Equation 7.16. The limits on the Z' production cross-section times branching fraction as a function of decay length are shown in Figures 7.31, 7.32, and 7.33 for each channel. The single observed $\mu\mu$ event results in the observed limits for that decay mode being $\sim 2\sigma$ above the expected limit, but does not constitute a signal discovery. Rather, the result is that the limits for this decay mode are less aggressive than the expected limits. For the ee and $e\mu$ channels, the observed limits nearly overlap with the expected limits in all cases due to the zero observed events in each channel following the introduction of the $e\mu$ cosmic veto. Only the specific bench mark models where the scalar mass is 500 GeV can exclude some parameters in each channel due to their relatively large cross sections, $\sim O(0.1)$ fb. These models are excluded for decay lengths $\sim 1 - 100$ mm. Cross section limits for neutral resonances decaying to a high-mass oppositely charged pair of leptons range from ∼0.1 to 20 fb varying slightly across scalar and Z' mass points of the benchmark model.

Model-independent limits can also be set on the visible cross section, $\epsilon\sigma$, by considering the background-only scenario. Table 7.12 summarizes the model-independent limits for each of the decay channels in order of the number of observed events in the data. For the ee and $e\mu$ channels, signal models that predict at least ∼3 events are excluded at the 95% confidence level. For $\mu\mu$ channel, the observed event in the signal region does not constitute a statistically significant observation especially given the unaccounted background sources of the events and signal models that predict at least ∼4 events are excluded at the 95% confidence level.

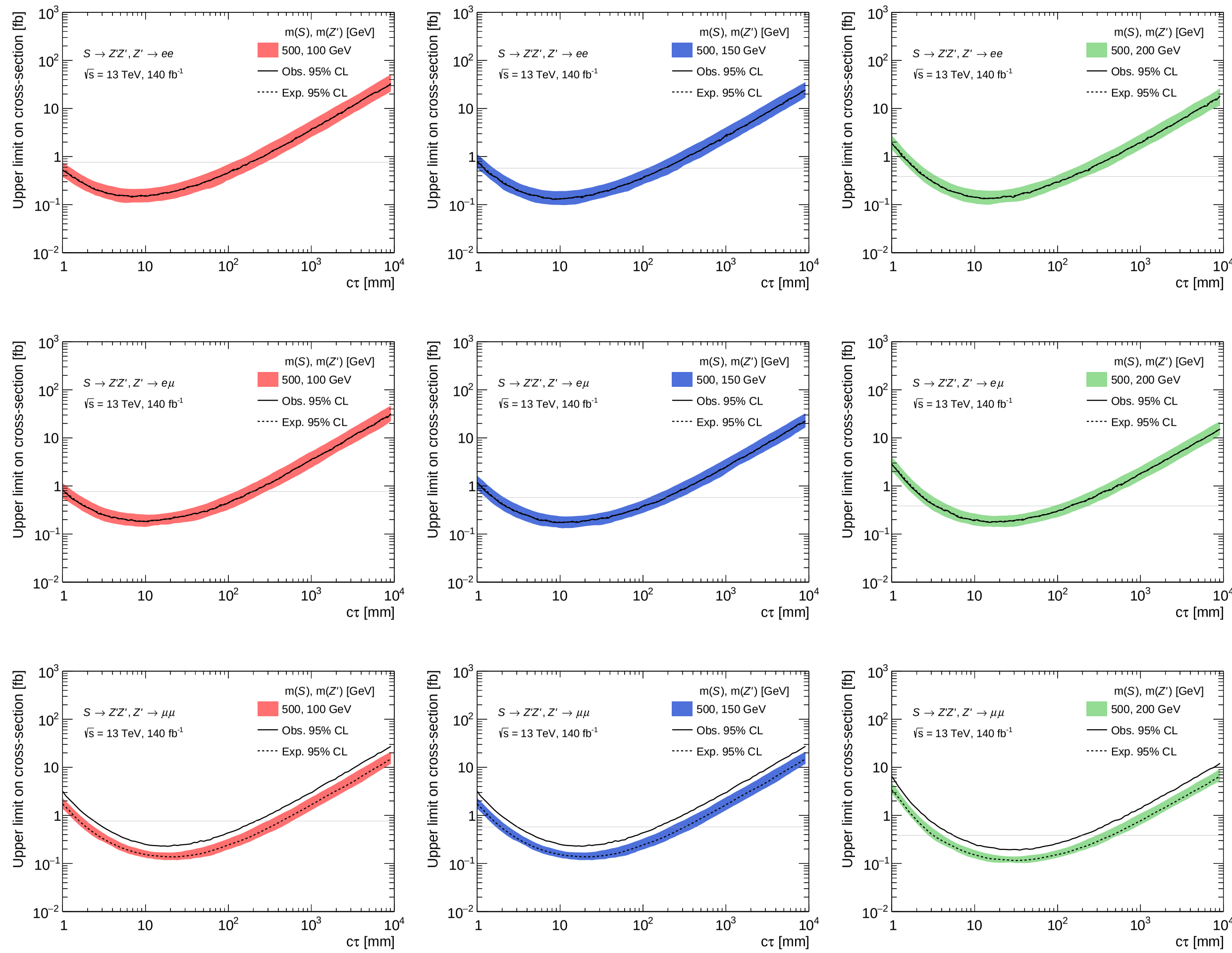

Figure 7.31: Observed limits on cross section as a function of decay length ($c\tau$) for a scalar mass of 500 GeV and Z' mass of 100 (left), 150 (middle), or 200 GeV (right) decaying to ee (top), $e\mu$ (middle), and $\mu\mu$ (bottom) final states. The colored bands represent the total uncertainties.

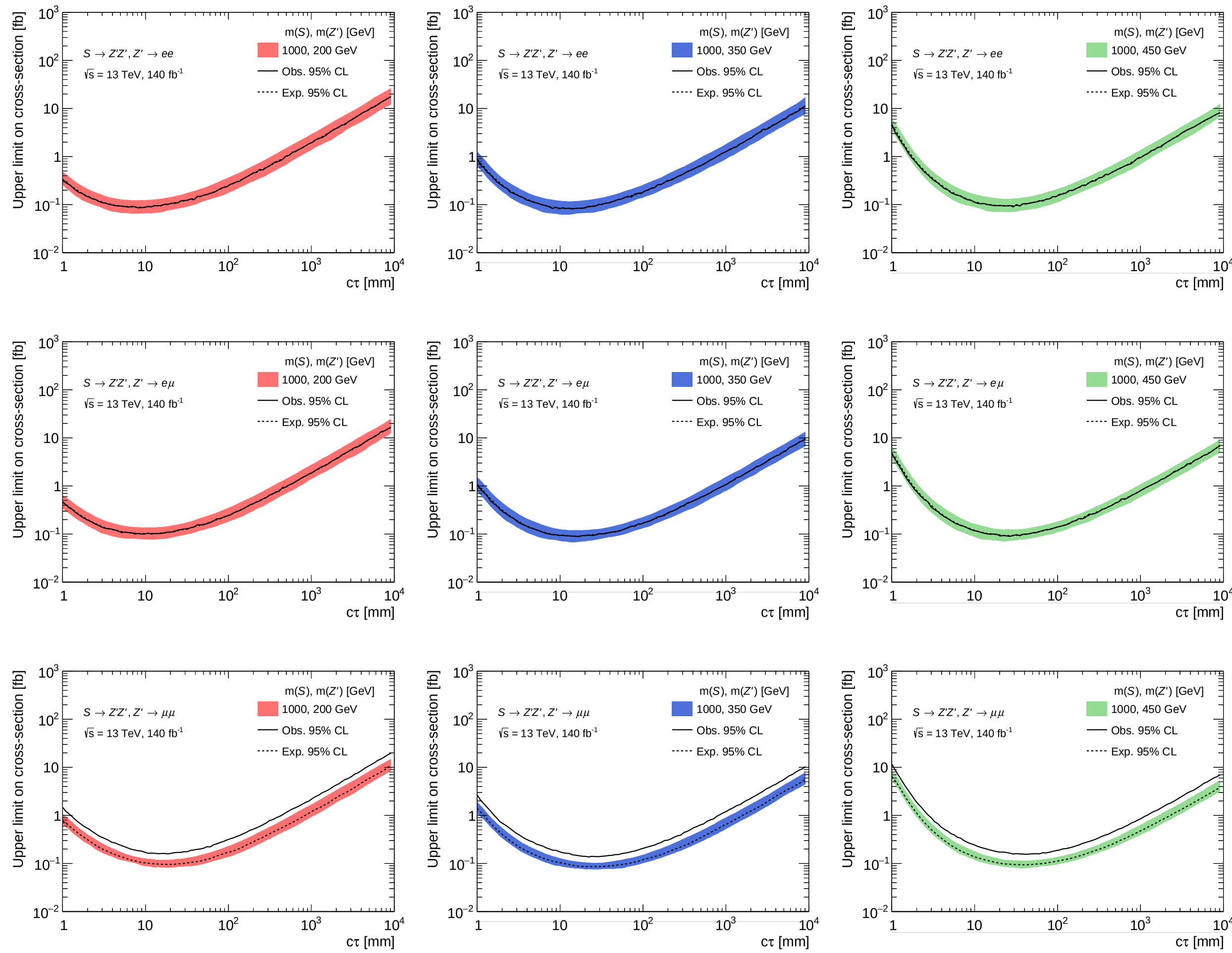

Figure 7.32: Observed limits on cross section as a function of decay length ($c\tau$) for a scalar mass of 1000 GeV and Z' mass of 200 (left), 350 (middle), or 450 GeV (right) decaying to ee (top), $e\mu$ (middle), and $\mu\mu$ (bottom) final states. The colored bands represent the total uncertainties.

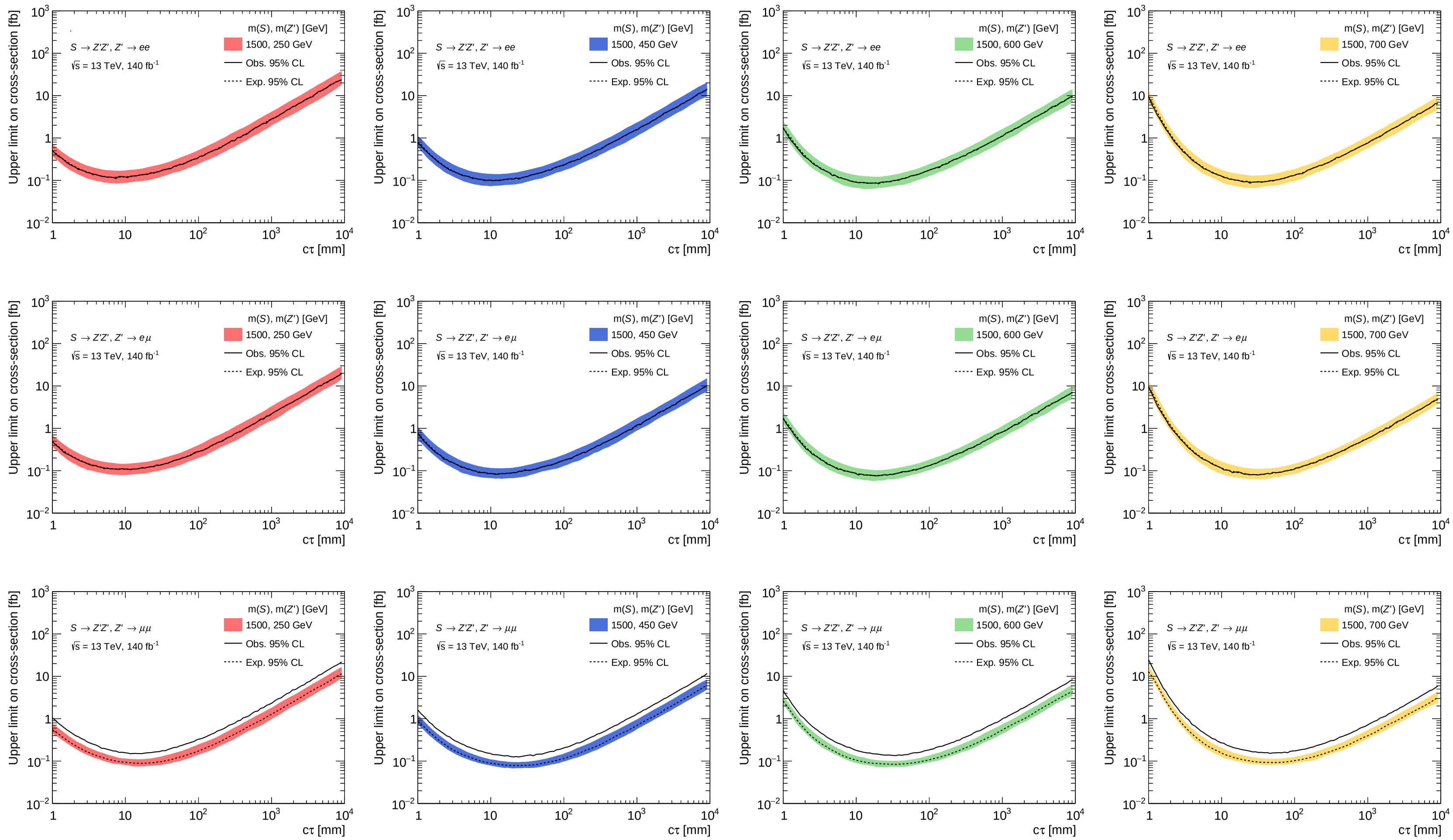

Figure 7.33: Observed limits on cross section as a function of decay length ($c\tau$) for a scalar mass of 1500 GeV and Z' mass of 250 (left), 450 (left middle), 600 (right middle), or 700 GeV (right) decaying to ee (top), $e\mu$ (middle), and $\mu\mu$ (bottom) final states. The colored bands represent the total uncertainties.

Signal channel	$\langle\epsilon\sigma\rangle^{95}_{\rm obs}$[fb]	$S^{95}_{\rm obs}$	$S^{95}_{\rm exp}$	$p(s=0)$ (Z)
ee (0 events)	0.02	3.1	$2.8^{+0.2}_{-0.1}$	0.27 (0.60)
$e\mu$ (0 events)	0.02	3.0	$1.1^{+0.0}_{-0.4}$	0.02 (2.08)
$\mu\mu$ (1 event)	0.03	3.8	$3.5^{+0.3}_{-1.4}$	0.01 (2.30)

Table 7.12: 95% CL upper limits on the visible cross section, $\langle\epsilon\sigma\rangle^{95}_{\rm obs}$, number of signal events, $S^{95}_{\rm obs}$, and number of signal events, $S^{95}_{\rm exp}$, given the expected number (and $\pm1\sigma$ excursions on the expectation) of background. The probability for observing the number of events assuming no signal is presented.

Chapter 8
Summary

In this thesis, a search for new BSM long-lived neutral particles decaying to $\mu\mu$, ee, or $e\mu$ pairs in the ATLAS detector at the LHC is presented. The search uses the full 140 fb^{-1} of Run II dataset collected in pp collisions at $\sqrt{s} = 13$ TeV at the ATLAS experiment between 2015 and 2018. The lepton pairs must form a common vertex in the ID volume of the detector and have a dilepton mass of at least 12 GeV, strongly suppressing SM background sources. Dedicated algorithms to reconstruct highly-displaced tracks and vertices greatly improve the search sensitivity while high p_T triggers and filters reduce CPU processing time and suppress contributions from material interactions and conversions.

Three events were observed in the signal regions of the full Run II data. The agreed upon source and treatment of these three events is an ongoing investigation by experts at the ATLAS experiment at the time of publication, but this analysis has produced preliminary prescriptions. The two $e\mu$ events are likely poorly reconstructed cosmic ray muons where one muon is misreconstructed as a low p_T electron due to it failing the modified identification criteria. These two events can be removed by imposing the cosmic veto, $\Delta R_{\cos} > 0.01$, on $e\mu$ DVs. The $\mu\mu$ event is likely a combination of effects in the custom secondary vertexing algorithm and muon reconstruction where a poorly associated muon track is used to form a $\mu\mu$ DV. This event is not consistent with the background estimate of 0.0245 ± 0.0410 for the channel and is considered an unaccounted for background source that may need an alternative estimation technique in the future. The $\mu\mu$ event could also be potentially removed with a future cut on the global χ^2/n_{dof} of the combined MS and ID tracks following a dedicated study on the relevant signal muons, but this study is beyond the scope of this analysis. It is possible that, by the time of publication, this event is removed by an additional cut after further investigation.

Following the preliminary recommendations of this analysis, the $e\mu$ cosmic veto is applied to signal samples and removes the two observed events in data and the upper limits are derived on the $\sigma \times$ BR at the 95% CL. Limits on the cross section for neutral resonances decaying to oppositely charged lepton pairs vary from $\sim$0.1 to 20 fb with only small variations across the scalar and Z' mass points for the benchmark model. The limits are interpreted in the context of a benchmark model where a pair-produced Z' is the LLP but can be readily used to interpret other models with a heavy neutral resonance.

While no evidence of any signal was found in this search, improvements to the LRT [105] and VSI algorithms for Run III as well as the improvements to LHC provide promising enhancements to the sensitivity to this particular signal. New, dedicated displaced object triggers (electrons and muons, especially) for Run III also offer a promising avenue for improved sensitivity. Hopefully, analyses such as this and the many other full Run II and early Run III searches will lay the groundwork for the expanded search for physics beyond the SM in the combined effort to understand the many observed phenomena still unexplained by our current theories of the universe.

Bibliography

[1] ATLAS Collaboration, *Observation of a new particle in the search for the Standard Model Higgs boson with the ATLAS detector at the LHC*, Physics Letters B **716** (2012) 1, URL: https://doi.org/10.1016%2Fj.physletb.2012.08.020 (cit. on pp. 1, 2, 5, 11).

[2] CMS Collaboration, *Observation of a new boson at a mass of 125 GeV with the CMS experiment at the LHC*, Physics Letters B **716** (2012) 30, URL: https://doi.org/10.1016%2Fj.physletb.2012.08.021 (cit. on pp. 1, 2, 5, 11).

[3] M. Magg, Q. Shafi, and C. Wetterich, *Gauge hierarchy in presence of discrete symmetry*, Phys. Lett. B **87** (1979) 227, URL: https://cds.cern.ch/record/133340 (cit. on pp. 1, 6).

[4] M. Magg and C. Wetterich, *Neutrino mass problem and gauge hierarchy*, Phys. Lett. B **94** (1980) 61, URL: https://cds.cern.ch/record/133759 (cit. on pp. 1, 6).

[5] G. Bertone, D. Hooper, and J. Silk, *Particle dark matter: evidence, candidates and constraints*, Physics Reports **405** (2005) 279, URL: https://doi.org/10.1016%2Fj.physrep.2004.08.031 (cit. on pp. 1, 6).

[6] D. Clowe et al., *A Direct Empirical Proof of the Existence of Dark Matter**, The Astrophysical Journal **648** (2006) L109, URL: https://dx.doi.org/10.1086/508162 (cit. on pp. 1, 6).

[7] D. P. Adan, *Dark Matter searches at CMS and ATLAS*, (2023), arXiv: 2301.10141 [hep-ex] (cit. on p. 1).

[8] D. Toussaint, S. B. Treiman, F. Wilczek, and A. Zee, *Matter-antimatter accounting, thermodynamics, and black-hole radiation*, Phys. Rev. D **19** (4 1979) 1036, URL: https://link.aps.org/doi/10.1103/PhysRevD.19.1036 (cit. on pp. 1, 6).

[9] M. Dine and A. Kusenko, *Origin of the matter-antimatter asymmetry*, Rev. Mod. Phys. **76** (1 2003) 1, URL: https://link.aps.org/doi/10.1103/RevModPhys.76.1 (cit. on pp. 1, 6).

[10] C. Burgess and G. Moore, *The Standard Model: A Primer*, Cambridge University Press, 2006 (cit. on p. 2).

[11] A. Einstein, *Die Grundlage der allgemeinen Relativitätstheorie*, Annalen der Physik **354** (1916) 769, URL: https://onlinelibrary.wiley.com/doi/abs/10.1002/andp.19163540702 (cit. on p. 2).

[12] P. W. Higgs, *Broken Symmetries and the Masses of Gauge Bosons*, Phys. Rev. Lett. **13** (16 1964) 508, URL: https://link.aps.org/doi/10.1103/PhysRevLett.13.508 (cit. on p. 2).

[13] K. G. Wilson, *Confinement of quarks*, Phys. Rev. D **10** (8 1974) 2445, URL: https://link.aps.org/doi/10.1103/PhysRevD.10.2445 (cit. on p. 3).

[14] D. J. Gross and F. Wilczek, *Ultraviolet Behavior of Non-Abelian Gauge Theories*, Phys. Rev. Lett. **30** (26 1973) 1343, URL: https://link.aps.org/doi/10.1103/PhysRevLett.30.1343 (cit. on p. 3).

[15] H. D. Politzer, *Reliable Perturbative Results for Strong Interactions?*, Phys. Rev. Lett. **30** (26 1973) 1346, URL: https://link.aps.org/doi/10.1103/PhysRevLett.30.1346 (cit. on p. 3).

[16] M. Drewes, *The Phenomenology of Right Handed Neutrinos*, International Journal of Modern Physics E **22** (2013) 1330019, URL: https://doi.org/10.1142%2Fs0218301313300191 (cit. on p. 4).

[17] V. A. Kostelecký, *Gravity, Lorentz violation, and the standard model*, Phys. Rev. D **69** (10 2004) 105009, URL: https://link.aps.org/doi/10.1103/PhysRevD.69.105009 (cit. on p. 6).

[18] A. G. Riess et al., *Observational Evidence from Supernovae for an Accelerating Universe and a Cosmological Constant*, The Astronomical Journal **116** (1998) 1009, URL: https://doi.org/10.1086%2F300499 (cit. on p. 6).

[19] G. Goldhaber and D. B. Cline, "The Acceleration of the Expansion of the Universe: A Brief Early History of the Supernova Cosmology Project (SCP)", *AIP Conference Proceedings*, AIP, 2009, URL: https://doi.org/10.1063%2F1.3232196 (cit. on p. 6).

[20] M. H. Ahn, S. Aoki, H. Bhang, et al., *Indications of Neutrino Oscillation in a 250 km Long-Baseline Experiment*, Phys. Rev. Lett. **90** (4 2003) 041801, URL: https://link.aps.org/doi/10.1103/PhysRevLett.90.041801 (cit. on p. 6).

[21] M. J. Strassler and K. M. Zurek, *Echoes of a hidden valley at hadron colliders*, Physics Letters B **651** (2007) 374, URL: https://doi.org/10.1016%2Fj.physletb.2007.06.055 (cit. on p. 7).

[22] S. Cassel, D. Ghilencea, and G. Ross, *Electroweak and dark matter constraints on a in models with a hidden valley*, Nuclear Physics B **827** (2010) 256, URL: https://doi.org/10.1016%2Fj.nuclphysb.2009.10.029 (cit. on p. 7).

[23] P. Langacker, *The physics of heavy Z' gauge bosons*, Reviews of Modern Physics **81** (2009) 1199, URL: https://doi.org/10.1103%2Frevmodphys.81.1199 (cit. on p. 8).

[24] ATLAS Collaboration, *Search for high-mass dilepton resonances using 139* fb^{-1} *of pp collision data collected at* $\sqrt{s} = 13$ *TeV with the ATLAS detector*, Physics Letters B **796** (2019) 68, URL: https://doi.org/10.1016%2Fj.physletb.2019.07.016 (cit. on pp. 8, 9).

[25] CMS Collaboration, *Search for resonant and nonresonant new phenomena in high-mass dilepton final states at* $\sqrt{s} = 13$ *TeV*, Journal of High Energy Physics **2021** (2021) 208, URL: https://doi.org/10.1007%2Fjhep07%282021%29208 (cit. on pp. 8, 9).

[26] L. Basso, A. Belyaev, S. Moretti, and C. H. Shepherd-Themistocleous, *Phenomenology of the minimal* $B-L$ *extension of the Standard model:* Z' *and neutrinos*, Physical Review D **80** (2009) 055030, URL: https://doi.org/10.1103%2Fphysrevd.80.055030 (cit. on p. 8).

[27] P. D. Group et al., *Review of Particle Physics*, Progress of Theoretical and Experimental Physics **2022** (2022) 083C01, eprint: https://academic.oup.com/ptep/article-pdf/2022/8/083C01/49175539/ptac097.pdf, URL: https://doi.org/10.1093/ptep/ptac097 (cit. on pp. 8, 9).

[28] M. Bauer, S. Diefenbacher, T. Plehn, M. Russell, and D. A. Camargo, *Dark matter in anomaly-free gauge extensions*, SciPost Phys. **5** (2018) 036, URL: https://scipost.org/10.21468/SciPostPhys.5.4.036 (cit. on pp. 9, 35).

[29] L. Evans and P. Bryant, *LHC Machine*, Journal of Instrumentation **3** (2008) S08001, URL: https://dx.doi.org/10.1088/1748-0221/3/08/S08001 (cit. on p. 10).

[30] ATLAS Collaboration, *The ATLAS Experiment at the CERN Large Hadron Collider*, Journal of Instrumentation **3** (2008) S08003, URL: https://dx.doi.org/10.1088/1748-0221/3/08/S08003 (cit. on pp. 10, 11, 13, 15, 17, 20).

[31] *LEP design report*, Report, CERN, 1983, URL: https://cds.cern.ch/record/98881 (cit. on p. 10).

[32] R. Scrivens et al., *Overview of the status and developments on primary ion sources at CERN**, (2011), URL: https://cds.cern.ch/record/1382102 (cit. on p. 10).

[33] O. S. Brüning et al., *LHC Design Report*, CERN Yellow Reports: Monographs, CERN, 2004, URL: https://cds.cern.ch/record/782076 (cit. on p. 10).

[34] J. Haffner, *The CERN accelerator complex. Complexe des accélérateurs du CERN*, (2013), URL: https://cds.cern.ch/record/1621894 (cit. on p. 11).

[35] CMS Collaboration, *The CMS experiment at the CERN LHC*, Journal of Instrumentation **3** (2008) S08004, URL: https://dx.doi.org/10.1088/1748-0221/3/08/S08004 (cit. on p. 11).

[36] LHCb Collaboration, *The LHCb Detector at the LHC*, Journal of Instrumentation **3** (2008) S08005, URL: https://dx.doi.org/10.1088/1748-0221/3/08/S08005 (cit. on p. 11).

[37] ALICE Collaboration, *The ALICE experiment at the CERN LHC*, Journal of Instrumentation **3** (2008) S08002, URL: https://dx.doi.org/10.1088/1748-0221/3/08/S08002 (cit. on p. 11).

[38] D. Boussard and T. P. R. Linnecar, *The LHC Superconducting RF System*, tech. rep. LHC-Project-Report-316, CERN-LHC-Project-Report-316, CERN, 1999, URL: https://cds.cern.ch/record/410377 (cit. on p. 11).

[39] ATLAS Collaboration, *Luminosity Public Results Run 2*, https://twiki.cern.ch/twiki/bin/view/AtlasPublic/LuminosityPublicResultsRun2, URL: https://twiki.cern.ch/twiki/bin/view/AtlasPublic/LuminosityPublicResultsRun2 (cit. on p. 12).

[40] G. Avoni et al., *The new LUCID-2 detector for luminosity measurement and monitoring in ATLAS*, JINST **13** (2018) P07017 (cit. on pp. 12, 33).

[41] ATLAS Collaboration, *Luminosity determination in pp collisions at $\sqrt{s} = 13$ TeV using the ATLAS detector at the LHC*, arXiv: 2212.09379 [hep-ex] (cit. on pp. 12, 33, 67).

[42] H. Pernegger, *The Pixel Detector of the ATLAS experiment for LHC Run-2*, Journal of Instrumentation **10** (2015) C06012, URL: https://dx.doi.org/10.1088/1748-0221/10/06/C06012 (cit. on p. 14).

[43] S. Grinstein, *Overview of the ATLAS insertable B-layer (IBL) project*, Nuclear Instruments and Methods in Physics Research Section A: Accelerators, Spectrometers, Detectors and Associated Equipment **699** (2013) 61, URL: http://www.sciencedirect.com/science/article/pii/S0168900212003440 (cit. on p. 16).

[44] A. Abdesselam and T. Akimoto, *The Barrel Modules of the ATLAS SemiConductor Tracker*, tech. rep. ATL-INDET-PUB-2006-005, ATL-COM-INDET-2006-009, CERN-ATL-COM-INDET-2006-009, CERN, 2006, URL: https://cds.cern.ch/record/974073 (cit. on p. 16).

[45] A. Abdesselam, *ATLAS SCT Endcap Module Production*, tech. rep. ATL-INDET-PUB-2006-007, ATL-COM-INDET-2006-008, CERN, 2006, URL: https://cds.cern.ch/record/973395 (cit. on p. 16).

[46] A. Vogel, *ATLAS Transition Radiation Tracker (TRT): Straw Tube Gaseous Detectors at High Rates*, tech. rep. ATL-INDET-PROC-2013-005, CERN, 2013, URL: https://cds.cern.ch/record/1537991 (cit. on p. 16).

[47] ATLAS Collaboration, *Particle Identification Performance of the ATLAS Transition Radiation Tracker*, tech. rep. ATLAS-CONF-2011-128, CERN, 2011, URL: https://cds.cern.ch/record/1383793 (cit. on p. 17).

[48] ATLAS Collaboration, *ATLAS calorimeter performance: Technical Design Report*, Technical design report. ATLAS, CERN, 1996, URL: https://cds.cern.ch/record/331059 (cit. on p. 17).

[49] H. Zhang (On behalf ofthe ATLAS Liquid Argon Calorimeter Group), *The ATLAS Liquid Argon Calorimeter: Overview and Performance*, Journal of Physics: Conference Series **293** (2011) 012044, URL: https://dx.doi.org/10.1088/1742-6596/293/1/012044 (cit. on p. 17).

[50] A. M. Henriques Correia, *The ATLAS Tile Calorimeter*, tech. rep. ATL-TILECAL-PROC-2015-002, CERN, 2015, URL: https://cds.cern.ch/record/2004868 (cit. on p. 17).

[51] ATLAS Collaboration, *ATLAS liquid-argon calorimeter: Technical Design Report*, Technical design report. ATLAS, CERN, 1996, URL: https://cds.cern.ch/record/331061 (cit. on p. 18).

[52] ATLAS Collaboration, *ATLAS tile calorimeter: Technical Design Report*, Technical design report. ATLAS, CERN, 1996, URL: https://cds.cern.ch/record/331062 (cit. on p. 19).

[53] ATLAS Collaboration, *ATLAS muon spectrometer: Technical Design Report*, Technical design report. ATLAS, CERN, 1997, URL: https://cds.cern.ch/record/331068 (cit. on p. 19).

[54] F. Bauer et al., *Construction and test of MDT chambers for the ATLAS muon spectrometer*, Nuclear Instruments and Methods in Physics Research Section A: Accelerators, Spectrometers, Detectors and Associated Equipment **461** (2001) 17, URL: https://www.sciencedirect.com/science/article/pii/S0168900200011566 (cit. on p. 21).

[55] T. Argyropoulos et al., "Cathode strip chambers in ATLAS : Installation, commissioning and in situ performance", *2008 IEEE Nuclear Science Symposium Conference Record*, 2008 2819 (cit. on p. 21).

[56] G. Aielli et al., *The RPC first level muon trigger in the barrel of the ATLAS experiment*, Nuclear Physics B - Proceedings Supplements **158** (2006) 11, URL: https://www.sciencedirect.com/science/article/pii/S0920563206004178 (cit. on p. 21).

[57] A. Yamamoto et al., *Progress in ATLAS central solenoid magnet*, IEEE Transactions on Applied Superconductivity **10** (2000) 353 (cit. on p. 22).

[58] ATLAS Collaboration, *Performance of the ATLAS trigger system in 2015*, The European Physical Journal C **77** (2017) 317, URL: https://doi.org/10.1140%2Fepjc%2Fs10052-017-4852-3 (cit. on p. 23).

[59] A. R. Martínez (On behalf of the ATLAS Collaboration), *The Run-2 ATLAS Trigger System*, Journal of Physics: Conference Series **762** (2016) 012003, URL: https://dx.doi.org/10.1088/1742-6596/762/1/012003 (cit. on p. 24).

[60] T. Vazquez Schroeder, *The ATLAS Trigger in Run-2: Design, Menu, and Performance*, tech. rep. ATL-DAQ-PROC-2017-027, CERN, 2018, URL: https://cds.cern.ch/record/2287548 (cit. on p. 24).

[61] J. Pequenao and P. Schaffner, "How ATLAS detects particles: diagram of particle paths in the detector", 2013, URL: https://cds.cern.ch/record/1505342 (cit. on p. 26).

[62] ATLAS Collaboration, *Performance of the reconstruction of large impact parameter tracks in the ATLAS inner detector*, tech. rep. ATL-PHYS-PUB-2017-014, CERN, 2017, URL: https://cds.cern.ch/record/2275635 (cit. on pp. 25, 27, 28).

[63] ATLAS Collaboration, *Performance of vertex reconstruction algorithms for detection of new long-lived particle decays within the ATLAS inner detector*, tech. rep. ATL-PHYS-PUB-2019-013, CERN, 2019, URL: https://cds.cern.ch/record/2669425 (cit. on pp. 26, 29, 63).

[64] T. Cornelissen et al., *Concepts, Design and Implementation of the ATLAS New Tracking (NEWT)*, tech. rep. ATL-SOFT-PUB-2007-007, ATL-COM-SOFT-2007-002, CERN, 2007, URL: https://cds.cern.ch/record/1020106 (cit. on p. 26).

[65] R. Frühwirth, *Application of Kalman filtering to track and vertex fitting*, Nuclear Instruments and Methods in Physics Research Section A: Accelerators, Spectrometers, Detectors and Associated Equipment **262** (1987) 444, URL: https://www.sciencedirect.com/science/article/pii/0168900287908874 (cit. on p. 27).

[66] ATLAS Collaboration, *Performance of the ATLAS track reconstruction algorithms in dense environments in LHC Run 2*, The European Physical Journal C **77** (2017) 673, URL: https://doi.org/10.1140%2Fepjc%2Fs10052-017-5225-7 (cit. on p. 27).

[67] ATLAS Collaboration, *Reconstruction of primary vertices at the ATLAS experiment in Run 1 proton–proton collisions at the LHC*, The European Physical Journal C **77** (2017) 332, URL: https://doi.org/10.1140/epjc/s10052-017-4887-5 (cit. on p. 29).

[68] S. Boutle et al., *Primary vertex reconstruction at the ATLAS experiment*, Journal of Physics: Conference Series **898** (2017) 042056, URL: https://dx.doi.org/10.1088/1742-6596/898/4/042056 (cit. on p. 29).

[69] ATLAS Collaboration, *Mapping the material in the ATLAS Inner Detector using secondary hadronic interactions in 7 TeV collisions*, tech. rep. ATLAS-CONF-2010-058, CERN, 2010, URL: https://cds.cern.ch/record/1281331 (cit. on p. 29).

[70] R. E. Kalman, *A new approach to linear filtering and prediction problems*, Trans. ASME, D **82** (1960) 35, URL: https://cds.cern.ch/record/434680 (cit. on p. 29).

[71] ATLAS Collaboration, *Electron reconstruction and identification in the ATLAS experiment using the 2015 and 2016 LHC proton–proton collision data at $\sqrt{s} = 13$ TeV*, The European Physical Journal C **79** (2019) 639, URL: https://doi.org/10.1140%5C%2Fepjc%5C%2Fs10052-019-7140-6 (cit. on p. 31).

[72] W. Lampl et al., *Calorimeter Clustering Algorithms: Description and Performance*, tech. rep. ATL-LARG-PUB-2008-002, ATL-COM-LARG-2008-003, CERN, 2008, URL: https://cds.cern.ch/record/1099735 (cit. on p. 31).

[73] ATLAS Collaboration, *Improved electron reconstruction in ATLAS using the Gaussian Sum Filter-based model for bremsstrahlung*, tech. rep. ATLAS-CONF-2012-047, CERN, 2012, URL: https://cds.cern.ch/record/1449796 (cit. on p. 31).

[74] ATLAS Collaboration, *Electron and photon energy calibration with the ATLAS detector using 2015–2016 LHC proton-proton collision data*, Journal of Instrumentation **14** (2019) P03017, URL: https://dx.doi.org/10.1088/1748-0221/14/03/P03017 (cit. on p. 31).

[75] ATLAS Collaboration, *Electron and photon energy calibration with the ATLAS detector using LHC Run 2 data*, 2023, arXiv: 2309.05471 [hep-ex] (cit. on p. 31).

[76] ATLAS Collaboration, *Muon reconstruction performance of the ATLAS detector in proton–proton collision data at $\sqrt{s} = 13$ TeV*, The European Physical Journal C **76** (2016) 292, URL: https://doi.org/10.1140%2Fepjc%2Fs10052-016-4120-y (cit. on p. 31).

[77] ATLAS Collaboration, *The ATLAS Simulation Infrastructure*, The European Physical Journal C **70** (2010) 823, URL: https://doi.org/10.1140%2Fepjc%2Fs10052-010-1429-9 (cit. on p. 35).

[78] S. Agostinelli et al., *Geant4—a simulation toolkit*, Nuclear Instruments and Methods in Physics Research Section A: Accelerators, Spectrometers, Detectors and Associated Equipment **506** (2003) 250, URL: https://www.sciencedirect.com/science/article/pii/S0168900203013688 (cit. on p. 35).

[79] ATLAS Collaboration, *Search for displaced vertices of oppositely charged leptons from decays of long-lived particles in pp collisions at $\sqrt{s} = 13$ TeV with the ATLAS detector*, Physics Letters B **801** (2020) 135114, URL: https://www.sciencedirect.com/science/article/pii/S0370269319308366 (cit. on pp. 35, 43).

[80] J. Alwall et al., *The automated computation of tree-level and next-to-leading order differential cross sections, and their matching to parton shower simulations*, Journal of High Energy Physics **2014** (2014) 79, URL: https://doi.org/10.1007%5C%2Fjhep07%5C%282014%5C%29079 (cit. on p. 35).

[81] T. Sjöstrand et al., *An introduction to PYTHIA 8.2*, Computer Physics Communications **191** (2015) 159, URL: https://doi.org/10.1016%5C%2Fj.cpc.2015.01.024 (cit. on pp. 35, 37).

[82] NNPDF Collaboration, R. D. Ball, et al., *Parton distributions with LHC data*, Nucl. Phys. B **867** (2013) 244, arXiv: 1207.1303 [hep-ph] (cit. on pp. 35, 37).

[83] S. Frixione, P. Nason, and C. Oleari, *Matching NLO QCD computations with parton shower simulations: the POWHEG method*, Journal of High Energy Physics **2007** (2007) 070, URL: https://doi.org/10.1088%5C%2F1126-6708%5C%2F2007%5C%2F11%5C%2F070 (cit. on p. 37).

[84] T. Sjöstrand, S. Mrenna, and P. Z. Skands, *A brief introduction to PYTHIA 8.1*, Comput. Phys. Commun. **178** (2008) 852, arXiv: 0710.3820 [hep-ph] (cit. on p. 37).

[85] J. Catmore, M. Elsing, E. Lipeles, D. Rousseau, and I. Vivarelli, *Report of the Analysis Model Study Group*, tech. rep. ATL-COM-SOFT-2013-005, CERN, 2013, URL: https://cds.cern.ch/record/1543445 (cit. on p. 39).

[86] ATLAS Collaboration, *Study of the material of the ATLAS inner detector for Run 2 of the LHC*, Journal of Instrumentation **12** (2017) P12009, URL: https://dx.doi.org/10.1088/1748-0221/12/12/P12009 (cit. on p. 43).

[87] K. F. Di Petrillo et al., *Search for long-lived, massive particles in events with a displaced vertex and muon in pp collisions at $\sqrt{s} = 13$ TeV with the ATLAS detector*, tech. rep. ATL-COM-PHYS-2018-1138, CERN, 2018, URL: https://cds.cern.ch/record/2633973 (cit. on p. 43).

[88] ATLAS Collaboration, *Search for long-lived, massive particles in events with displaced vertices and missing transverse momentum in $\sqrt{s}$ = 13 TeV pp collisions with the ATLAS detector*, Phys. Rev. D **97** (5 2018) 052012, URL: https://link.aps.org/doi/10.1103/PhysRevD.97.052012 (cit. on p. 43).

[89] M. Aoki et al., *Search for long-lived, massive particles in events with a displaced vertex and multiple jets in $\sqrt{s} = 13$ TeV collisions with the ATLAS detector*, tech. rep. ATL-COM-PHYS-2021-1049, CERN, 2021, URL: https://cds.cern.ch/record/2792409 (cit. on p. 43).

[90] M. Backhaus, *The upgraded Pixel Detector of the ATLAS Experiment for Run2 at the Large Hadron Collider*, tech. rep. ATL-INDET-PROC-2015-015, CERN, 2016, URL: https://cds.cern.ch/record/2110260 (cit. on p. 43).

[91] D. Krauss, "Search for long-lived particles decaying to oppositely charged lepton pairs with the ATLAS experiment at $\sqrt{s} = 13$ TeV", PhD thesis, 2019, URL: https://cds.cern.ch/record/2712393 (cit. on pp. 56, 60).

[92] K. Bjoerke et al., *Summary of and Recommendations for the "Better than Zero" Problem*, tech. rep. ATL-COM-GEN-2017-009, CERN, 2017, URL: https://cds.cern.ch/record/2280679 (cit. on p. 65).

[93] W. Buttinger, *Using Event Weights to account for differences in Instantaneous Luminosity and Trigger Prescale in Monte Carlo and Data*, tech. rep. ATL-COM-SOFT-2015-119, CERN, 2015, URL: https://cds.cern.ch/record/2014726 (cit. on p. 68).

[94] E. Ruttinger, *Electron identification efficiencies using the Zmass method*, tech. rep. ATL-COM-PHYS-2021-1064, CERN, 2021, URL: https://cds.cern.ch/record/2798044 (cit. on p. 70).

[95] ATLAS Collaboration, *Electron and photon performance measurements with the ATLAS detector using the 2015–2017 LHC proton-proton collision data*, Journal of Instrumentation **14** (2019) P12006, URL: https://dx.doi.org/10.1088/1748-0221/14/12/P12006 (cit. on p. 70).

[96] A. Collaboration, *Electron and photon efficiencies in LHC Run 2 with the ATLAS experiment*, 2023, arXiv: 2308.13362 [hep-ex] (cit. on p. 70).

[97] ATLAS Collaboration, *Muon reconstruction and identification efficiency in ATLAS using the full Run 2 pp collision data set at $\sqrt{s} = 13$ TeV*, The European Physical Journal C **81** (2021) 578, URL: https://doi.org/10.48550/arXiv.2012.00578 (cit. on p. 70).

[98] *Early Inner Detector Tracking Performance in the 2015 data at $\sqrt{s} = 13$ TeV*, tech. rep. ATL-PHYS-PUB-2015-051, CERN, 2015, URL: `https://cds.cern.ch/record/2110140` (cit. on p. 85).

[99] S. H. Oh and C. Wang, *Kshort and Lambda Production In Jets from pp Collisions at 7 TeV Center-of-Mass Energy*, tech. rep. ATL-COM-PHYS-2014-1258, CERN, 2014, URL: `https://cds.cern.ch/record/1951024` (cit. on p. 85).

[100] M. Baak et al., *HistFitter software framework for statistical data analysis*, The European Physical Journal C **75** (2015) 153, URL: `https://doi.org/10.1140%2Fepjc%2Fs10052-015-3327-7` (cit. on p. 93).

[101] G. Cowan, *Statistics for Searches at the LHC*, 2013, arXiv: `1307.2487 [hep-ex]` (cit. on pp. 93, 94).

[102] K. Cranmer, *Practical Statistics for the LHC*, 2015, arXiv: `1503.07622 [physics.data-an]` (cit. on pp. 93, 94).

[103] G. Cowan, K. Cranmer, E. Gross, and O. Vitells, *Asymptotic formulae for likelihood-based tests of new physics*, The European Physical Journal C **71** (2011) 1554, URL: `https://doi.org/10.1140/epjc/s10052-011-1554-0` (cit. on p. 94).

[104] A. L. Read, *Presentation of search results: the CLs technique*, Journal of Physics G: Nuclear and Particle Physics **28** (2002) 2693, URL: `https://dx.doi.org/10.1088/0954-3899/28/10/313` (cit. on p. 94).

[105] ATLAS Collaboration, *Performance of the reconstruction of large impact parameter tracks in the inner detector of ATLAS*, 2023, arXiv: `2304.12867 [hep-ex]` (cit. on p. 101).